

Statistical analysis of stress and deformation state in polycrystalline aggregates with a large number of grains

Dissertation

zur Erlangung des akademischen Grades

Doktoringenieur
(Dr.-Ing.)

von M.Sc. Oleksandr Prygorniev
geb. am 22.11.1987 in Kharkiw
genehmigt durch die Fakultät für Maschinenbau
der Otto-von-Guericke-Universität Magdeburg
Gutachter:
apl.Prof.Dr.-Ing.habil. Konstantin Naumenko
Prof.Dr.rer.nat. Siegfried Schmauder
Promotionskolloquium am 17.06.2015

Abstract

The present thesis is focused on the numerical modeling and simulation of polycrystalline structures with the macroscopic dimensions and realistic boundary conditions. The microstructure of polycrystals is represented by the randomized three-dimensional Voronoi diagram assuming the convexity of grains and faces. In order to achieve the macroscopic dimensions of structures, a large number of grains must be calculated and generated within the geometrical model. On the other hand, several assumptions such as the simple grain material model, grains interaction approach, etc. should be introduced to reduce the computational costs. The developed software framework generates the geometrical and finite element models of a polycrystal considering arbitrary shape of sample, thickness of the grain boundary layer, number of grains, and other geometrical properties.

The main idea is to investigate the influence of the heterogeneous microstructure on the macroscopic behavior in different regions of the polycrystals such as the bulk, notches, and surface area. For this reason, specific numerical algorithms of averaging and interpolation are developed and implemented in an efficient programming code to perform a statistical analysis of the simulation results. One usually considers a scale separation method with the representative volume element to introduce the microstructural material behavior at the macroscale. However, the obtained results of the simulation with entire polycrystals show an appearance of the surface layer effect, which is not covered by the classical continuum theory. After thorough investigation of the smooth and notched cylindrical polycrystals under different loading conditions, the thickness of the surface layer and the strength of the surface layer effect were determined.

The proposed method and developed framework can be further used for the analysis of polycrystalline heterogeneous materials with various material models and under arbitrary loading conditions.

Zusammenfassung

Die vorliegende Dissertation beschäftigt sich mit der geometrischen Modellierung und Simulation von polykristallinen Strukturen unter Berücksichtigung der makroskopischen Abmessungen und realistischer Randbedingungen. Die Mikrostruktur der Polykristalle wird durch stochastische, regellos aufgebaute, dreidimensionale Voronoi-Diagramme repräsentiert unter Annahme konvexer Körner und Korngrenzen. Um makroskopische Abmessungen zu berücksichtigen, muss man ein Voronoi-Diagramm mit einer großen Anzahl an Körnern generieren und die Ergebnisse im geometrischen Modell abbilden. Außerdem müssen einige Annahmen, zum Beispiel bezüglich des Materialmodells und der Wechselwirkung der Körner, getroffen werden, um die Rechenkosten zu reduzieren. Das entwickelte Programmgerüst generiert die geometrischen und Finite-Elemente-Modelle unter Berücksichtigung der beliebigen Formen des Polykristalls, Dicke der Korngrenzen, Anzahl der Körner und anderer variierender geometrischer Eigenschaften.

Der Grundgedanke besteht dabei in der Untersuchung des Einflusses der heterogenen Gefügestruktur auf das makroskopische Materialverhalten in unterschiedlichen Teilgebieten eines Polykristalls, wie zum Beispiel das Innere des Polykristalls, Kerben und Oberflächen. Deshalb werden spezielle numerische Algorithmen zur Mittelung und Interpolation entwickelt und in einen leistungsfähigen Programmcode implementiert, um eine statistische Analyse der Simulationsergebnisse durchzuführen. Üblicherweise wird das Materialverhalten auf der Mikroebene ins makroskopische Modell integriert, indem die verschiedenen Skalen mittels eines repräsentativen Volumenelements getrennt werden. Die erzielten Simulationsergebnisse der ganzen Polykristalle lassen jedoch auf das Auftreten von Oberflächenschichteffekten schließen, welche in der klassischen Kontinuumstheorie nicht berücksichtigt werden. Die Dicke der Oberflächenschicht und die Stärke des Oberflächenschichteffekts werden nach sorgfältiger Untersuchung der glatten und gekerbten zylindrischen Polykristalle unter verschiedenen Beanspruchungsbedingungen bestimmt.

Man kann die vorgeschlagene Methode und das entwickelte Programmgerüst zur Analyse von polykristallinen heterogenen Materialien mit variierenden Materialmodellen und unterschiedlichen Beanspruchungsbedingungen einsetzen.



Contents

Contents	I
List of Figures	III
List of Tables	VII
1 Introduction and Motivation	1
1.1 Introduction	1
1.2 Motivation	4
2 Models for polycrystals	9
2.1 Masing model	14
2.1.1 Example with three rods	15
2.1.2 Statistical distribution of yield stress	17
2.1.3 Masing principle	18
2.2 Voronoi diagram	19
2.2.1 Algorithms overview	21
2.2.2 Cell-based generation algorithm	23
2.2.3 Grain boundary layer	25
2.2.4 Geometrical singularities	30
2.2.5 Randomized incremental algorithm	32
2.3 Construction in CAD/CAE Abaqus	37
2.3.1 Shape of polycrystal	39
2.4 Finite element model	41
2.4.1 Finite-thickness boundary layer	41

2.4.2	Mesh dependence	45
3	Constitutive equations	49
3.1	Grain interior	49
3.2	Grain boundaries	52
4	Postprocessing	57
4.1	Volumetric averaging	58
4.2	Point-wise averaging	59
4.3	Interpolation using shape functions	60
4.3.1	Linear tetrahedral finite element	62
4.3.2	Linear hexahedral finite element	63
4.3.3	Linear prism finite element	64
5	Simulation	67
5.1	Surface layer effect	68
5.1.1	Rectangular plate under cyclic load	68
5.1.2	Cylindrical bar in cyclic viscoplasticity	72
5.1.3	Cylindrical bar under tension. Loading rate dependence	75
5.1.4	Cylindrical bar under tension. Relaxation test	78
5.1.5	Cylindrical bar under multicyclic deformation	79
5.1.6	Influence of grain material's anisotropy	80
5.1.7	Elastic tension of notched cylindrical bar	82
5.2	Intergranular fracture	86
5.2.1	Sensitivity analysis of viscosity parameter	87
5.2.2	Displacement-controlled test	89
5.2.3	Uniaxial creep test of cylindrical polycrystal	90
6	Conclusions	95
A	Implicit time integration scheme	101
B	Mapping of arbitrary point in extruded hexahedral finite element	103
C	Mapping of arbitrary point in extruded prism finite element	105
	Bibliography	107

List of Figures

1.1	Examples of copper microparts and microstructures	5
1.2	Example of fuel cell plate	5
1.3	Strains in compressed aluminium specimen	7
2.1	Polycrystalline microstructure of copper	9
2.2	Elasticity modulus of single crystal	10
2.3	Distribution of crystallographic orientations	10
2.4	Reconstruction of the microstructure	12
2.5	2D Voronoi diagram	13
2.6	Masing model	14
2.7	Construction of the stress-strain diagram for three rods	16
2.8	Continuous Masing-type model	17
2.9	Illustration of the Masing principle	19
2.10	Gravitational influence of stars	20
2.11	Voronoi diagrams in nature	20
2.12	Samples of aluminum/silicon-carbide foam	21
2.13	Cubic crystallites	21
2.14	Duality of the Voronoi diagram and Delaunay tessellation	22
2.15	Raster Voronoi diagram	23
2.16	Formation of the cell by cutting with half-space planes	24
2.17	Cavities in grain boundaries	26
2.18	Transformation of grains	27
2.19	Offset of faces	28
2.20	Grain boundaries	29

2.21	Short edge	29
2.22	Examples of short edges	30
2.23	Regularization of the Voronoi diagram	31
2.24	Construction of 6 cells with randomized incremental approach	33
2.25	Algorithm of modified randomized incremental algorithm	34
2.26	Step-by-step construction of a grain	38
2.27	Formation of cylindrical polycrystal	40
2.28	Unmeshable boundaries	40
2.29	Example of meshing two grains and boundaries between them	42
2.30	Geometrical and FE model of grain boundaries in polycrystal	42
2.31	Calculation of point's barycentric coordinates	43
2.32	Scheme of interpolation and transformation of nodes	44
2.33	Example of the unit cell model with 1000 grains	46
2.34	Mesh-dependence	47
3.1	Cohesive finite element COH3D6	52
3.2	Examples of deformation of bicrystal with cohesive grain boundary	55
4.1	Normal stresses in cylindrical polycrystal	57
4.2	Scheme of point-wise averaging over N samples of polycrystal	60
4.3	Illustration of the mapping procedure	62
4.4	Arbitrary point P within linear tetrahedral finite element C3D4	62
4.5	Arbitrary point P within linear hexahedral finite element C3D8	63
4.6	Arbitrary point P within linear prism finite element C3D6	64
5.1	Rectangular plate under cyclic load	70
5.2	Averaged stresses in rectangular model	72
5.3	Cylindrical bar under tension	73
5.4	Averaged distributions of stresses in cylindrical model	74
5.5	Averaged distribution of normal stresses in cylindrical bar	75
5.6	Cylindrical polycrystals under different strain rates	76
5.7	Dependence of averaged stresses in cylinder on the radial coordinate	77
5.8	Cylindrical polycrystalline specimen under tension and relaxation	78
5.9	Averaged stresses in cylindrical polycrystal under cyclic load	80
5.10	Averaged stresses vs. radial coordinate in cylindrical specimen	81
5.11	Average stresses vs. radial coordinate in cylindrical specimen	82
5.12	Cylindrical bar with circumferential notch	83
5.13	Notched cylindrical specimen in elastic tensile test	84
5.14	Cylindrical polycrystal with finite-thickness grain boundaries	87
5.15	Influence of the viscosity in displacement-controlled test	88

5.16	Influence of the viscosity in creep test	89
5.17	Cylindrical polycrystal under displacement-controlled tensile load	90
5.18	Cylindrical polycrystal in creep test under different loads	91
5.19	Cylindrical polycrystal in creep test	92
B.1	Arbitrary point within linear hexahedral finite element C3D8	103
C.1	Arbitrary point within linear prism finite element C3D6	105



List of Tables

2.1	Parameters of rods in the example of Masing's model	15
2.2	Time of calculation of Voronoi diagram	35
2.3	Number of edges of in Voronoi diagram	36
2.4	Generation time of Voronoi diagrams with grain boundaries, s . . .	36
2.5	Generation time of finite element meshes in grain boundaries . . .	44
3.1	Elastic material properties of grains	50
3.2	Inelastic material properties of grains	51

Introduction and Motivation

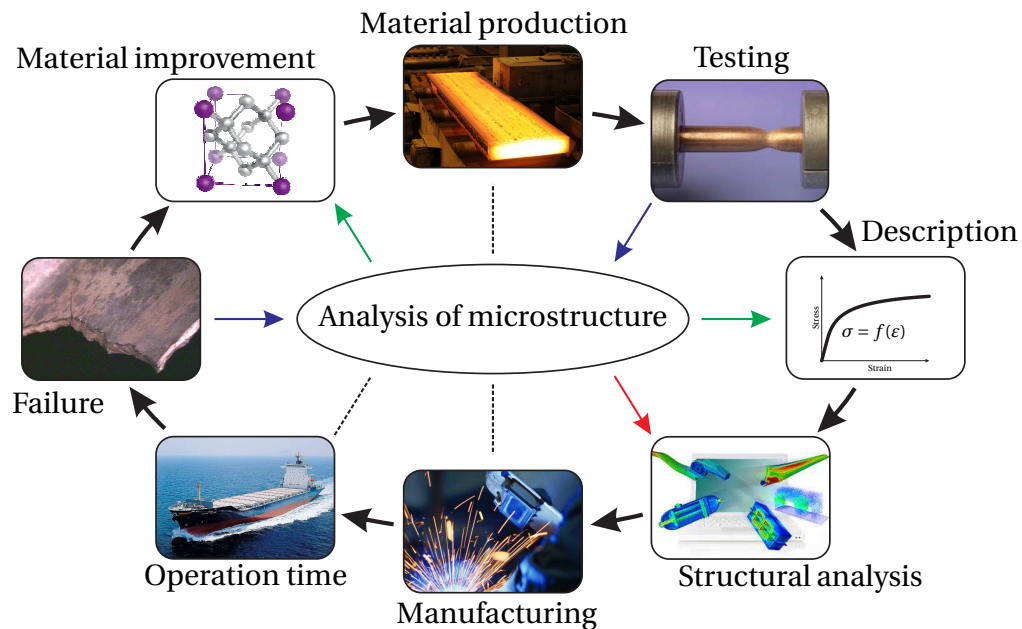
1.1 Introduction

Prolongation of lifetime, weight reduction and compactness are basic goals in the design of many structures. Seeking for the balance between durability and costs, one should consider many engineering aspects such as operation conditions, manufacturing quality, environmental influences, etc. Depending on the used sort of material, these factors influence deformations occurring in the structure in different ways. In order to figure out critical displacements and forces, one performs a structural mechanics analysis, taking into account the loading conditions and the material model. Usually, the elasto-plastic behavior of a specified material is represented as the relationship between macroscopic stresses and strains by means of a stress-strain diagram. It often demonstrates the presence of nonlinear effects and dependencies such as yielding, hardening and the loading rate dependence, which should be described within a constitutive model. The nature of these effects lies in the redistribution of stresses and strains caused by the heterogeneity of microstructure. For this reason, a clear understanding of the material behavior in both micro- and macroscale is needed as a key point in the development of precise material model for structural analysis.

From another point of view, the investigation of the contribution of different microstructural phenomena into a macroscopic response can be useful in the development of new advanced materials, resisting to a defined range of stresses and temperatures. Current progress in manufacturing technologies provides the possibility to design new materials with desired

properties. Thus, a high economic efficiency and reliability can be achieved in special fields of medicine, aerospace, energy engineering, etc. However, the development of new materials suggests a thorough iterative process of modeling, simulation, optimization and testing for different variations of the microstructure until an appropriate configuration is found.

Furthermore, the monitoring of the material's microstructure is recommended at different stages. For example, microstructural defects appear in the material during the manufacturing process because of imperfect technologies. They can propagate during the operation time, depending on the intensity of loads. Therefore, the monitoring of changes at the microscale can be used to prevent a loss of functionality due to unexpected failure. Finally, a microscopic investigation of the damaged zones are useful for the improving of the material.



In the present work, the polycrystalline microstructure is examined using the example of pure copper. A similar microstructure with certain differences can be observed among many other metals and alloys such as silver, aluminium, brass, etc. [16, 112]. Regarding a face-centered cubic crystallographic structure, grains possess anisotropic properties. In polycrystals, grains exhibit different stiffness in the loading direction because of random crystal lattice orientations. Therefore, the distribution of stresses and strains is strongly heterogeneous. Due to the non-uniform accumulation of plastic strains and the non-uniform relaxation, the intensive redistribution

of stresses takes place during loading as well as unloading. In addition, local defects are observed in the form of nucleation and coalescence of voids and dislocations movement, which may eventually cause fracture or failure. These effects together characterize macroscopic behavior which is experimentally observed in stress-strain diagrams, creep curves, and low cycle hysteresis loops of copper[1, 64].

There are two ways to investigate the material microstructure and its macroscopic response: experimental testing and numerical simulation. The precise data can be achieved in the experimental approach, while the numerical study gives an approximated solution. Anyway, both methods have their advantages as well as disadvantages. The analysis of real specimens requires a complicated tool, which includes a testing machine and micrography equipment. Usually, the capturing of a microstructure and the conducting of mechanical tests are carried out separately because of many difficulties in the setup, especially considering an elevated temperature. The taking of micrographs often requires destructive methods, which eliminates further mechanical testing. However, in order to distinguish the influence of different microscopic effects onto a macroscopic response, developments in the microstructure should be investigated during the mechanical test. An accordance between microstructural phenomena and macroscopic properties can be illustrated by examples of simple specimens. For example, in [42] crack propagation in a titanium specimen under tension, captured by in-situ X-ray tomography is analyzed. Unfortunately, high costs and a low accessibility of the required equipment limits the number of experimental tests, whereas a thorough study of different specimens under various loading conditions is necessary. Moreover, the recognition of local stresses, elastic and plastic strains in the microstructure during the test is a complicated task, as discussed in publications [28, 75, 83].

In contrast to the experimental approach, the numerical study provides full information about the material state at any point of the model. By using different numerical methods, such as the finite element method, approximate stresses and strains can be calculated, taking into account the material behavior, loading and boundary conditions. A wide range of microstructural effects can be introduced in the numerical model of polycrystal, including the form of grains, the thickness of grain boundary layer, the orientation of crystalline lattice. On a generated polycrystal with the required shape, different numerical tests such as tension, shear, torsion, cyclic loading, etc. can be performed similarly to real tests. Besides the standard tests, non-realistic experiments are available as well. For example, the inelastic

properties of polycrystal in different directions can be analyzed in several tests with various loads but the identical initial microstructure, which is impossible in real experiments.

The numerical approach is a sufficient groundwork for the analysis of polycrystals, due to low costs and adjustable complexity of the generated microstructure. However, the dimensions and the representability of the polycrystalline model are significantly limited by computational power. For this reason, in order to investigate the accordance of microstructural effects with a macroscopic response, this work is focused on simulation of small specimens.

1.2 Motivation

Many compact structures contain microcomponents such as pins, wires and sheets, which are illustrated in Figs. 1.1 and 1.2. The grain size there is comparable with the dimensions of structures, which allows to illustrate the influence of the heterogeneous microstructure more evidently in comparison to large parts. Moreover, notches, holes, and cuts possess a macroscopic stress gradients around the concentration area in which the prediction of the life time is especially demanded. In large structures, the grain size is much smaller than their dimensions and the concentration factors are well investigated [73], while in microparts, a special behavior can be expected. Nevertheless, the microscopic behavior in those regions and its description within the material model remain unclear.

The general aim of this thesis is the modeling and the simulation of polycrystalline aggregates using the finite element method. Unlike the experimental research, the accuracy of the numerical analysis depends on the level of description of the microstructure and its behavior in the model. The highest representability can be achieved through the implementation of all known and observed microscopic mechanisms. However, the usage of such a model, especially considering the large number of grains, is doubtful from the computational point of view.

Therefore, one should either reduce the size of the polycrystal or simplify the microscopic material behavior. The first approach underlies the well-known scale-separation method which considers two domains of numerical modeling: micro- and macroscopic. The specimen at the macroscale is represented by the homogeneous structure, whereas the polycrystalline microstructure is generated within the elementary representative volume

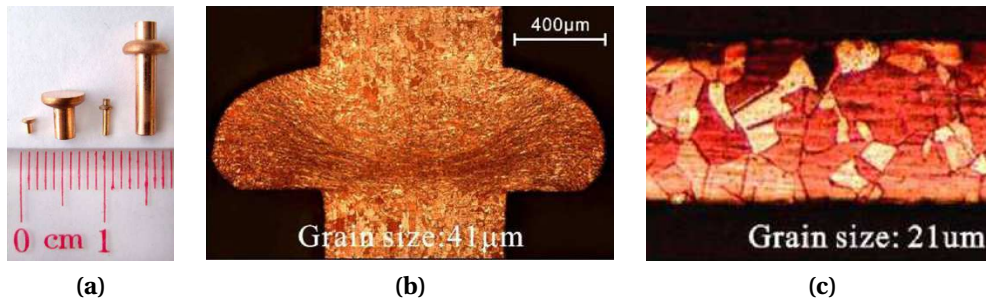


Figure 1.1 Examples of copper microparts (a), the microstructure of pin (b) and the microstructure thin plate (c). After [19]

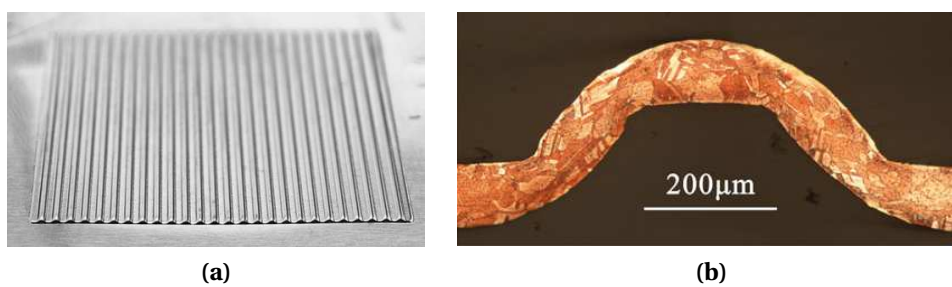


Figure 1.2 Example of fuel cell plate (a) and its microstructure (b), taken from [19, 97]

element (RVE) introduced by Hill in 1963 [43]. The RVE is usually based on the unit cell model with periodic boundary conditions and the periodic microstructure on opposite sides of the cube.

Assuming that macro- deformations and stresses are uniform over the whole volume of the RVE, one can estimate the macroscopic properties of the polycrystal by performing a homogenization procedure in a series of basic tension and shear tests on the unit cell. Thus, heterogeneous stresses and strains under specified loading conditions can be averaged in order to identify parameters of the macroscopic material model.

Due to the periodicity of the unit cell, such a material model smoothly describes the behavior of an arbitrary point in the homogeneous target structure. At the same time, it states the independence of the microstructural behavior described in the RVE on the global boundary conditions. Therefore, the simulation of microparts with a homogeneous structure, characterized by the RVE-based material model, may contain a certain error if macroscopic fields such as stresses or strains exhibit essential gradients. This error can be reduced by decreasing RVE's size until the gradient becomes negligible within the unit cell. However, a low bound of the RVE's size is defined by a minimal

number of grains required to ensure representability. It means that the size of RVE should be defined in a certain range, considering the size of grains and the geometrical configuration of the target structures.

The illustrated examples of the microparts clearly show that the existence of a RVE in such a length scale is questionable. Therefore, the polycrystalline aggregate, including its microstructure, shape and realistic boundary conditions, should be analyzed in its full representation. Such an approach implies the generation of a large number of grains in order to achieve macroscopic dimensions of the specimen. Taking into account the limited computational power, the description of the microstructural behavior should be simplified. Anyway, for a qualitative analysis, one can introduce basic properties such as anisotropic elasticity and viscoplasticity, which together lead to a complex non-linear response. It allows us to investigate the influence of a discrete heterogeneous microstructure in the concentration area, bulk and surface regions within the same analysis. If difference in the estimated material behavior between those regions is negligible, the applicability of the RVE can be confirmed. Otherwise, the scale separation method should be extended in order to cover the observed effects.

The necessity to generate a large number of grains inside a specimen with arbitrary shape raises different problems of efficiency and accuracy. Moreover, the finite element method itself demands additional convergence criteria which must be considered during the generation of the geometrical model. Most of the analysis steps can be performed by using standard algorithms within existing solutions, such as the CAD/CAE programs Abaqus, Ansys, Comsol, Nastran/Patran, etc. However, the development of more advanced algorithms allows us to improve the performance and stability, which are especially important in the study of a random microstructure. For example, generalized meshing algorithms are well suitable for arbitrary solids and planes. Nevertheless, the time of mesh generation can be significantly reduced for special problems like sweep mesh and nodes transition using developed algorithms.

The statistical analysis requires the generation of geometrical and finite element models of the polycrystal in the CAD/CAE Abaqus in fully automatic mode including the assignment of material properties, loading and boundary conditions. It allows us to simulate a large number of samples within a reasonable computational time and effort. Such an automatization can be implemented within a developing framework that consists of an own code, open-source and commercial libraries.

Besides the modeling of a polycrystalline aggregate and its simulation under certain loading conditions, one has to analyze the calculation results. Taking into account the high heterogeneity of strains and stresses, as shown on experimental example in Fig. 1.3, statistical methods must be involved. For example, the macroscopic response of a polycrystal can be computed

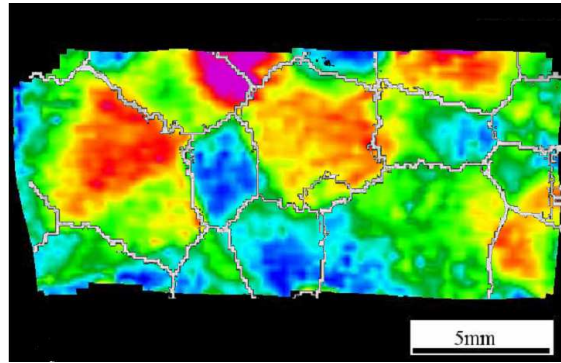


Figure 1.3 Strains in compressed aluminium specimen, after [75]

through the arithmetic averaging of the required field over the whole volume of the structure. The averaged stresses and strains in normal directions are represented by the stress-strain diagram, similar to the ones obtained in real experiments with a testing machine. However, in order to investigate the influence of the polycrystalline microstructure in different regions of the specimen, more advanced averaging and interpolation techniques should be developed. For instance, the distribution of stresses in the radial direction of the specimen can be estimated through averaging over radial layers.

The simulation of the polycrystal with a complex shape remains impracticable from a computational point of view. However, the statistical analysis of the stress and deformation state in simple specimens with the large number of grains admits a wide range of investigation directions, such as the analysis of the stress redistribution in the surface layer, the concentration area and the propagation of cracks. Finally, the information obtained in this research can be used in the verification or improvement of the homogenization technique.

Models for polycrystals

Typical micrographs of pure copper are illustrated in Figs. 2.1a and 2.1b. One can clearly see grains of different shape separated by boundaries. The size and the form of grains depend on the nature of material processing. Hence, the different distributions of grain properties can be observed in the polycrystalline microstructure. Moreover, it is well known that coarsening and refinement of grains often take place during cooling or plastic deformation as an effect of recrystallization [94, 104]. However, in order to simplify the construction and simulation of the microstructure, fixed grain boundaries and a uniform grain size are assumed. Such properties are inherent for isotropic copper at a constant temperature and small deformations.

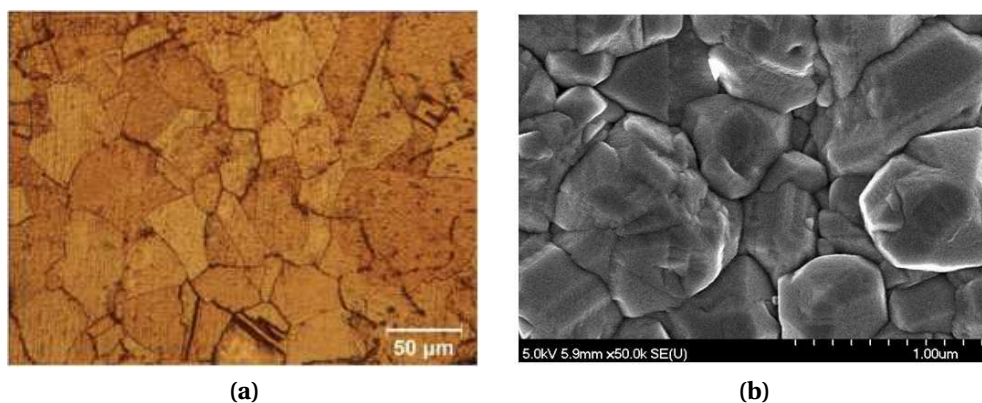


Figure 2.1 Polycrystalline microstructure of copper: (a) bulk region [10]; (b) surface [56]

Besides the geometrical representation, the material model of the microstructure must be introduced. According to the face-centered cubic crystallographic system grains exhibit anisotropic behavior during the deformation. The elastic properties of common single crystals are given in [71, 55, 85]. More evidently, the anisotropy can be illustrated as the dependence of the elasticity modulus on the crystallographic orientation as it is shown for nickel in Fig. 2.2 and for copper in [69]. In the picture, the axes are defined through the Miller notation, which

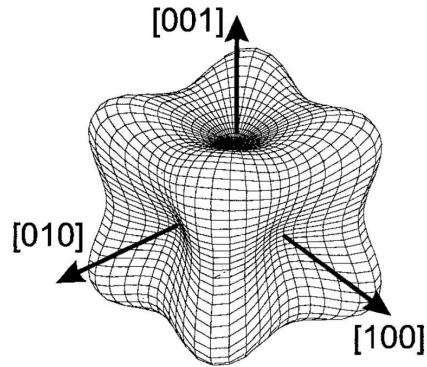


Figure 2.2 Elasticity modulus of single crystal [35]

was introduced by William Hallows Miller [62] in 1839 and has often been used since in the material science in order to describe crystallographic vectors and planes. The distribution of crystalline lattice directions characterizes the heterogeneity of the microstructure in a polycrystalline aggregate. For example, Fig. 2.3a shows the experimentally observed crystallographic orientations in a copper polycrystal, whereby colors represent the crystal directions based on the orientation map in Fig. 2.3b. The capturing and recognition of the microstructure, including material directions, are discussed in the publications [58, 76]. In the present thesis the statistically uniform distribution of material orientations is considered in the same manner as was done in many other works [32, 48, 67]. The implementation of microscopic constitutive material behavior was performed taking into account the anisotropic properties and random local coordinate systems as shown in Section 3 along with a description of the boundary layer.

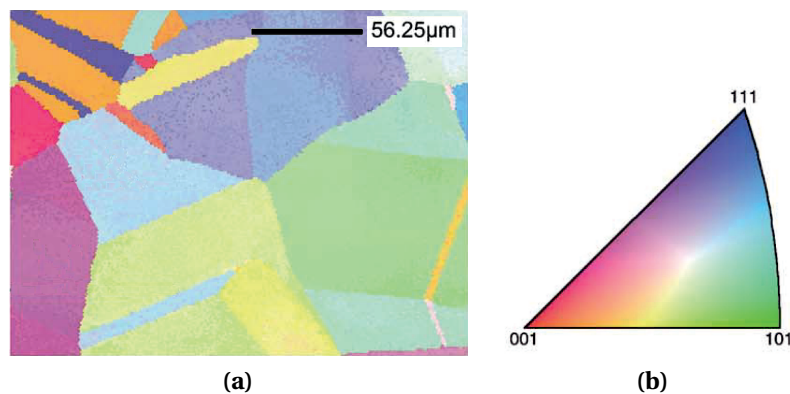


Figure 2.3 Distribution of crystallographic orientations: (a) micrograph; (b) orientation map, after [96]

For this reason, the simulation of polycrystals requires the analysis of an interdependent multi-component system with various micromechanical properties. First solutions were obtained using the simplest analytical and semi-analytical models. For instance, in 1889 and 1929, respectively, Voigt [101] and Reuss [79] have introduced bounds of the elasticity modulus for polycrystals without any consideration of the grain shape. Later, regular microstructures with a specified form of grains were proposed in [66, 99, 106], taking into account the interactions between grains. Due to the quickness and stability of the analytical approach, these models are still widely involved in different multi-iterative problems such as optimization and parametrization. Nevertheless, the simulation of realistic microstructures requires the implementation of more advanced models with an arbitrary three-dimensional shape of grains and interaction behavior.

Atomistic molecular dynamic simulations demonstrate high accuracy in the modeling of nanoscale phenomena in grains and grain boundaries, as discussed in works [57, 68, 95]. For example, the analysis of grain boundary sliding can be performed considering the fact that the thickness of boundaries is equal to few atomic layers. However, the number of grains and the timescale are significantly limited due to the necessity to calculate the interactions between an immense number of particles. It makes the simulation of a polycrystalline aggregate with macroscopic dimensions too expensive from a computational point of view.

A more common way to investigate the polycrystalline microstructure is based on the representation of grains by deformable solids, characterized by anisotropic material behavior and random material orientation. Depending on the type of interaction mechanism, grains can be perfectly glued or bonded regarding specified separation behavior. To estimate stresses and strains in a polycrystal, the structural mechanical analysis should be performed.

A widely known numerical technique for solving complex mechanical problems is the finite element method (FEM). For the structural analysis, it was firstly applied by Alexander Hrennikoff [45] in 1941 and Richard Courant [23] in 1943. The method calculates the solution of partial differential equations through the decomposition of the domain by simpler subdomains - finite elements. Within each finite element, an approximation function is described. Introducing the stiffness matrix, boundary and loading conditions, one can compute forces and displacements at nodes of elements by solving a global system of equations composed from basis functions. Stresses and strains at Gauss points [26, 109, 110] are evaluated using the described material model, considering nodal displacements. A detailed overview on

FEM and its applications can be found in the textbooks [22, 111].

In order to perform the finite element analysis (FEA), the model of polycrystal should be meshed by finite elements such as tetrahedra, prisms, hexahedrons, etc. There are two basic ways to generate a FE mesh for the polycrystalline microstructure. One can either reconstruct the microstructure of real specimen or generate a random one using space partitioning algorithms.

The first method is based on the recognition of photomicrographs as discussed in the works [14, 15, 40, 42, 59]. The algorithm consists of three general steps. First of all, raster images of the micrographs are captured from samples of the material. In order to recognize microstructural details, image processing algorithms can be used as shown in Fig. 2.4 using the example of an aluminium alloy. Thus, the binarization algorithm allows us to highlight regions in which the amplitude of the color gradient exceeds a predefined threshold value. Therefore, grain boundaries can be identified as the effect of color discontinuity in micrographs. Afterwards, using different algorithms of mesh generation [46, 53, 78], one can reconstruct solids of recognized regions by finite elements.

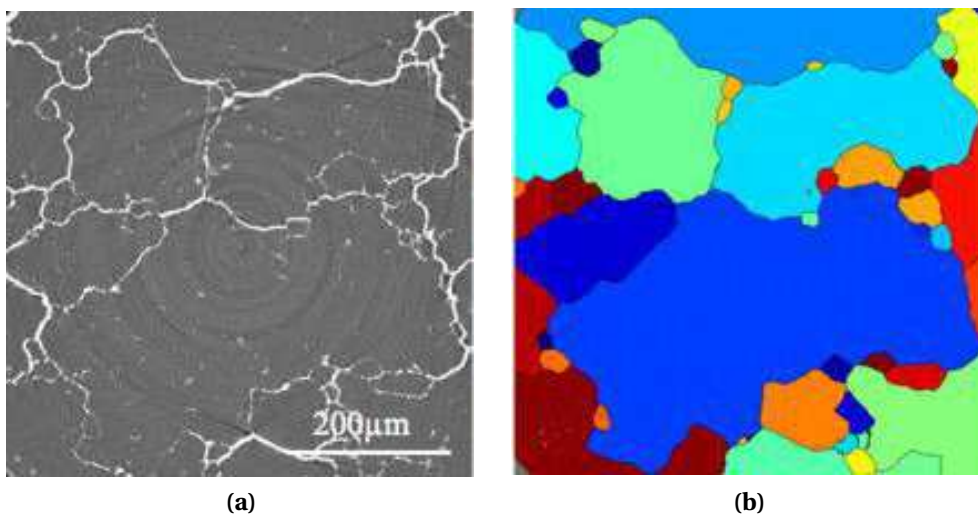


Figure 2.4 Reconstruction of the microstructure: (a) source micrograph; (b) result of segmentation, after [59]

Of course, the detailization and accuracy of this method are limited by the quality of micrographs. If the resolution of images is high enough, the generated model closely represents the microstructure of the original sample, including the shape of grains, crystal lattice orientations, inclusions, voids,

etc. Otherwise, noise data and artifacts can be mistakenly identified as features of the microstructure. Despite the accurate representability of a real microstructure, this approach has a limited applicability. For example, the analysis of polycrystals with specified distribution of grain volume can be complicated since the material sample with the corresponding microstructure should be produced at first.

In contrast to the reconstruction approach, the space partition method allows us to generate a random microstructure with required properties such as number of grains, grain volume distribution, shape of grains, thickness of boundary layer, etc. Therefore, a parametrical and sensitivity analysis can be performed in order to investigate the influence of these properties on the macroscopic response. The representability of the microstructure depends on the type of generation algorithm. For example, convex and concave grains with a curved shape can be constructed using different techniques as discussed in [39, 81]. However, the calculation of curved surfaces needs more computational time in comparison to planar faces. Furthermore, a higher number of finite elements must be generated in order to approximate non-linear surfaces, that increases the simulation time.

For this reason, planar faces and the convexity of grains are assumed in the present work in order to reduce the generation and simulation time of polycrystals with a large number of grains. These assumptions underlie the classical model of Voronoi diagram, illustrated by a two-dimensional example in Fig. 2.5. Applications of this model can be found in many publications [7, 8, 32], due to the similarity with the real microstructure. Regarding the works of Susmit Kumar and Stewart

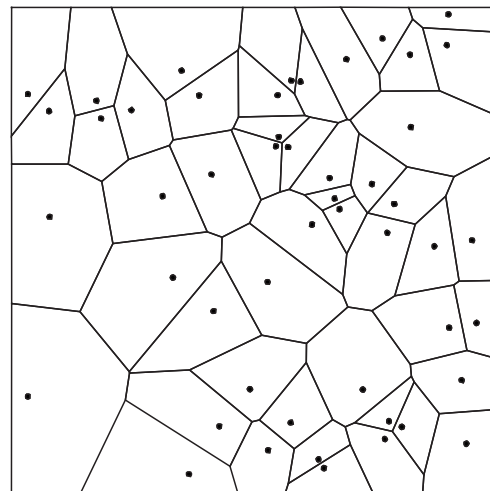


Figure 2.5 2D Voronoi diagram

K. Kurtz [50, 51] the statistical distributions of angles between edges and lengths of edges in the Voronoi diagram correlate with the same properties of real microstructures on the example of aluminium alloy. Moreover, the planar polygonal form of faces facilitate the calculation of the finite-thickness boundary layer and the generation of a corresponding finite element mesh.

Despite the fact that the Voronoi diagram does not represent a real microstructure precisely, it can be used in the qualitative analysis of basic

material properties. The present thesis is focused on the structural analysis of models with a large number of grains. The results of the simulations are given in Section 5, taking into account different loading conditions and the shape of polycrystals. However, in order to illustrate the contribution of microstructural components into a macroscopic response, the simplest model of parallel rods is shown in the next section.

2.1 Masing model

A complex non-linear material response can be formulated by the system of simplest components with different values of specified material parameters. A convenient example to demonstrate the general properties of this method is the model of parallel rods illustrated in Fig. 2.6. All rods are constrained to the same displacements, ignoring the interactions between themselves. Therefore, the shape of rods can be neglected. This model was originally proposed by Georg Masing [60] in 1923 in order to explain the Bauschinger effect. The model is also used in recent works [20, 36, 61, 90].

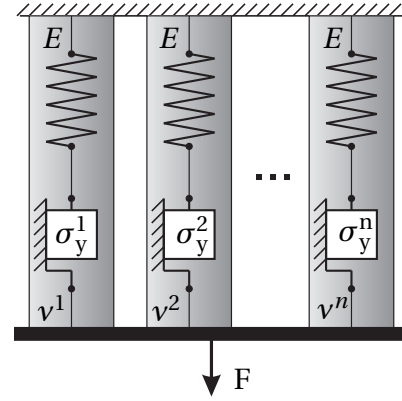


Figure 2.6 Masing model

The material behavior in rods is characterized by a uni-axial ideal elastoplastic model with the identical elasticity modulus E but different yield stress σ_y^k . Considering the equality of applied total strains ε , the stress in each rod σ^k can be described using the Hooke's law:

$$\sigma^k = E(\varepsilon - \varepsilon_{pl}^k), \quad (2.1)$$

where ε_{pl}^k is the plastic strain in k -rod. If the stress in the rod is smaller than the corresponding yield stress, the rod is deforming elastically. Otherwise, the inelastic strain is accumulated in k -rod according to following equation:

$$\varepsilon_{pl}^k = \begin{cases} 0, & \varepsilon \leq \varepsilon_y^k \\ \varepsilon - \varepsilon_y^k & \text{otherwise,} \end{cases} \quad (2.2)$$

where yield strain is $\varepsilon_y^k = \sigma_y^k / E$.

The described behavior can be represented by the rheological model of consistently joined spring and dry friction elements, illustrated in Fig. 2.6

and known as the Prandtl element. Since rods have different yield strengths the accumulation of plastic strains starts irregularly, which induces the non-uniform distribution of stresses. Taking into account the weight coefficients $\sum v^k = 1$, which introduce the specific cross cross-section of rods, the averaged stress can be computed by equation (2.3). In the case where an equal area of cross-sections is considered, the equation transforms into the simple arithmetic mean.

$$\sigma = \sum \sigma^k v^k \quad (2.3)$$

The number of rods and the distribution of yield strengths define the nonlinearity of the homogenized response. In the case where the step between yield stress values of rods is small, the smooth macroscopic yielding can be achieved. However, in order to graphically illustrate the contribution of each rod into the macroscopic response, the model with only three components is discussed in the next section.

2.1.1 Example with three rods

Masing's model of three rods, similar to illustrated in Fig. 2.6, is analyzed considering the following values of yield stress and weight coefficients:

Table 2.1 Parameters of rods in the example of Masing's model

k	Yield stress σ_y^k	Weight coefficient v^k
1	$0.2\sigma_y$	0.6
2	$0.5\sigma_y$	0.3
3	σ_y	0.1

Assuming the identical Young's modulus E , the corresponding yield strain values can be evaluated as shown below for each rod:

$$\varepsilon_y^1 = 0.2\sigma_y/E, \quad \varepsilon_y^2 = 0.5\sigma_y/E, \quad \varepsilon_y^3 = \sigma_y/E$$

Fig. 2.7a represents stress-strain diagrams for each rod with the ideal elasto-plastic model. After the homogenization with equation (2.1), the average stress is constructed as shown in Fig. 2.7b.

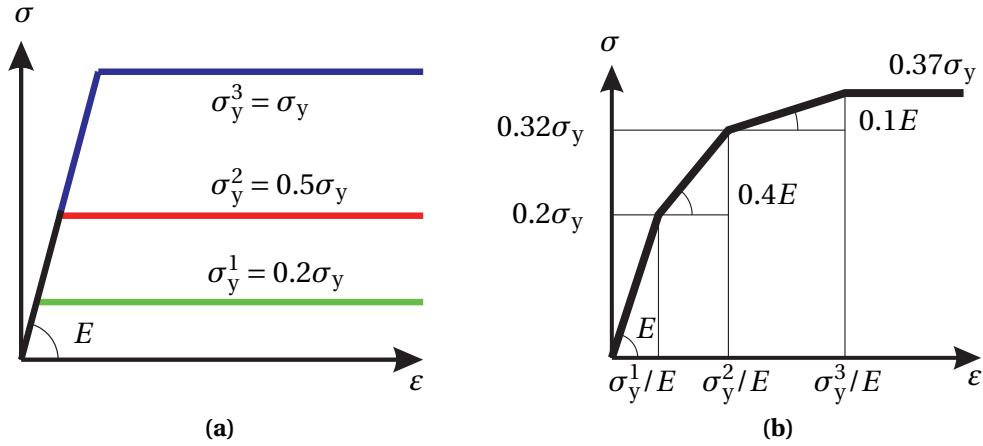


Figure 2.7 Construction of the stress-strain diagram for three rods:
 (a) stresses in rods; (b) average stress

The four intervals (Fig. 2.7b) separated by yield strength points of three rods can be explained in details:

1. In the first interval, all rods deform elastically until the applied strain reaches the smallest yield strain ε_y^1 .
2. The increase of the strain amplitude leads to the accumulation of plastic deformation in the first rod which maintains constant stress for $\varepsilon \geq \varepsilon_y^1$:

$$\sigma^1 = 0.2\sigma_y$$

Hence, the diagram of average stress in the second interval has a smaller slope. The stress can be computed by the following equation:

$$\sigma = 0.6(0.2\sigma_y) + (0.3 + 0.1)E\varepsilon \quad (2.4)$$

The end point of the second interval can be calculated by substituting the yield strain $\varepsilon_y^2 = 0.5\sigma_y/E$ of the second rod into Eq. (2.4):

$$\sigma = 0.6(0.2\sigma_y) + (0.3 + 0.1)(0.5\sigma_y) = 0.32\sigma_y$$

3. In the third interval, only the last rod deforms elastically, while the total strain is smaller than its yield strain ε_y^3 . The average stress can be computed in a similar way, considering constant stresses in the first and the second rod:

$$\sigma = 0.6(0.2\sigma_y) + 0.3(0.5\sigma_y) + 0.1E\varepsilon = 0.27\sigma_y + 0.1E\varepsilon$$

4. Finally, the Masing model implies a special case in which all components deform plastically which doesn't change the stresses in the entire model. In the given example, the average stress in the fourth interval is constant:

$$\sigma = 0.6(0.2\sigma_y) + 0.3(0.5\sigma_y) + 0.1\sigma_y = 0.37\sigma_y$$

Although the rods are described by the simplest ideal elasto-plastic model, the non-linear macroscopic behavior can be captured. Furthermore, one can describe the experimentally obtained material response by the Masing-type model through the decomposition of the stress-strain diagram. For example, a piece-wise linear interpolation of stress-strain curve allows us to identify the properties of components by the slope of linear pieces.

2.1.2 Statistical distribution of yield stress

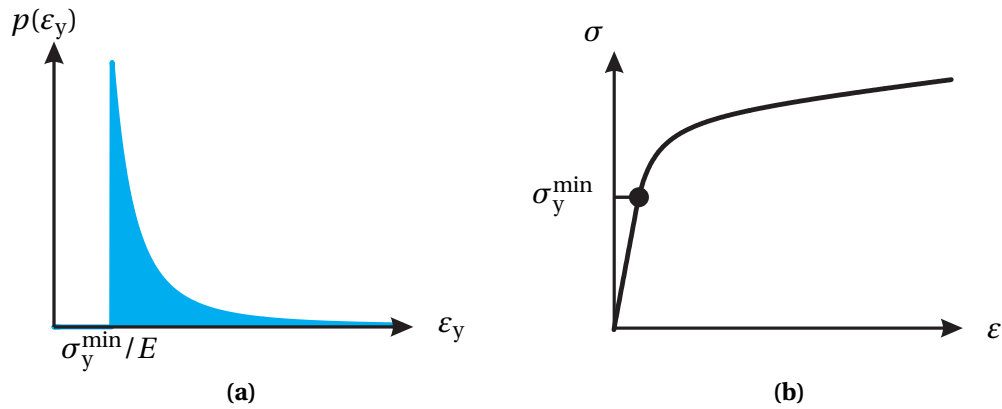


Figure 2.8 Continuous Masing-type model: (a) probability density function; (b) stress-strain diagram

To introduce a smooth stress-strain diagram, one can represent the model by an infinite number of rods with a continuous distribution of yield strength. In this case a homogenized stress under the monotonic displacement-controlled load can be calculated using the following equation [70]:

$$\sigma = \Phi(\varepsilon) = E \left[\varepsilon - \int_0^\varepsilon (\varepsilon - \varepsilon_y) p(\varepsilon_y) d\varepsilon_y \right] \quad (2.5)$$

where $p(\varepsilon_y)$ is a probability density function of yield strains. The function may represent different heterogeneous properties such as the distribution of crystalline lattice orientations. Anyway, it must be defined taking into account the following property:

$$\int_0^\infty p(\varepsilon_y) d\varepsilon_y = 1$$

In the given example, the exponential law is used in order to formulate the probability density function of yield strains as shown in Fig. 2.8a. The function has non-zero values in range $[\sigma_y^{\min}/E, \infty]$, while zero values are preset elsewhere. It allows us to formulate the purely elastic behavior for stresses less than the minimal yield stress parameter σ_y^{\min} . The corresponding integrated stress response is illustrated in Fig. 2.8b with respect to applied strains.

The obtained stress-strain diagram illustrates the presence of similar yielding and hardening effects as observed in experimental mechanical tests. However, to illustrate the Bauschinger effect, the calculation of the entire hysteresis loop must be accomplished. Besides the tensile loading step, the unloading step should be evaluated as well. In the discussed model, this task can be simplified taking into account the Masing principle.

2.1.3 Masing principle

The Masing principle follows from equation (2.5) after some transformations explained in [36, 70]. It states that an unloading curve of the hysteresis loop coincides with the loading curve plotted in double inverse axes:

$$\sigma^{\text{unload}} = \sigma_0 - 2\Phi\left(\frac{\varepsilon^*}{2}\right) \quad (2.6)$$

where $\varepsilon^* = \varepsilon_0 - \varepsilon$ and $\sigma^* = \sigma_0 - \sigma$ are inverse axes of the unloading curve with its origin at the end of the initial loading curve $(\varepsilon_0, \sigma_0)$. The integration function Φ is described by Eq. (2.5).

Thus, in Fig. 2.9, the red curve provides the solution of the Masing model under a monotonic load as discussed early. The blue line is obtained by double scaling and reversing. The obtained curve clearly demonstrates the Bauschinger effect as the inequality of the yield strength points for loading and unloading.

This principle is often applied in material science and engineering in order to predict hysteresis loops, using data from experimental tensile tests. Often, the conducting of a compression test after tensile one is complicated or not feasible. In this case, it is possible to perform a cyclic analysis with the estimated hysteresis loop.

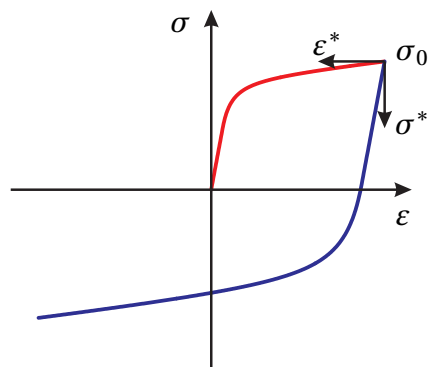


Figure 2.9 Illustration of the Masing principle

A thorough investigation of more advanced microstructure's models can reveal simple methods and techniques to estimate material behavior in complex structures, avoiding computationally expensive simulations. For this reason, the model of Voronoi tessellation is considered as a close representation of the real polycrystalline microstructure.

2.2 Voronoi diagram

The Voronoi diagram is a method of the decomposition of space into a set of convex cells based on the distribution of site points. In the three-dimensional case, cells of the Voronoi tessellation are separated by convex planar polygonal faces in which all points on the single face lie equidistantly from the two nearest sites. Three neighboring cores determine an edge as an intersection of three faces. Vertices of these edges are equidistant from at least four nearest site points. Therefore, any point inside the cell of the Voronoi diagram lies closer to the site of that cell than to any other site, as described in the following definition [107]:

$$R_k = \{x \in X \mid d(x, P_k) \leq d(x, P_j) \forall j \neq k\} \quad (2.7)$$

where x is a point in space X involved in distance function d along with the coordinates of site points P . Voronoi cell R_k is described by index k , while the rest of site points are denoted using index j .

The two-dimensional Voronoi diagram is represented by convex polygonal cells separated by linear edges in the same manner as in the 3D case. Thus, the vertices of the tessellation are characterized by the same distance to at least three neighboring sites, while all points on edges between the vertices are equidistant from the nearest two sites.

Likely, the first Voronoi diagram was drawn by the French mathematician René Descartes in 1644, based on his circular vortex theory of planetary motion [91]. Thus, in Fig. 2.10, Descartes' understanding of the gravitational influence of stars is illustrated. However, the first mathematical declaration was made in 1850 by the German mathematician Gustav Lejeune Dirichlet for the investigation of two- and three dimensional quadratic forms [27]. For this reason, the tessellation is often titled after him. Five years later, in 1855, the first documented practical application can be found in the report of John Snow [92] regarding the 1854 cholera epidemic in London. Besides the source of disease, he has observed the statistical correlation between the people's

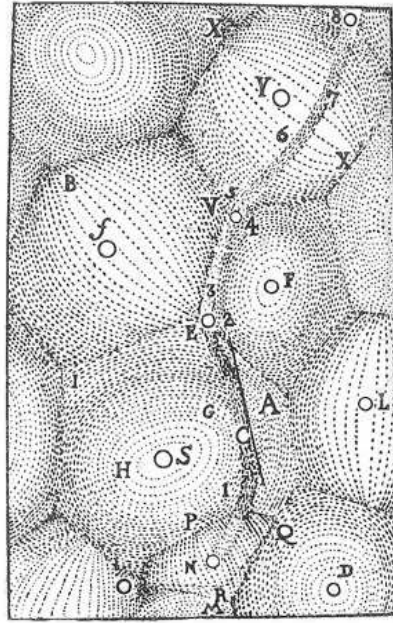


Figure 2.10 Gravitational influence of stars

proximity to a water pump and the number of deaths. On account of simplicity and clarity, the diagram found application in many fields under different names in the following years. Nevertheless, it is mostly named after the Ukrainian mathematician Georgy Voronoi, due to his work on the generalization of Dirichlet's results for an arbitrary dimension [102] in 1907. A significant contribution for the understanding of his work was made by the Soviet mathematician Boris Delaunay in publication [25] dedicated to Voronoi's honor in 1934. The Voronoi diagram has gained high popularity in science because of its frequent appearance in nature (Fig. 2.11) and technology (Fig. 2.12). Moreover, since the development of microscopy allows us to capture the microstructure of materials, the applicability of the Voronoi tessellation in metallurgy is confirmed as well.

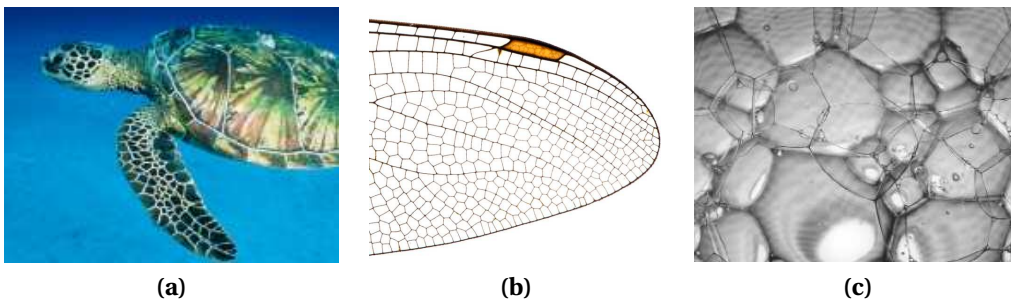


Figure 2.11 Voronoi diagrams in nature: (a) sea turtle; (b) dragonfly wing; (c) soap bubbles (pictures are taken from [5, 49, 82])

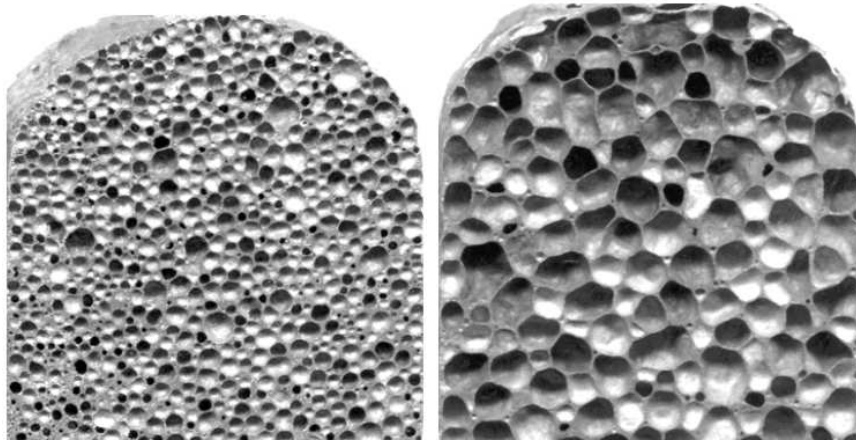


Figure 2.12 Samples of aluminum/silicon-carbide foam [34]

2.2.1 Algorithms overview

Despite the perfect theoretical description of the Voronoi diagram, the calculation of cells over an arbitrary distribution of site points remained complicated, due to the lack of algorithms and computational power. The construction of geometrical model requires the computation of a large number of intersections in order to provide the coordinates of vertices, configuration of edges and faces.

Particularly, the algorithm of the generation of the Voronoi tessellation can be simplified by assuming a regular distribution of site points which introduce repeatable pattern cells. For example, the first models based on this approach can be found in crystallography. Figure 2.13 illustrates the example of a cubic crystal structure analyzed by Paul Niggli [66] in 1927. The similar Wigner–Seitz cells were described in 1933 by Eugene Wigner and Frederick Seitz [106], and further often applied in material science.

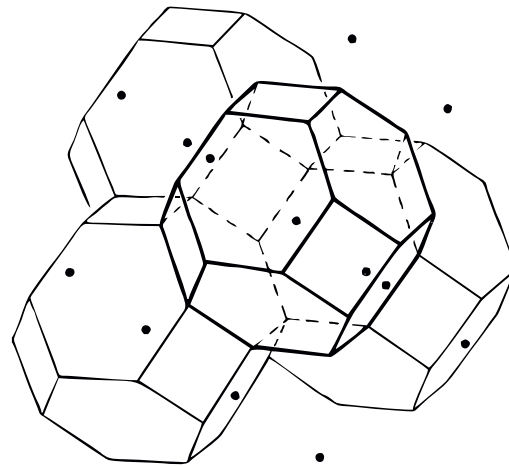


Figure 2.13 Cubic crystallites[66]

However, sufficient methods and techniques to calculate irregular structures have started developing with the beginning of the computer era. For instance, an efficient realization of the sweep line algorithm for the generation

of the Voronoi diagram was proposed by Dan Hoey and Michael Ian Shamos [84] in 1975, considering two-dimensionality. Later, in 1986, another sweep line algorithm was developed and implemented on programming language C by Steven Fortune [30]. Due to high efficiency, the Fortune's algorithm is still widely used, being implemented in different programming languages including C++, Java, Python, etc.

Besides the sweep line algorithms, the common approach to generate a Voronoi diagram is based on its duality with the Delaunay tessellation as shown in Fig. 2.14. The figure represents cells of the Voronoi diagram by red lines, while triangles of the Delaunay tessellation are plotted by dotted black lines. The duality property states that one tessellation can be obtained from other. Thus, the edges of the Delaunay triangulation connect the nearest site points of the Voronoi diagram as highlighted for example by green dotted lines in Fig. 2.14. Therefore, connecting the couples of neighboring Voronoi sites, one constructs the Delaunay triangulation. Likewise, the Voronoi diagram can be obtained from the Delaunay tessellation. A circumcenter of a triangle defines the Voronoi vertex as shown in example in Fig. 2.14 by a green circumcircle and cross.

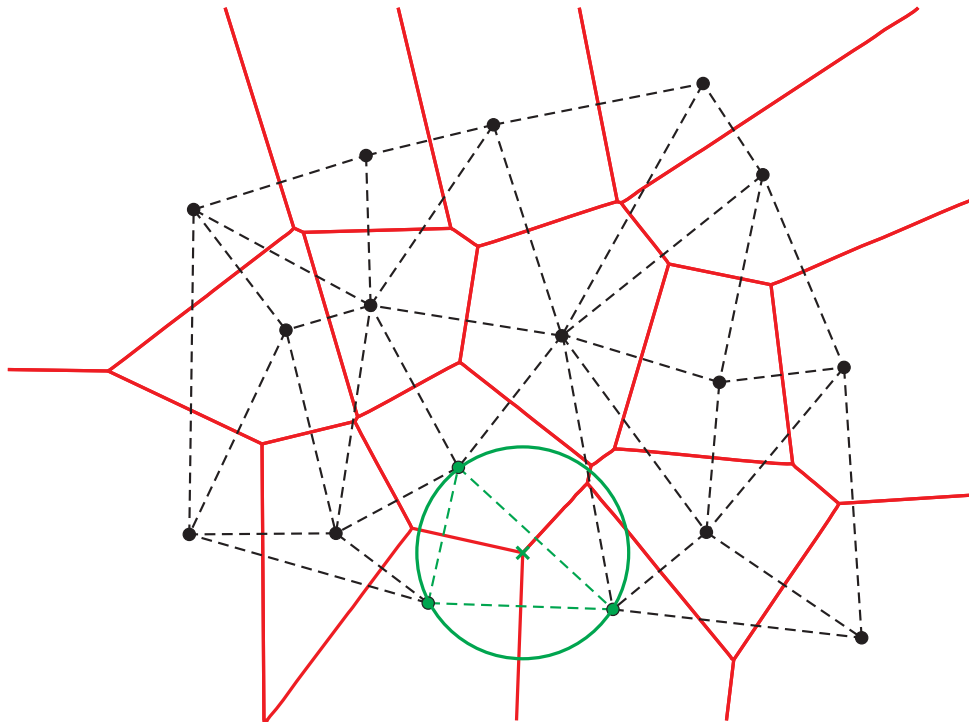


Figure 2.14 Duality of the Voronoi diagram and Delaunay tessellation

To generate the Delaunay tessellation, different technics can be involved.

For example, the open-source library `qhull` computes a 3D Delaunay tessellation by the modified convex hull algorithm called QuickHull algorithm [9]. Furthermore, it can reconstruct the Voronoi diagram, taking into account the duality with the Delaunay triangulation.

The discussed sweep line and the `qhull`'s algorithm provide the exact solution of the Voronoi diagram, which may require high computational costs. Another approach with a flexible efficiency can be found in the works [7, 100], in which the Voronoi diagram is represented by a discrete raster map as shown in Fig. 2.15. The Voronoi sites, which are represented by red voxels in the figure, are added into the initially empty map. Then, empty voxels around the Voronoi sites get the cell number they belong to according

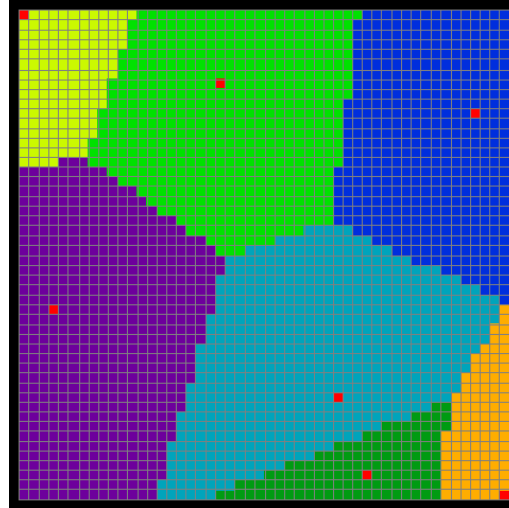


Figure 2.15 Raster Voronoi diagram to the incremental isotropic propagation algorithm [37]. As one of the advantages of this approach, the resulting map represents a ready to use 3D hexahedral or 2D quadrilateral finite element mesh, while other algorithms require the generation of a geometrical model at first. The resolution of the map characterizes the relationship between performance and accuracy. For example, a high density of voxels supposes a longer computational time, but the shape of the obtained cells is near to smooth. Contrariwise, the low resolution of the Voronoi diagram ensures a shorter generation time, assuming sharp grain borders. Anyway, the applicability of this method for the modeling of polycrystalline microstructure is questionable because of unclear formulation of grain boundary thickness.

An additional overview on the history, modifications and construction algorithms concerning the Voronoi diagram can be found in papers [6, 31].

2.2.2 Cell-based generation algorithm

The modeling of a polycrystalline microstructure with the Voronoi diagram has special requirements which are not covered by the mentioned algorithms. For instance, a sweep line approach computes 2D tessellations, while three-dimensionality is needed. The `qhull` library supports up to four dimensions,

but provides an inconvenient output data structure. Moreover, the necessity to introduce a criteria of the geometry's validity requires a synchronous verification and construction of Voronoi cells, as will be discussed further. For these reasons, the cell-based computation of the Voronoi diagram is preferred.

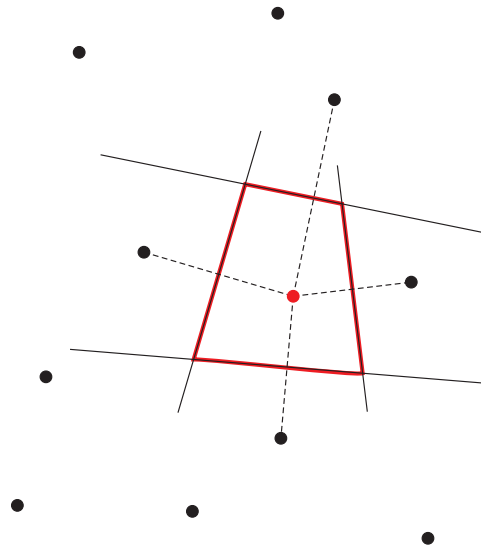


Figure 2.16 Formation of the cell by cutting with half-space planes

The convenient algorithm to calculate the Voronoi diagram is implemented in open-source library `Voro++` by Chris H. Rycroft in programming language C++ [80]. Unlike the mentioned solutions, this library computes each Voronoi cell separately from other cells. The algorithm can be explained in Fig. 2.16, where the construction of one cell is illustrated on the example of a red site point. The rest of the Voronoi diagram is calculated cell-by-cell in a similar way. At the beginning, each cell fills the entire volume of a container. Sequentially, the excess parts of the cell are cut off by half-space planes represented by black lines. These planes are equidistant to the cell's site point and neighboring sites. Therefore, the faces of the cell can be constructed as shown by red lines in the example. Finally, the following information is printed out for each cell separately in order to generate geometrical and finite element models of solid grains:

- Coordinates of the site point
- Absolute or relative coordinates of vertices
- Faces described by vertex sequences

In comparison with common solutions like the qhull library and the Fortune's algorithm, this library demonstrates lower efficiency because of a large number of repeatable operations. Particularly, the time of generation was reduced, due to the ignoring of remote site points and an advanced memory management. Moreover, a cell-based construction algorithm can be parallelized. Since cells are calculated independently, the generation of a Voronoi diagram can be performed in the multithread mode. It may decrease the computational time in few times depending on the number of threads. An especially promising improvement can be expected using the graphical processing unit (GPU) in which a large number of threads is available.

Anyway, the generation of random Voronoi diagrams with few a thousands grains can be performed in a reasonable time. The modeling of larger structures is senseless by the reason of the inability to simulate them with the FEM. Thus, the generation of a finite element mesh and the conducting of the analysis require more computational power than the construction of Voronoi cells.

In the present work, the programming code of the library Voro++ was significantly modified in order to introduce a special functionality such as the modeling of finite-thickness grain boundaries, excluding of the geometrical singularities, etc. For example, the verification of the cell's geometry is implemented within the cell's calculation kernel as a part of the randomized incremental Voronoi Diagram (RIVD) algorithm. Unlike the library's original construction algorithm, the RIVD allows to generate a Voronoi diagram, taking into account specified criteria like the minimal edge length, proximity to surface and the angle between edges. However, short edges and other unacceptable geometrical singularities may appear in the offset faces of the grain boundary layer, as discussed in next section. For this reason, the calculation of grain boundaries was implemented within the Voro++ library as well.

2.2.3 Grain boundary layer

Besides the shape of grains, the modeling of a polycrystalline microstructure implies the description of the grain boundary region. Being defects of the microstructure, grain boundaries engender a wide range of microscopic effects which influence on the macroscopic response. For example, the Hall-Petch effect states the dependence of the yield strength on the grain size, due to the fact that boundaries inhibit a dislocation movement between grains, as was independently discovered by Hall [41] in 1951, and Petch [72] in 1953.

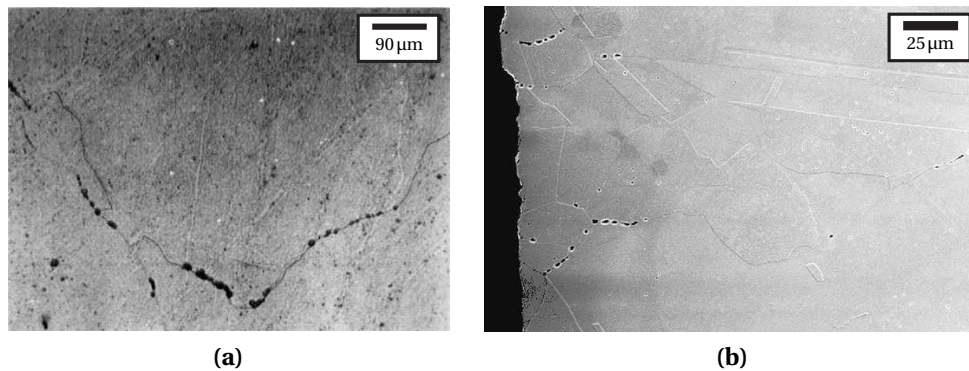


Figure 2.17 Cavities in grain boundaries: (a) magnesium-aluminium alloy [89]; (b) copper polycrystal [108]

Furthermore, as shown in [52, 77], the grain boundary sliding is a mechanism of creep which was explained by diffusion of vacancies along boundaries.

Taking into account the suggestion that grain boundaries have the thickness of a few atomic layers made in the works [17, 18], one can assume zero physical thickness. This assumption is widely used in the numerical modeling, due to a simple implementation within the finite element analysis. For instance, this approach can be found in several publications on simulations of intergranular fracture [86, 87] and diffusion creep [11, 93]. However, nucleation and growth of cavities often occur in grain boundaries under creep [21, 98] and fatigue [89] conditions, especially at elevated temperatures. As shown in Fig. 2.17, cavities occupy a certain volume which makes the assumption of zero-thickness questionable. The common solution to introduce a boundary layer with finite thickness is based on an interface model, as shown on the example of the cohesive zone approach in [88], among many others.

On the other hand, the modeling of a solid boundary layer with finite-thickness allows us to clearly represent the area of the interface's influence. To perform FEA, different standard and special-purpose volumetric finite elements are available. For example, cohesive or XFEM elements can be used to simulate a crack propagation. Anyway, a geometrical model of grains and grain boundaries must be generated at first. Therefore, different meshing techniques can be involved afterwards.

The construction of finite-thickness grain boundaries in a randomized Voronoi diagram is a challenging task, taking into account the arbitrary shape of grains. The probably easiest way to obtain a solid boundary layer is based on the moving of Voronoi vertices. Two approaches can be considered, as

shown in Fig. 2.18. The first one is based on the shrinking of vertices with respect to the site or mass center of a cell, as demonstrated in Fig. 2.18a. This method confers an advantage on the ability to introduce the dependence on the grain size using different scaling coefficients. Fig. 2.18b illustrates the second approach, where grains are moved apart by the isotropic expansion of the Voronoi sites. Since the relative coordinates of vertices are given for each cell separately, the rigid transition of cells can be performed without any additional recalculations. Therefore, higher efficiency is attained by using the second approach, while the method of shrinking requires the scaling of all vertices in the model. Anyway, both methods generate similar structures with empty space between the grains. The solid of grain boundaries can be obtained by the subtraction of solid grains from a homogeneous container.

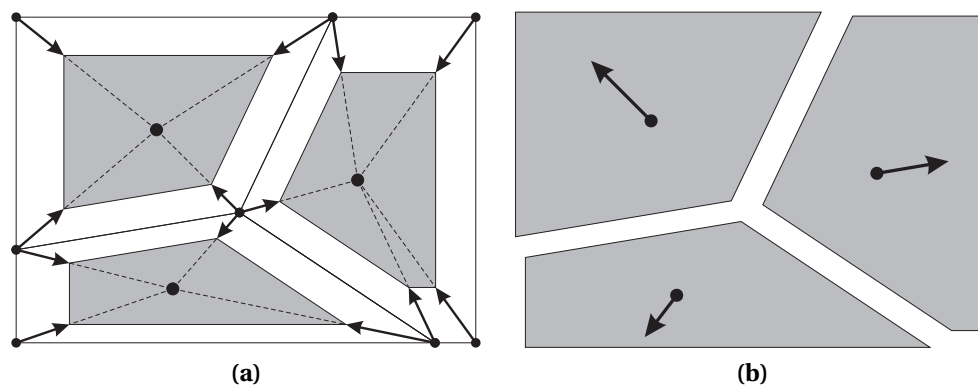


Figure 2.18 Transformation of grains: (a) shrink vertices; (b) move grains

For the reason that the boundary layer is represented by a single solid, the generation of a regular mesh is complicated, due to the large number of faces connected under different angles. Such a structure is not meshable with extrusion, sweep or revolution techniques, which can create prisms and hexahedrals. Therefore, one has to generate tetrahedral elements by the free meshing algorithm. Despite the inapplicability of special-purpose finite elements, the free meshing technique is commonly used in the modeling of a polycrystalline microstructure. For example, the cavity growth model based on the stiffness matrix degradation approach is implemented with standard tetrahedral continuum elements [69], where normal and shear directions were introduced by a discrete local coordinate system.

In addition to meshing difficulties, both methods provide an unclear definition of the boundary layer's thickness. It makes the analysis of a

polycrystalline microstructure inaccurate because of different thicknesses in the model.

In this work, another approach based on the offsetting of the faces by a specified distance is proposed. Taking into account the convexity of cells and the planar convex polygonal shape of faces, one can reconstruct the Voronoi cell with shifted faces. Unlike the mentioned algorithms, the proposed one calculates a position of the offset vertex through the intersection of three planes, as shown in Fig. 2.19, where three Voronoi faces with a common vertex P are illustrated.

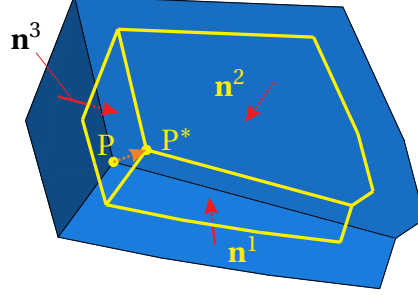


Figure 2.19 Offset of faces

Considering normals $\mathbf{n}^i(n_x^i, n_y^i, n_z^i)$ and coordinates of vertex $P(x_P, y_P, z_P)$, the point-normal form of the plane equation can be described for each face:

$$n_x^i x + n_y^i y + n_z^i z - d_i = 0 \quad (2.8)$$

with $d_i = n_x^i x_P + n_y^i y_P + n_z^i z_P$.

Introducing the offset distance u_i , a position of the required vertex $P^*(x_{P^*}, y_{P^*}, z_{P^*})$ is characterized as the intersection of three planes by the following equation:

$$\begin{pmatrix} n_x^1 & n_y^1 & n_z^1 \\ n_x^2 & n_y^2 & n_z^2 \\ n_x^3 & n_y^3 & n_z^3 \end{pmatrix} \begin{pmatrix} x_{P^*} \\ y_{P^*} \\ z_{P^*} \end{pmatrix} = \begin{pmatrix} d_1 + u_1 \\ d_2 + u_2 \\ d_3 + u_3 \end{pmatrix} \quad (2.9)$$

By repeating this procedure for each vertex of the cell, one can construct new faces, as shown by yellow line in the example. Therefore, the original Voronoi faces represent a middle-surface of grain boundaries. For instance, Fig. 2.20a demonstrates three grains with an identical thickness of the grain boundaries. In the 2D case, boundaries are represented by trapezoids, while in the 3D case polygonal prisms are given between grains. The sweep mesh technique well suits for the generation of prism or hexahedra finite elements in boundaries solids with clearly defined top and bottom facets. Hence, the debonding behavior can be implemented with a cohesive zone model or other surface separation techniques which allow us to simulate intergranular fracture. In the case where an interface model is not compatible with multi-layer boundaries, one can consider a model with the single layer, as shown in Fig. 2.20b. Therefore, junctions should be represented in another way

or assumed to be negligible. For example, volume fraction of unmeshed junctions in a polycrystal with 500 grains and the thickness of 3% of the grains size is approximately equal to 0.1%.

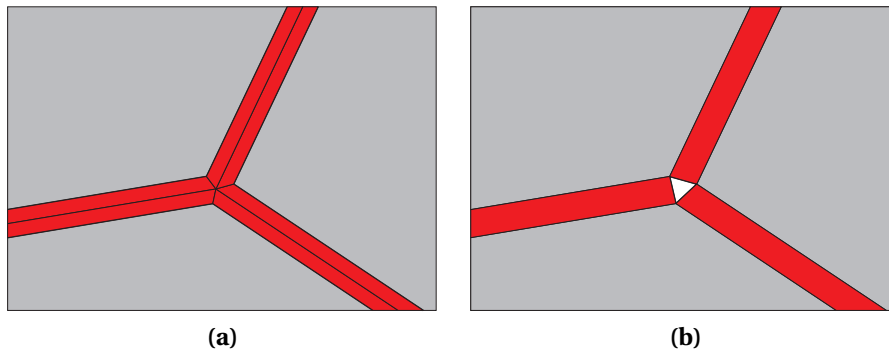


Figure 2.20 Grain boundaries: (a) double-layer; (a) single-layer

The main advantage of this approach is the clear definition of the boundary layer thickness for each face of the grains. Besides the parametrical analysis of polycrystalline aggregates, it facilitates the simulation of different microstructural phenomena. For instance, the dependence on grain size or crystalline lattice mis-orientation can be introduced in grain boundaries.

However, the implementation of the offsetting algorithm withstands several difficulties in the geometrical and finite element modeling. For example, unlike the scaling approach, the offset operation may create a self-intersecting circuit of edges. It is caused by the presence of short edges which can be transformed into a point, or even reversed during the transformation, as illustrated in Fig. 2.21. Since the same topology of top and bottom faces of prism boundaries is required, one should either remove short edges from the Voronoi diagram or decrease the offset distance. The second option limits the applicability of the method. For instance, the polycrystalline model with an identical specified thickness of the boundary layer may not be constructed if the offsetting distance is too large for certain boundaries. Nevertheless, short edges can be removed from the model as well as other geometrical singularities, as explained in the further sections.

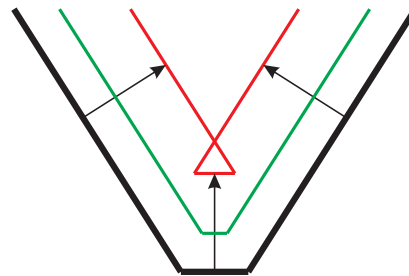


Figure 2.21 Short edge

2.2.4 Geometrical singularities

Short edges often appear in structures like the Voronoi diagram, taking into account a random distribution of site points, as it is shown in Fig. 2.22a. An example of the short edge in a 3D cell is illustrated in Fig. 2.22b as the common edge of four faces. These geometrical singularities complicate the preprocessing steps such as the offsetting of faces explained above, or the finite element meshing. For these reasons, a reduction of the geometrical singularities is an important step in the modeling of an arbitrary polycrystalline microstructure.

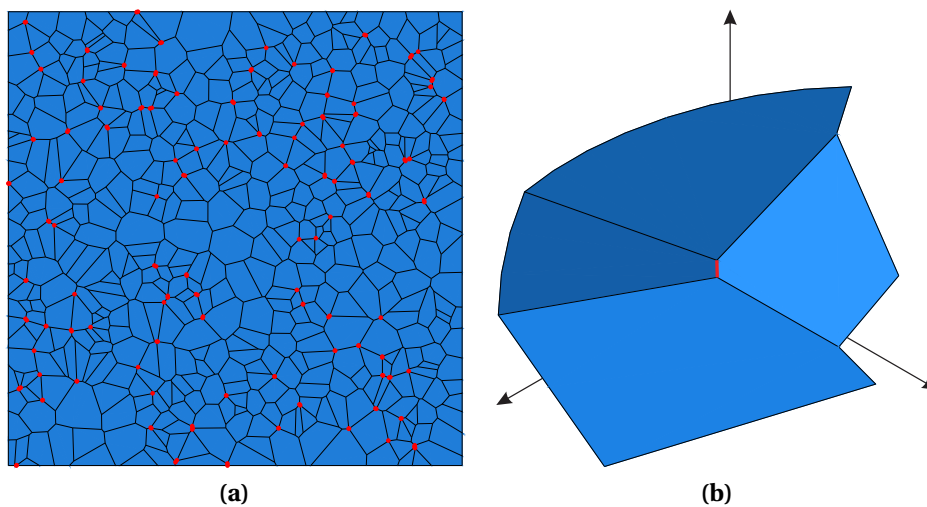


Figure 2.22 Examples of short edges: (a) 2D plate; (b) 3D grain

The regularization technique for removing short edges in the Voronoi diagram is implemented in the open-source library Neper [74]. It can be briefly explained in the example in Fig. 2.23a. The algorithm is based on replacement of the edge's couple of vertices by a single vertex at the middle. Hence, the adjacent faces should be reconstructed as shown in Fig. 2.23b, where two special cases can be considered. If a face shares both replacing vertices (top faces in the example), it remains planar, except for triangular faces which transform into lines. However, if the short edge is connected to face only by a single vertex (bottom face in example), one should take into account the fact that the middle point lies out of the plane. Therefore, the face should be replaced by two planar faces, as demonstrated in Fig. 2.23b.

However, the regularization technique is not suitable for the description of criteria such as the minimal angle between edges or the proximity of vertices to the surface of a specimen. The first criteria is required for the embedded Abaqus sweep mesh algorithm, where a minimal angle 30 degrees should

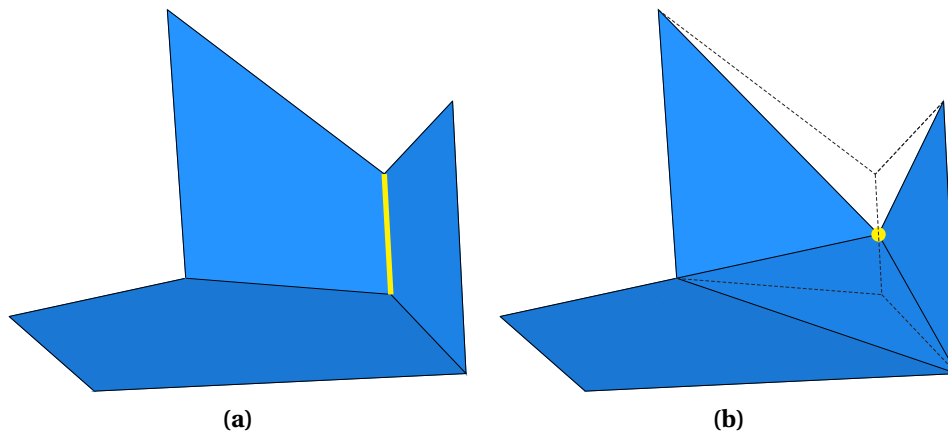


Figure 2.23 Regularization of the Voronoi diagram: (a) example of short edge;
(b) faces after reconstruction

be complied between the sides and the base of prisms. The second criteria allows us to improve the meshing of boundaries on a surface of the cylindrical polycrystalline model, as explained in the Section 2.3.1.

Anyway, the solution of the Voronoi diagram uniquely follows from the source distribution of site points. For instance, any vertex in the diagram is equidistant to at least four site points in 3D, and three site points in the 2D case. Therefore, in order to obtain Voronoi cells without geometrical singularities, the appropriate distribution of site points must be generated.

A similar problem was resolved in the work [105] which is focused on the generation of a meshable planar Voronoi diagrams. The two introduced criteria are the angle between edges and the aspect ratio, involved in the so called "trial-and-error" algorithm. It calculates a series of randomized realizations of the diagram until a suitable distribution is obtained. For the reason that a complete distribution of site points should be regenerated on every attempt, the low efficiency and convergence of this approach are observed. For instance, the generation of 1000 grains in 2D takes about 10^6 trials.

In the present work, a similar approach based on the "trial-and-error" idea, but implemented within a randomized incremental algorithm, is proposed and explained below. This approach allows us to generate an arbitrary Voronoi diagram that corresponds to the prescribed geometrical criteria. Despite the longer generation time, the algorithm is well suitable for the modeling of polycrystals, due to the absence of undesirable geometrical singularities in the model, and other advantages.

2.2.5 Randomized incremental algorithm

To represent a polycrystalline microstructure by the Voronoi diagram, one generates the randomized distribution of site points. Each site refers to the convex cell with planar faces according to the description of the Voronoi tessellation explained in beginning of the chapter. Taking into account the arbitrary shape of cells, different geometrical singularities such as short edges and small angles are observed. For this reason, a set of geometrical criteria is introduced in order to verify constructed faces and edges. In the case of an insufficient form of the cells, the distribution of Voronoi cores should be modified. However, singularities can appear in either the reconstructed model because of the interconnectivity and complexity of the Voronoi tessellation. Therefore, the generation of random site points, along with the recalculation of a tessellation, should be performed in several attempts until an appropriate diagram is obtained.

The mentioned example of the "trial-and-error" method [105] recalculates an entire Voronoi diagram a considering new distribution of random site points on each attempt. The efficiency of this approach is low since passed cells are regenerated as well as failed. Instead of the full reconstruction, one may adjust particular sites in the distribution in order to regenerate only the required failed cells.

In this work, the randomized incremental Voronoi diagram [38] (RIVD) is involved as the groundwork of the cell-based "trial-and-error" method. Unlike the standard generation algorithm, the RIVD is constructed incrementally site-by-site. The iteration consists of three main steps: the insertion of a new site point, the calculation of the new cell, and the updating of neighboring cells. To compute the faces of a Voronoi diagram, one can use different libraries such as the Fortune's code, based on the sweep line technique, or qhull library, which uses the duality to the Delaunay tessellation. Both approaches compute an entire Voronoi diagram even to calculate certain cells, which disregards the advantages of the proposed algorithm. In contrast, the open-source library Voropp constructs each cell separately, as explained in Section 2.2.2. Due to the cell-based structure and open-source code, the Voropp library suits well for the implementation of the randomized incremental Voronoi diagram.

More evidently, the construction of RIVD can be demonstrated by the example in Fig. 2.24, where six random sites are inserted incrementally. According to the cell-based construction algorithm implemented by Chris Rycroft in the library Voropp, every cell of the Voronoi diagram is obtained

through the cutting of a container volume by half-space planes, which are equidistant to a couple of the cell's site and neighboring sites. In the example, the first cell occupies the entire container, taking into account the single site point in the distribution. In the next step, another cell is calculated considering the same initial state, but cropped using the half-space plane between two sites. Furthermore, the first cell should be reconstructed in the second step as well because of a non-actual geometry. Finally, the obtained face separates two cells, as illustrated by a red line in the figure. In the same way, the remaining sites are added into the Voronoi diagram incrementally. Besides the updated cells with reconstructed faces, one can observe several unmodified cells, represented by black site points in the figures. Ignoring these remote Voronoi cores allows us to reduce the amount of unnecessary calculations which decreases the computational time of a iteration, especially considering a large number of cells.

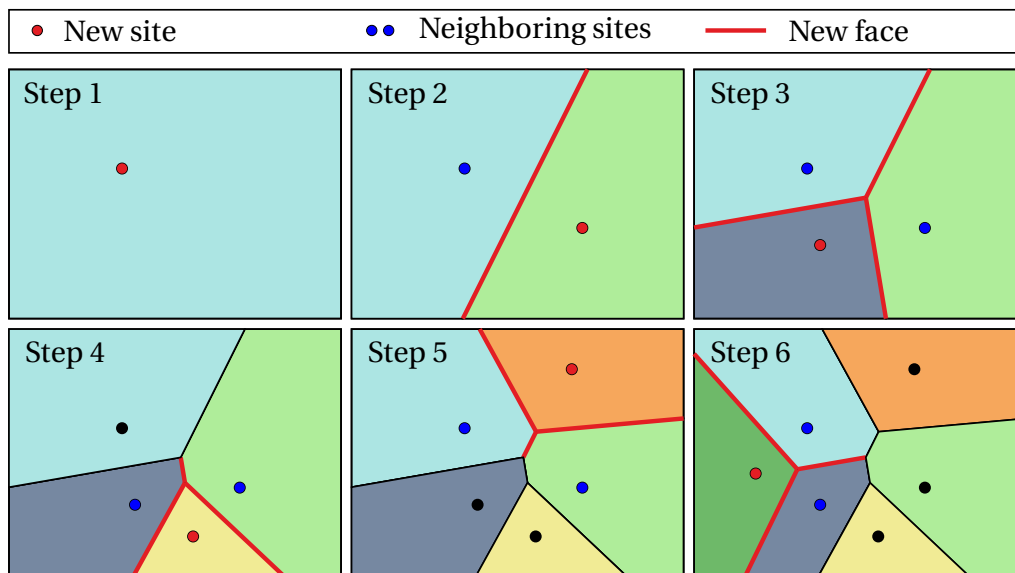


Figure 2.24 Construction of 6 cells with randomized incremental approach

For the reason that only certain cells are involved in the iteration, it is beneficial to implement the verification procedure as a part of the cell-based construction algorithm. If the criteria are not satisfied in the inserted or updated cell, the increment should be repeated considering another random position of the site point, but the same initial state of the diagram. Eventually, the suitable coordinates of a site point will be found which allows to continue with the construction of the Voronoi diagram by inserting the next site point. Hence, the algorithm is based on a combination of RIVD and the "trial-and-

error" method, as demonstrated by Fig. 2.25.

Despite the convenient cell-based architecture, the open-source library Voron++ was significantly redesigned to implement the developed algorithm. For instance, the original power management technique implies the computation of every cell consequently within the same block of memory. Standard generation approach has its advantages in the low memory usage, since

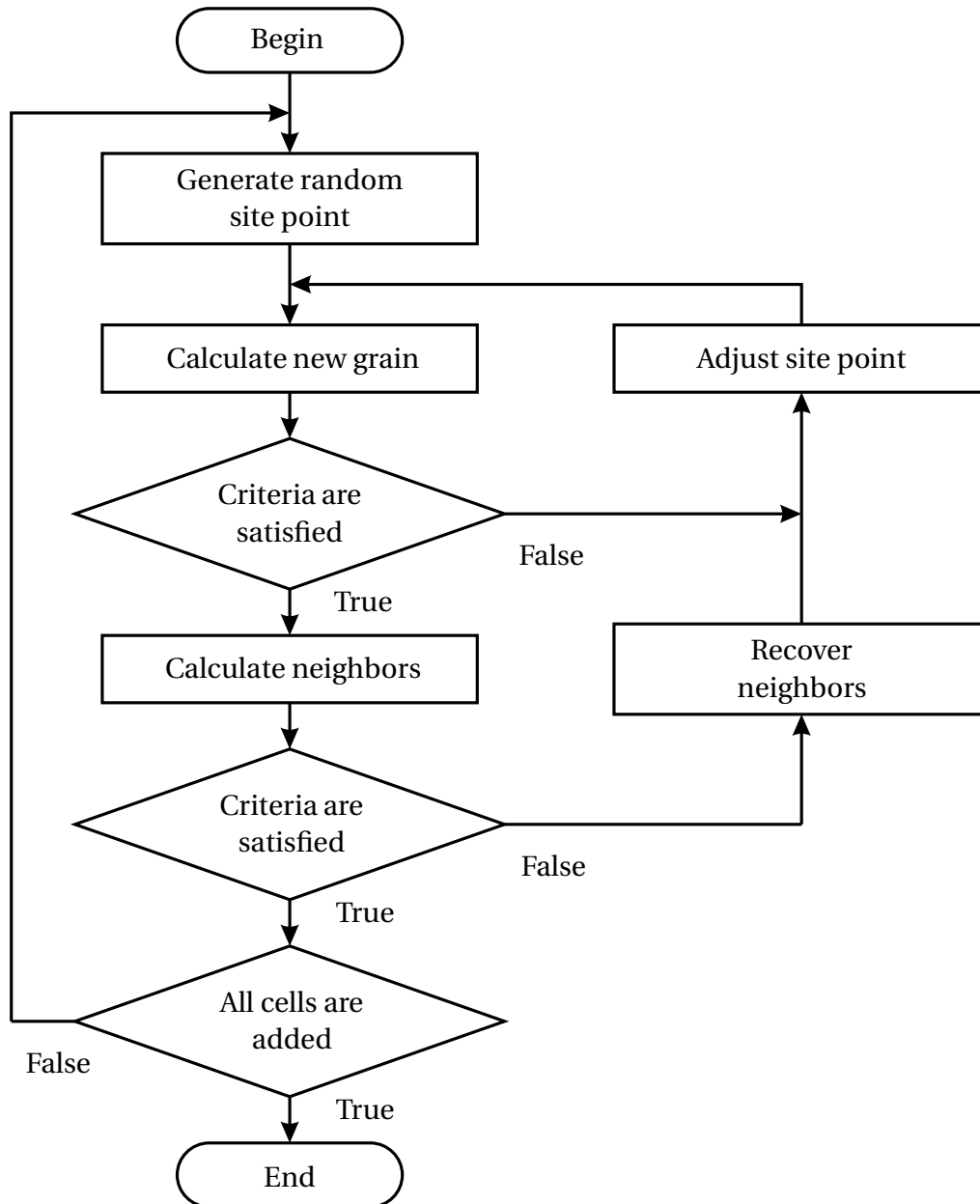


Figure 2.25 Algorithm of modified randomized incremental algorithm

each cell is constructed and printed out only once, whereas the incremental algorithm suggests the calculation and storing of cells in separate memory blocks, which reduces the amount of unnecessary operations. However, the modified code allows us to generate the randomized Voronoi diagram with required number of cells within a cubic container. As a criteria of verification, one can involve different geometrical properties such as:

- Length of edge
- Angle between faces
- Angle between edges
- Size or volume of grain
- Area of face

The strength of these criteria, along with number of cells, influences on convergence of the algorithm. For example, different threshold values of the edge length can be used to determine short edges. In Table 2.2, the computational time of the models with a different number of cells and a minimum length of edges is presented considering an average cell size of $40\mu\text{m}$. For the comparison with the standard algorithm, three models are generated considering the same number of cells, but the disabled criteria. As shown in Table 2.3, the model with 1000 cells consists of 12430 edges, where 40 edges have a length less than $0.1\mu\text{m}$. Using the proposed algorithm, the similar Voronoi diagram without edges shorter than $0.1\mu\text{m}$ was obtained in 2.62 seconds.

Table 2.2 Time of calculation of Voronoi diagram, s

Number of grains	Original	Minimum length of edges, μm			
		0.1	0.5	1	2
500	0.49	1.136	1.2	1.33	1.84
1000	1.0	2.62	2.95	3.6	6.677
2000	2.02	7.61	9.62	14.12	41.19

Despite the larger computation time of the Voronoi diagram, the efficiency of the entire framework is improved, due to a higher stability of the preprocessing and meshing steps. For example, the present work is focused on the modeling of a polycrystalline microstructure, assuming zero- or finite-thickness of the grain boundary layer. As discussed in Section 2.2.3,

Table 2.3 Number of edges of in Voronoi diagram

Number of grains	Shorter than threshold				Total
	0.1 μm	0.5 μm	1 μm	2 μm	
500	23	110	213	423	6081
1000	40	214	438	878	12430
2000	86	454	930	1824	25255

boundaries with finite-thickness are constructed by offsetting the faces inside. The method suggests the same topology of original and offset faces to generate prism finite elements using the sweep mesh technique. Due to the absence of short edges, the generation of valid geometrical and finite element models can be performed with a higher probability. However, the construction of boundaries with a required thickness may fault in several cases. Therefore, the offsetting of faces should be implemented within the cell-based construction algorithm of the Vorop++ library too. This approach allows us to regenerate cells with invalid boundaries in the same manner, using the "trial-and-error" method. In this case, the convergence of the generation depends on the offsetting distance, along with other mentioned criteria. Table 2.4 shows the averaged construction time of the models with a different number of cells and different thickness of boundary layer, where the average size of cells equals 40 μm .

Table 2.4 Generation time of Voronoi diagrams with grain boundaries, s

Number of grains	Thickness of boundary layer, μm				
	0.0	0.1	0.5	1.0	2.0
500	1.2	9.2	10.2	11	23
1000	2.95	25	28	55	87
2000	9.62	113	127	181	472

However, the performance of the library can be notably increased by using more advanced computational techniques. For instance, the cell-based programming code suits well for a multithreaded execution. Since cells are constructed independently, the generation of the Voronoi diagram can be parallelized. It allows to decrease the computational time by using several cores of the central processing unit (CPU). A particularly huge performance boost can be achieved with the graphical processing unit (GPU), where plenty of cores are available. Anyway, the amount of grains in the simulation of a polycrystalline microstructure within FEA is limited by a few thousands,

even though the simplest material model and coarse finite element mesh are considered.

In the case of a successful calculation, the library prints out the information about faces, edges, and vertices of the Voronoi diagram to generate geometrical and finite element models in CAD/CAE Abaqus.

2.3 Construction in CAD/CAE Abaqus

The simulation of structures within the Finite Element Analysis consists of three general steps: preprocessing, solving, and postprocessing. In the preprocessing step, the finite element model should be described along with the material behavior, time integration settings, loading and boundary conditions. The finite element solver calculates approximated displacements, stresses and strains in the model incrementally. Afterwards, the results of the converged solution are studied by numerical postprocessing techniques such as averaging, interpolation, etc. The full cycle of simulation can be performed using the well-known commercial CAD/CAE programs Abaqus, Ansys, Comsol, SolidWorks, and Nastran/Partan, or the open-source Calculix, which include the preprocessing module, solver and Visualization tools. Usually, embedded modeling functions in these programs demonstrate sufficient efficiency and usability for solving general problems, while the simulation of complex a material microstructure behavior requires more sophisticated approaches. On the other hand, the mentioned CAD/CAE programs provide access to certain features of modeling and simulation through the Application Programming Interface (API). Therefore, the functionality and performance can be improved for specific problems by using more advanced algorithms and programming codes. Hence, the software framework is developed and implemented to generate a polycrystalline microstructure in CAD/CAE program Abaqus version 6.12. Preprocessing functions, including geometrical modeling, are accessed by the Python Application Scripting Interface[3] (ASI), while the programming languages C++ and Fortran are involved in the postprocessing and material description respectively.

In the present work, the polycrystalline microstructure is represented by the 3D randomized Voronoi diagram with convex grains and planar polygonal faces. As discussed in the previous section, the diagram is computed by the modified open-source library Voro++ which constructs faces of finite thickness grain boundaries as well. The number of grains, offset distance, dimensions of the container, and geometrical criteria are input parameters

for the library. Every cell of the calculated Voronoi diagram can be described by the following data structure:

- Coordinates of site point
- Coordinates of Voronoi vertices
- Coordinates of offset vertices
- Sequences of vertices to describe convex polygonal faces

To generate a finite element mesh of the diagram, the corresponding geometrical model should be constructed at first. Considering the CAD/CAE program Abaqus, one can either import the model from a neutral geometrical file or create faces and solids with ASI. The first approach supposes that the model is generated by an external geometrical kernel and exported in a compatible file format, while in the second case the embedded geometrical modeling kernel is involved. Hence, the construction of the Voronoi diagram with the Abaqus Application Scripting Interface is more convenient and stable, due to its native modeling interface.

Solids of grains can be generated step-by-step, as shown as an example in Fig. 2.26. First of all, Voronoi vertices should be introduced with coordinates taken from Voropp library's output. Afterwards, the closed circuit of edges is described by connecting vertices in the described order using the Python ASI command "WirePolyLine". By applying the command "CoverEdges" on these edges, planar faces can be defined as illustrated in Fig. 2.26c. Finally, the Python ASI function "AddCells" performs a shell-to-solid transformation of the surrounding faces.

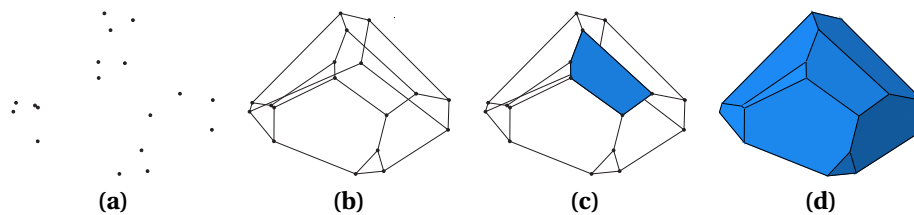


Figure 2.26 Construction of a grain step-by-step from vertices (a) to edges (b), faces (c), and solid (d)

Depending on the type of grain interaction model, one can construct solid Voronoi cells within a single part or in separate parts. In the second case, the contact behavior and mesh interface should be described between

grain solids, which influences on the convergence of the FEA. Instead, the consideration of single part implies the generation of a compatible finite element mesh which reduces computational time and costs. Moreover, the advanced grain interaction model can be introduced even in the single part, using a special material behavior within finite elements of grain boundary layer.

In the present work, two approaches of grain boundary modeling are considered. The first one is based on the generation of a polycrystalline microstructure assuming a zero-thickness boundary layer and perfectly bonded grains. In this case, the statistical analysis of the deformation state in randomized samples with a large number of grains can be performed in a reasonable time. Despite the simplest anisotropic grain material model, a complex macroscopic material response is achieved, as shown in the Chapter 5. Nevertheless, the intergranular fracture of a polycrystal is analyzed, considering the cohesive separation behavior in finite-thickness grain boundaries.

2.3.1 Shape of polycrystal

As discussed in the introduction chapter, the analysis of a heterogeneous deformation state in micro-parts under tension is the main goal of this thesis. The application of the scale separation method in the mentioned length scale is questionable because of the unclear existence of a representative volume element. Therefore, the entire polycrystalline model should be generated, taking into account a large number of grains, the shape of the sample, and realistic boundary conditions. Therefore, an influence of the discrete anisotropic microstructure can be investigated in the bulk and surface regions.

However, the most libraries including Voro++ calculate the Voronoi diagram within a basic container such as prism, cylinder, etc., while the modeling of holes, notches, and cuts can be useful in the analysis of a microstructure under a non-uniform deformation gradient. For this reason, the geometrical cutting operation is used to obtain the required shape of the polycrystal, as shown in Fig. 2.27 on the example of a cylindrical bar. Thus, this operation allows us to subtract the template solid model from the unit cell geometrical model of the Voronoi diagram.

However, the finite element meshing of polycrystals with a complex shape stands several difficulties in the case of finite-thickness grain boundaries. Since the sweep mesh technique is considered within the boundary layer,

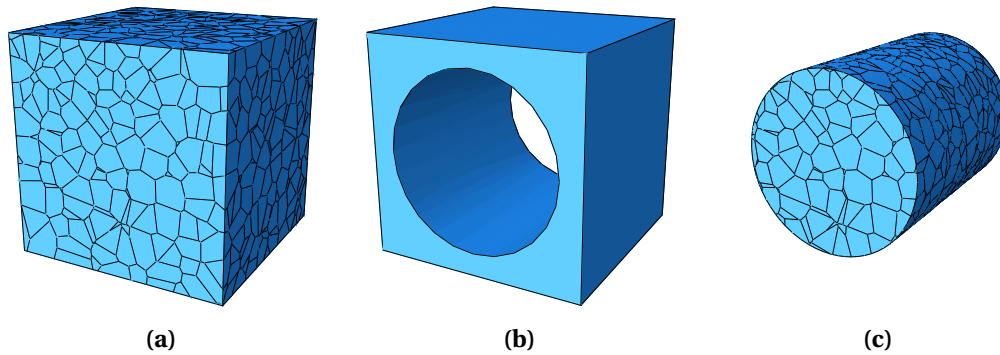


Figure 2.27 Formation of the cylindrical polycrystal (c) through cutting of the source unit cell model (a) by the solid template model (b)

the prism topology should be maintained in either updated polycrystal. As shown on the example of fig. 2.28, certain grain boundaries may become unmeshable after cutting, which makes the sweep algorithm unapplicable. Basically, such boundaries may appear in the case where a vertex of the Voronoi diagram lies closely to the suggested surface of the polycrystal. Therefore, the stability of the meshing can be improved by introducing the minimal distance of the Voronoi vertices to the surface as an additional criteria for the randomized incremental Voronoi algorithm, as it was explained in the Section 2.2.5.

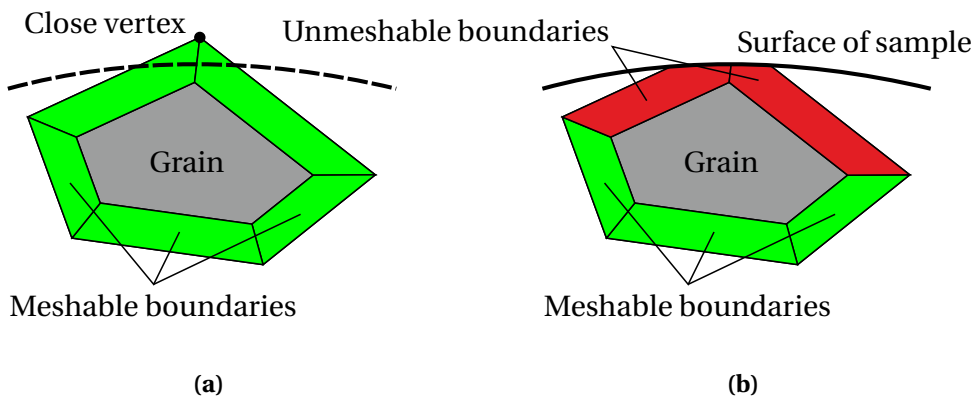


Figure 2.28 Unmeshable boundaries on the surface of polycrystal: (a) source model; (b) model after cutting

Despite the fact that geometrical criteria worsen convergence of the generation of a Voronoi diagram an obtained model is well meshable as

described further.

2.4 Finite element model

To generate the finite element model of polycrystalline aggregates, the type of elements should be considered depending on the material modeling approach and involved meshing algorithms. For the reason that elastic and inelastic material behavior is described in grain interior within the classical continuum theory, the standard volumetric elements can be used to represent solids of grains. Due to the complex arbitrary structure of Voronoi cells and polygonal faces, one can generate a tetrahedra inside the grains rather than prisms or hexahedrons. It can be done by using the free meshing algorithm implemented in many generation tools, including the Abaqus Mesh module.

Assuming zero-thickness boundaries, the embedded Abaqus mesh generator is more convenient. However, the modeling of a finite-thickness grain boundary layer shows the lack of performance and usability in the Abaqus Application Scripting Interface. For this reason, the open-source mesh generator Gmsh [33] was involved in the generation of the tetrahedra inside the grains within the finite-thickness approach, while the embedded Abaqus meshing tool is used otherwise. Moreover, an efficient sweep meshing algorithm is developed and implemented to insert prism elements between grains in the case of the finite-thickness boundary layer.

2.4.1 Finite-thickness boundary layer

The simulation of intergranular fracture implies the modeling of damage and debonding mechanisms in the grain boundary layer. It can be done by using standard or special-purpose finite elements. Anyway, the sweep meshing technique should be applied in boundaries to generate a layered mesh. It allows us to clearly assign top and bottom facets of elements onto debonding surfaces, which is especially important in the cohesive zone modeling approach. Since a tetrahedral mesh is considered in the grain bulk, one should generate triangular prisms between grains instead of hexahedrons.

The proposed offsetting algorithm (Section 2.2.3) results in two layers of solid boundaries between grains. The faces of the Voronoi diagram in this case become a mid-surface of the boundary layer. Due to an identical topology of the source mid-face and opposite target faces, one can generate prism finite

elements as demonstrated in Fig. 2.29, where the source triangular mesh is extruded along the sides of the boundaries.

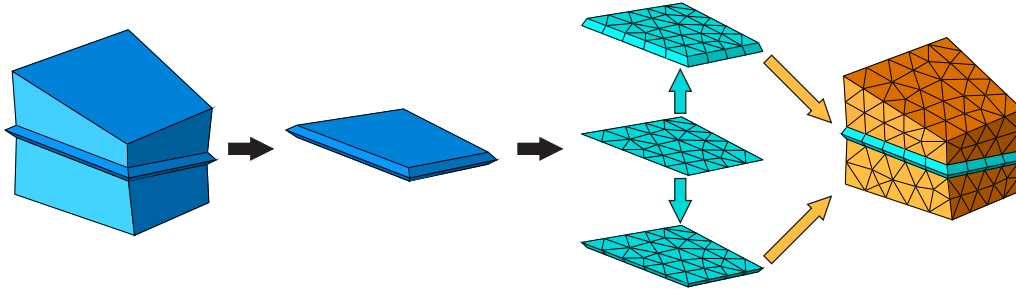


Figure 2.29 Example of meshing two grains and boundaries between them

By repeating this procedure for each face of the Voronoi diagram, the finite element model of grain boundary layer can be generated as shown in Fig. 2.30 on the example of a cylindrical bar with 500 grains.

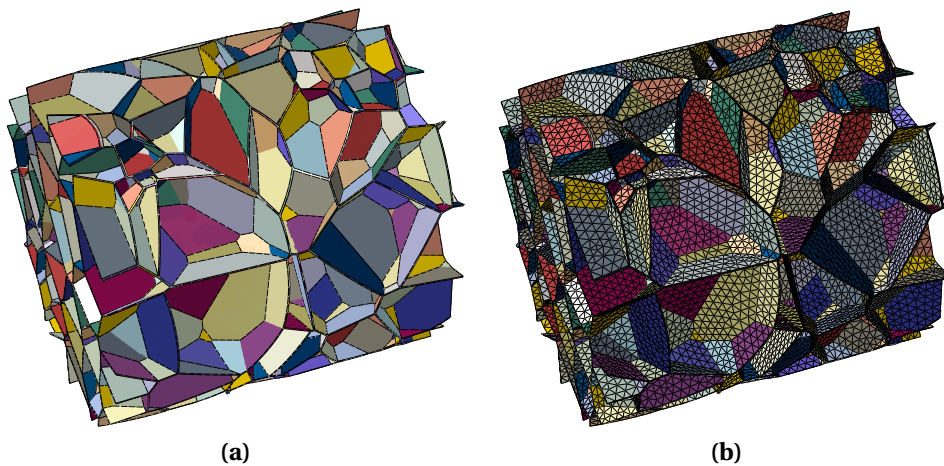


Figure 2.30 Geometrical (a) and finite element (b) models of finite-thickness grain boundaries in cylindrical polycrystal with 500 grains

The sweep meshing algorithm is implemented in the CAD/CAE program Abaqus as well as the free meshing algorithm and can be accessed by the Application Scripting Interface too. However, the embedded algorithm shows an inappropriate generation time in the case of a large number of grains. For instance, prism elements in the given example (Fig. 2.30) were generated in approximately 30 minutes using the Abaqus embedded function. For this reason, another sweep algorithm was developed and implemented in programming language Python.

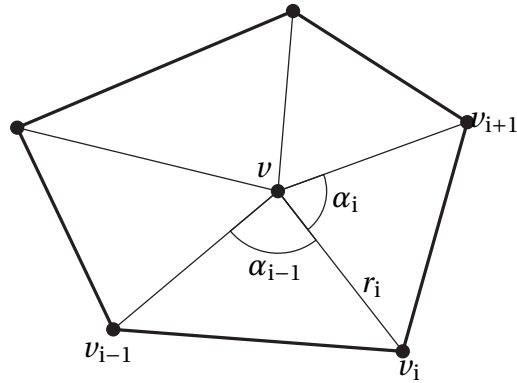


Figure 2.31 Calculation of point's barycentric coordinates

The proposed meshing technique is based on the interpolation of the nodal coordinates on the target face with respect to the coordinates of nodes on a master triangular mesh of the source face considering a barycentric coordinate system. The barycentric method allows us to represent coordinates of an arbitrary point within a polygon by a set of weight coefficients according to the position of the vertices, as shown in Fig. 2.31. It was firstly introduced for triangles in 1827 by Möbius [63] and, later, in 1975, for convex polygons by Wachspress [103]. The broad overview on the history, applications, and algorithms can be found in report [44]. The so-called mean value coordinates are given in [29] and formulated for every vertex of the polygon by the following equation:

$$\omega_i(v) = \frac{1}{r_i(v)} \left(\tan \frac{\alpha_{i-1}(v)}{2} + \tan \frac{\alpha_i(v)}{2} \right) \quad (2.10)$$

$$\lambda_i(v) = \frac{\omega_i(v)}{\sum_j \omega_j(v)} \quad (2.11)$$

By normalizing the barycentric coordinates with equation (2.11), one can perform affine transformations of the point together with a polygon such as translation, scaling, rotation, shear mapping, etc. The cartesian coordinates x, y, z of point v can then be interpolated among any other scalar field using the following equation:

$$F(v) = \sum_j \lambda_j(v) f_j \quad (2.12)$$

where f_j is a value of the interpolating field at vertex v_j .

For example, Fig. 2.32 illustrates the scheme of interpolation nodes during the transformation of the rectangle. In the same way nodes from the original Voronoi face can be translated onto the grain boundary's target face.

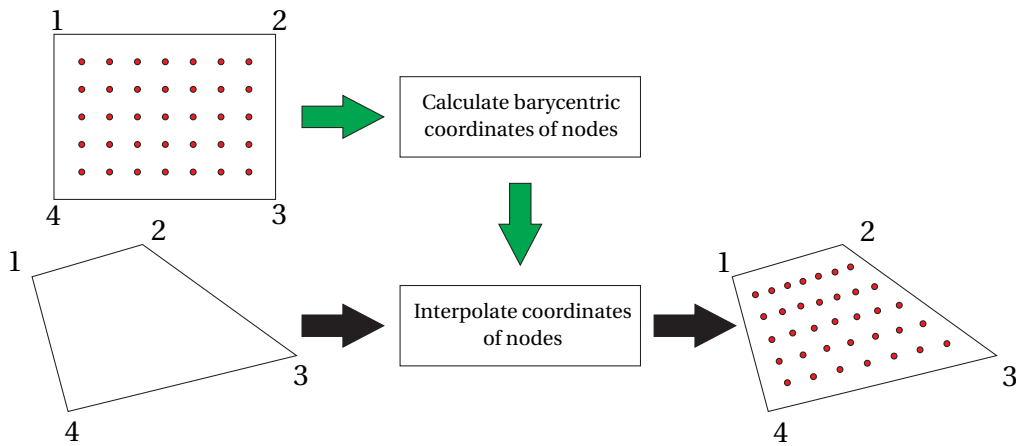


Figure 2.32 Scheme of interpolation and transformation of nodes

Taking into account the identical topology of triangles, the target mesh can be reconstructed as shown in Fig. 2.29. After the top and bottom facets of the elements are calculated, the layer of prisms can be described within an Abaqus input file.

By using the sweep algorithm based on a barycentric coordinate system, the time of meshing was significantly reduced. Nevertheless, the proposed approach is not applicable on boundaries with curved edges, which are observed in cylindrical polycrystals, models with holes, etc. For this reason, the finite element model of polycrystals with a complex shape is generated in a mixed mode using both the proposed one and embedded Abaqus meshing algorithms. The efficiency of algorithms can be compared in Table 2.5, where the time of mesh generation is demonstrated for grain boundaries in a cylindrical model and unit cell with 500 grains. A unit cell polycrystal consists of 5854 boundaries without curved edges, while in a cylindrical bar 776 boundaries with curved edges are identified among a total number of 5164.

Table 2.5 Generation time of finite element meshes in grain boundaries

	Cylinder		Unit cell	
	Only standard	Mixed	Only standard	Mixed
Standard	1866	31	2641	-
Barycentric	-	22	-	35
Total	1866	53	2641	35

To accomplish the generation of a finite element model, the grain interior is meshed as well. A compatible tetrahedral mesh can be obtained

considering the triangular facets on swept boundaries as a source for the propagation algorithm, as demonstrated in Fig. 2.29. For this purpose, the open-source mesh generator Gmsh was chosen because of its convenient importing and exporting features. Describing a triangular mesh, which was interpolated on the faces of grain boundaries, within a STL file (3D-Systems, Inc.), one can introduce the meshed faces of grains in the open-source program Gmsh. After the successful generation of tetrahedra, the corresponding nodal and elemental information can be printed out in a readable output file. Combining both grain and boundaries meshes in the Abaqus input file, the complete finite element model can be created.

However, besides the description of a finite element model, the material behavior of microstructure should be introduced in the Abaqus input file along with time integration settings, loading and boundary conditions.

2.4.2 Mesh dependence

In order to investigate an influence of the element size on the finite element solution of a polycrystalline model, the analysis of mesh dependence was performed assuming zero-thickness grain boundaries, perfectly bonded grains, and a purely elastic deformation. The example of finite element unit cell model with 1000 grains is represented in Fig. 2.33 along with boundary and loading conditions. Hence, by applying an identical displacement-controlled load u_x on the single side of unit cells and symmetric boundary conditions on three sides, the equal average strains ε_{xx} are obtained in polycrystals. On the other hand, a certain scatter of average stresses is observably because of the anisotropic elasticity inside grains and randomized material orientations. For this reason, a set of 50 randomized realizations of the polycrystalline microstructure was generated for unit cell models with 100, 500, and 1000 grains. Therefore, the statistical analysis of averaged stresses over polycrystal can be performed considering a different element size and number of grains.

Taking into account the average grain size of $40\ \mu\text{m}$, the most coarse mesh was generated with element size $30\ \mu\text{m}$, which corresponds to about 5600 elements in models with 100 grains, 35000 in the models with 500 grains, and 74000 elements in the models with 1000 grains. By decreasing the element size with step $1\ \mu\text{m}$, the finer finite element meshes were generated for every polycrystalline sample. Since the maximal number of elements is limited by computational abilities, the different minimum element size was reached in these models. Thus, the finest mesh for unit cell models with 100 grains was

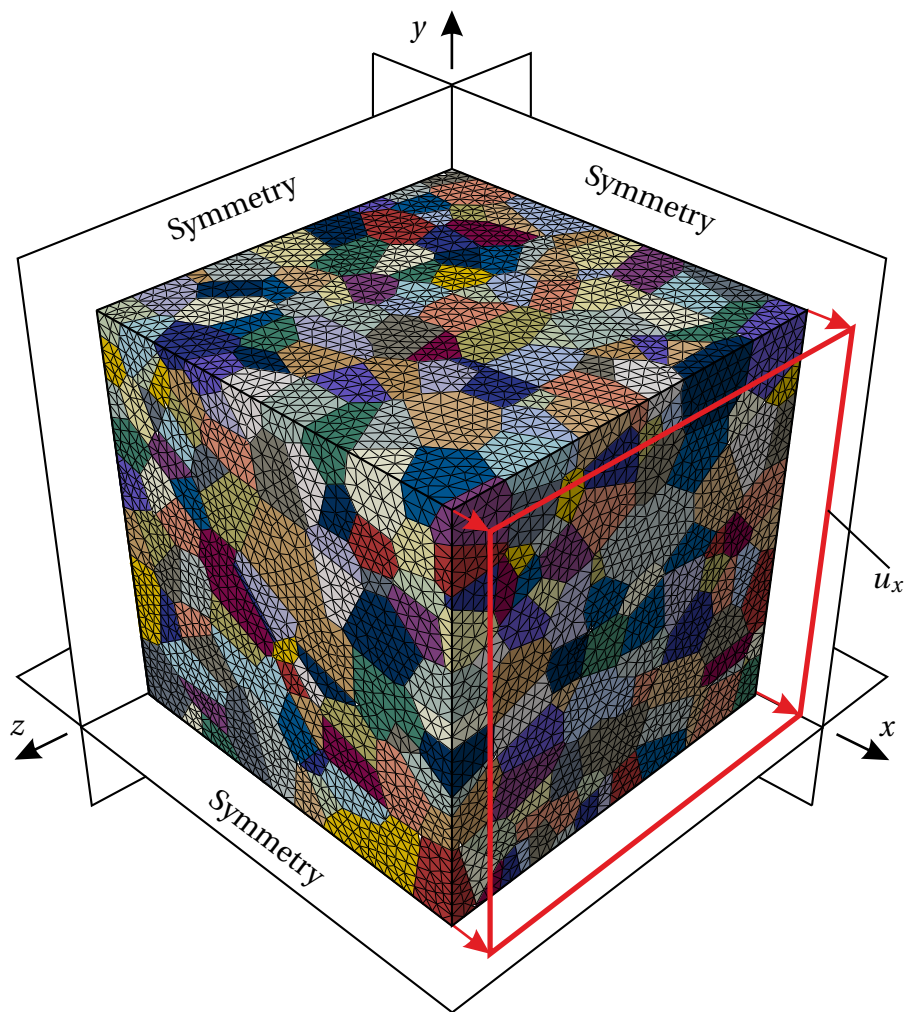


Figure 2.33 Example of the unit cell model with 1000 grains

achieved with the minimum element size $3\ \mu\text{m}$, which corresponds to about 1807000 finite elements. In the same way, the smallest size of $5\ \mu\text{m}$ along 217400 elements and $8\ \mu\text{m}$ along 1132500 elements are used in models with 500 grains and 1000 grains, respectively. However, the obtained simulation results for different number of grains can be compared within the single plot through a normalization of the total number of elements by number of grains, as represented in Fig. 2.34.

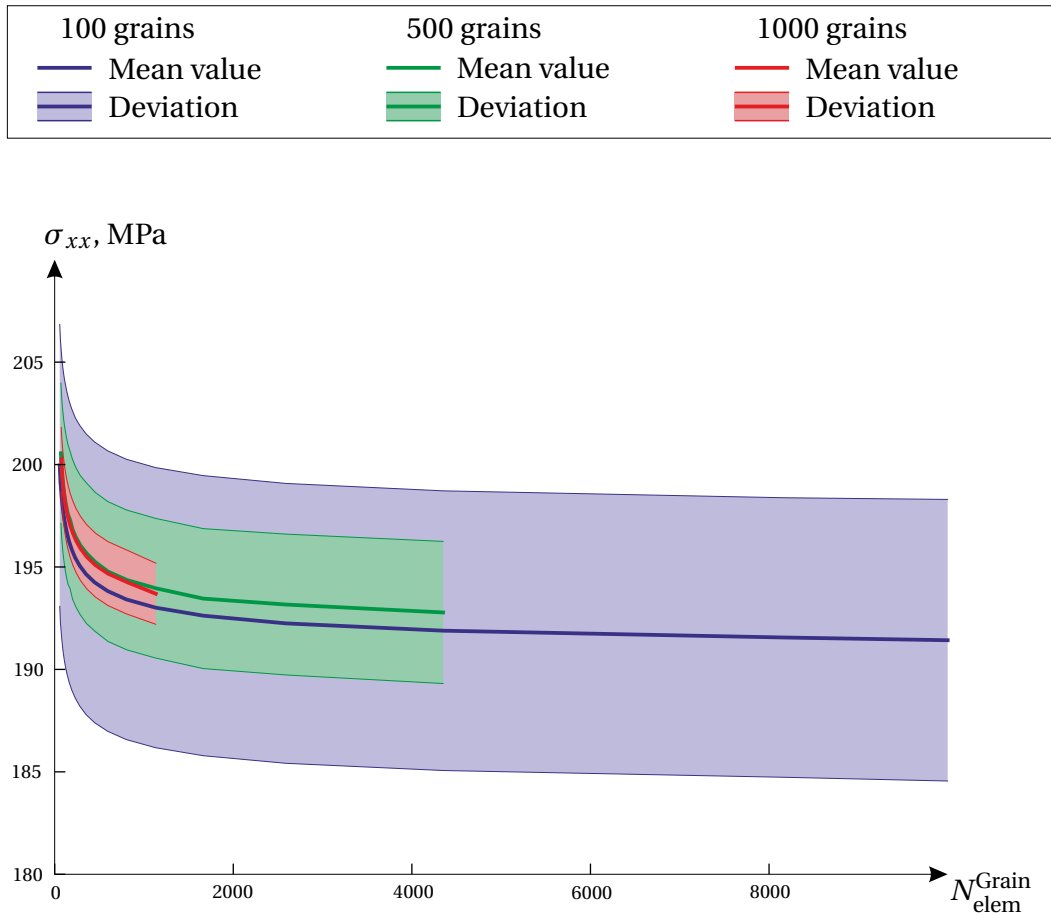


Figure 2.34 Dependence of averaged stresses and their deviation on the average number of elements per grain in the models with 100, 500, and 1000 grains

In the figure, horizontal axis shows the average number of elements per grains, while the vertical axis illustrates averaged stresses over polycrystal along the loading direction. By using the volumetric averaging, the homogeneous stress is obtained from a solution of every polycrystal. Afterwards, the mean value and deviation can be calculated for each finite element size by averaging of scalar homogeneous stresses over the 50 polycrystals. Thus, the mean value of stresses is represented by solid line, while the brushed area besides demonstrate the deviation of stresses. Blue, green, and red colors are introduced to distinguish results of analysis in models with 100, 500, and 1000 grains, respectively. The mean stress values in the polycrystals with 100 grains and 500 grains clearly show convergence to a certain value, due to decreasing of the element size and increasing of the number of elements

per grain. The simulation of models with 1000 grains has the same tendency, but requires finer mesh to achieve similar accuracy. Moreover, the solutions of models with 500 grains and 1000 grains are almost exact in the common range. Furthermore, one can observe dependence of the deviation on number of grains, which can explain a low representability of polycrystals with 100 grains.

Taking into account the obtained results of analysis for mesh dependence, the element size $8.4\mu\text{m}$, is used to generate finite element models in this work. The chosen elements size corresponds to approximately 1000 elements per grains. Despite the solution may have lower accuracy, the elastic and inelastic simulation of polycrystals with a large number of grains become possible. However, the influence of mesh dependence in analysis of multiple of polycrystals can be certainly reduced by maintaining the similar average number of elements per grains. Eventually, one can calculate an exact solution by decreasing a number of grains, adding of the computation power, etc.

Constitutive equations

The simulation of polycrystals implies the modeling of elastic and inelastic material behavior in grains and grain boundaries. To achieve the highest accuracy, one may describe all known micro-mechanical effects. For example, different theories such as the crystal-plasticity which can be used to formulate a microscopic behavior of crystalline lattice. However, it makes the finite element analysis unacceptably expensive from the computational point of view, especially considering a large number of grains. Therefore, the balance between representability and efficiency is the major question in the numerical simulation of a material microstructure. The present work is focused on the statistical analysis of polycrystals with macroscopic dimensions but a microscopic grain size. For this reason, the material behavior inside grains is formulated by a simplest viscoplastic anisotropic constitutive model, as shown further. The grain boundaries region is modeled in two different approaches: with a zero-thickness layer assuming perfectly bonded grains, and finite-thickness boundaries with a cohesive-type separation behavior.

3.1 Grain interior

The relationship between stresses and strains in grain interior is formulated by a generalized Hooke's law, which is represented in the following tensor form [65]:

$$\boldsymbol{\sigma} = {}^{(4)}\mathbf{C} \cdot \boldsymbol{\varepsilon}^{el} = {}^{(4)}\mathbf{C} \cdot (\boldsymbol{\varepsilon} - \boldsymbol{\varepsilon}^{in}), \quad (3.1)$$

where $\boldsymbol{\sigma}$ is the stress tensor, $\boldsymbol{\varepsilon}$, $\boldsymbol{\varepsilon}^{el}$, and $\boldsymbol{\varepsilon}^{in}$ are total, elastic and inelastic strain tensors respectively.

Assuming cubic type symmetry, it is convenient to decompose the fourth-rank elasticity tensor ${}^{(4)}\mathbf{C}$ using the three projection tensors ${}^{(4)}\mathbf{P}_i$ [13]:

$${}^{(4)}\mathbf{C} = \lambda_1 {}^{(4)}\mathbf{P}_1 + \lambda_2 {}^{(4)}\mathbf{P}_2 + \lambda_3 {}^{(4)}\mathbf{P}_3 \quad (3.2)$$

The projectors are given as follows:

$$\begin{aligned} {}^{(4)}\mathbf{P}_1 &= \frac{1}{3} \mathbf{I} \otimes \mathbf{I}, \\ {}^{(4)}\mathbf{P}_2 &= \sum_{i=1}^3 (\mathbf{g}_i \otimes \mathbf{g}_i \otimes \mathbf{g}_i \otimes \mathbf{g}_i) - {}^{(4)}\mathbf{P}_1, \\ {}^{(4)}\mathbf{P}_3 &= {}^{(4)}\mathbf{I} - {}^{(4)}\mathbf{P}_1 - {}^{(4)}\mathbf{P}_2, \end{aligned} \quad (3.3)$$

where \mathbf{I} and ${}^{(4)}\mathbf{I}$ are second- and fourth-rank identity tensors, \mathbf{g}_i , $i = 1, 2, 3$ is the orthonormal basis connected with the cubic lattice.

The material parameters λ_i were taken for a copper single crystal [32] and given in the Table 3.1.

Table 3.1 Elastic material properties of grains

λ_1	410	GPa
λ_2	47	GPa
λ_3	150	GPa

The components of the stiffness tensor can be recalculated as $C_{1111} = (\lambda_1 + 2\lambda_2)/3 = 168$ GPa, $C_{1122} = (\lambda_1 - \lambda_2)/3 = 121$ GPa, $C_{1212} = \lambda_3/2 = 75$ GPa.

Substituting the formulation of stiffness tensor (3.2) into the Hooke's law equation (3.4) the stress tensor can be evaluated in the following form:

$$\begin{aligned} \boldsymbol{\sigma} &= \frac{1}{3} \lambda_1 \text{tr} \boldsymbol{\varepsilon}^{el} \mathbf{I} \\ &+ \lambda_2 \left[\varepsilon_{11}^{el} \left(\mathbf{g}_1 \mathbf{g}_1 - \frac{1}{3} \mathbf{I} \right) + \varepsilon_{22}^{el} \left(\mathbf{g}_2 \mathbf{g}_2 - \frac{1}{3} \mathbf{I} \right) + \varepsilon_{33}^{el} \left(\mathbf{g}_3 \mathbf{g}_3 - \frac{1}{3} \mathbf{I} \right) \right] \\ &+ \frac{\lambda_3}{2} \left[\varepsilon_{12}^{el} (\mathbf{g}_1 \mathbf{g}_2 + \mathbf{g}_2 \mathbf{g}_1) + \varepsilon_{13}^{el} (\mathbf{g}_1 \mathbf{g}_3 + \mathbf{g}_3 \mathbf{g}_1) + \varepsilon_{23}^{el} (\mathbf{g}_2 \mathbf{g}_3 + \mathbf{g}_3 \mathbf{g}_2) \right] \end{aligned} \quad (3.4)$$

The power law type equation for the inelastic strain rate tensor can be given as follows:

$$\begin{aligned} \dot{\boldsymbol{\varepsilon}}^{in} &= \frac{3}{2} a \sigma_{eq}^{n-1} \left\{ \sigma_{11} \left(\mathbf{g}_1 \mathbf{g}_1 - \frac{1}{3} \mathbf{I} \right) + \sigma_{22} \left(\mathbf{g}_2 \mathbf{g}_2 - \frac{1}{3} \mathbf{I} \right) + \sigma_{33} \left(\mathbf{g}_3 \mathbf{g}_3 - \frac{1}{3} \mathbf{I} \right) \right. \\ &\quad \left. + \xi \left[\tau_{12} (\mathbf{g}_1 \mathbf{g}_2 + \mathbf{g}_2 \mathbf{g}_1) + \tau_{13} (\mathbf{g}_1 \mathbf{g}_3 + \mathbf{g}_3 \mathbf{g}_1) + \tau_{23} (\mathbf{g}_2 \mathbf{g}_3 + \mathbf{g}_3 \mathbf{g}_2) \right] \right\}, \end{aligned} \quad (3.5)$$

where a , n , and ξ are constants.

The equivalent stress can be formulated as follows:

$$\sigma_{\text{eq}}^2 = \frac{1}{2} [(\sigma_{11} - \sigma_{22})^2 + (\sigma_{11} - \sigma_{33})^2 + (\sigma_{22} - \sigma_{33})^2 + 6\xi(\tau_{12}^2 + \tau_{13}^2 + \tau_{23}^2)] \quad (3.6)$$

For $\xi = 1$ the von Mises equivalent stress for isotropic materials follows from (3.6).

The inelastic constants a , n , and ξ are given in the Table 3.2.

Table 3.2 Inelastic material properties of grains

a	$8.928 \cdot 10^{-12}$	$\frac{MPa^{-n}}{h}$
n	5.69	
ξ	0.01	

The described material behavior is implemented within Abaqus user subroutine UMAT in the programming language Fortran. An implicit time integration scheme was used to compute inelastic strains on each time increment using the backward difference Euler method [24, 65]:

$$\boldsymbol{\varepsilon}_{t+\Delta t}^{in} = \boldsymbol{\varepsilon}_t^{in} + \Delta t \dot{\boldsymbol{\varepsilon}}_{t+\Delta t}^{in}, \quad (3.7)$$

where the inelastic strain rate tensor at time $t + \Delta t$ is characterized by equation (3.5) with the updated stress tensor $\boldsymbol{\sigma}_{t+\Delta t} = \boldsymbol{\sigma}_t + \Delta \boldsymbol{\sigma}$.

Taking into account the Hooke's law (3.4) and the implicit time integration scheme, the increment of the stress tensor can be computed in the following way:

$$\Delta \boldsymbol{\sigma} = {}^{(4)}\mathbf{T} \cdot \cdot (\Delta \boldsymbol{\varepsilon}_t - \Delta \boldsymbol{\varepsilon}_t^{in}), \quad (3.8)$$

where the fourth-rank tensor ${}^{(4)}\mathbf{T}$ is:

$${}^{(4)}\mathbf{T} = \lambda_1 \mathbf{I} \otimes \mathbf{I} + {}^{(4)}\mathbf{K} - \frac{g \Delta t}{1 + g \Delta \boldsymbol{\sigma} \cdot \cdot {}^{(4)}\mathbf{M} \cdot \cdot \boldsymbol{\sigma}} \boldsymbol{\sigma} \cdot \cdot {}^{(4)}\mathbf{L} \otimes {}^{(4)}\mathbf{L} \cdot \cdot \boldsymbol{\sigma} \quad (3.9)$$

In the case of the power law type equation, the function g can be given as follows:

$$g = \frac{9}{4} \frac{a \sigma_{\text{eq}}^{n-1}}{\sigma_{\text{eq}}^2} (n-1) \quad (3.10)$$

The fourth-rank tensors ${}^{(4)}\mathbf{I}$, ${}^{(4)}\mathbf{K}$, ${}^{(4)}\mathbf{M}$ and ${}^{(4)}\mathbf{L}$ are given in Appendix A along with a generalized description of the function g .

The implicit time integration scheme significantly improves the convergence of the solution, due to high accuracy of the calculation derivatives. Therefore, higher time increments are allowed, which reduces the analysis time even though each iteration is computed longer.

3.2 Grain boundaries

As mentioned above, two different approaches of modeling grain boundaries are considered in this work. Assuming zero-thickness boundaries, grains are perfectly bonded, which does not require the description of a special behavior in the layer. Therefore, a polycrystal with a large number of grains can be simulated in an appropriate computational time. However, the second approach was proposed to investigate observed effects during damage propagation based on the example of intergranular fracture. For the reason that the present work is focused on the qualitative analysis, the cohesive zone technique with approximate properties is introduced because of the high efficiency and convergence of the standard Abaqus model. However, another material behavior can be applied in the future, due to the finite-thickness boundary layer and regular prism mesh. For example, the model of cavity growth within UMAT subroutine[69] introduces the behavior of grain boundaries under creep condition at an elevated temperature, considering the volumetric finite elements.

In this thesis, the boundary region is represented by a single layer of prism cohesive finite elements COH3D6, demonstrated on the example of Fig. 3.1a. The average grain size in the generated models is $40\ \mu\text{m}$, while the thickness of boundary layer T_0 equals to $1\ \mu\text{m}$.

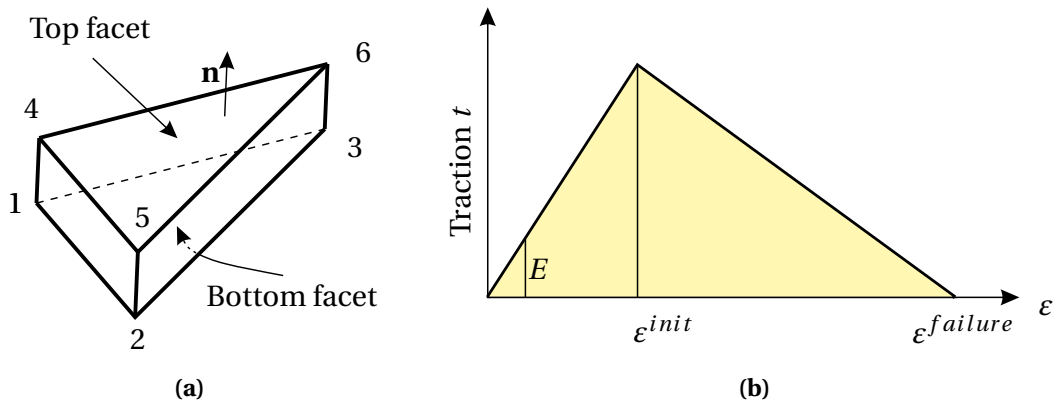


Figure 3.1 Cohesive finite element COH3D6: (a) configuration; (a) traction-separation law

According to the Abaqus Manual [2], cohesive behavior can be described with three traction-separation laws: one in normal direction and two in shear directions. The bilinear law consists of an elastic and inelastic range, separated by a damage initialization criteria, as shown in Fig. 3.1b. In the

elastic range, the cohesive behavior is described by the following equation:

$$\begin{Bmatrix} t_n \\ t_s \\ t_t \end{Bmatrix} = \begin{bmatrix} K_{nn} & 0 & 0 \\ 0 & K_{ss} & 0 \\ 0 & 0 & K_{tt} \end{bmatrix} \begin{Bmatrix} \varepsilon_n \\ \varepsilon_s \\ \varepsilon_t \end{Bmatrix}, \quad (3.11)$$

where t_n , t_s , and t_t are nominal traction stresses in three directions.

Matrix \mathbf{K} represents a stiffness matrix with zero values for uncoupled directions and stiffnesses K_{nn} in normal and K_{ss} , K_{tt} in shear directions. In this work, the constants of cohesive model $K_{nn} = 128$ GPa, $K_{ss} = K_{tt} = 48$ GPa are assumed. These values correlate with homogenized elastic properties of the unit-cell polycrystals with zero-thickness boundaries and perfectly bonded grains.

Normalized displacements ε_n , ε_s and ε_t follow from the separation displacements δ_n , δ_s , and δ_t , and the initial thickness T_0 :

$$\varepsilon_n = \frac{\delta_n}{T_0}, \quad \varepsilon_s = \frac{\delta_s}{T_0}, \quad \varepsilon_t = \frac{\delta_t}{T_0} \quad (3.12)$$

The inelastic separation of the cohesive layer starts when the damage initiation criteria MAXE (3.13) is reached.

$$\max \left\{ \frac{\langle \varepsilon_n \rangle}{\varepsilon_n^{\text{init}}}, \frac{\varepsilon_s}{\varepsilon_s^{\text{init}}}, \frac{\varepsilon_t}{\varepsilon_t^{\text{init}}} \right\} = 1 \quad (3.13)$$

The critical strains, which correspond to the damage initiation, are shown below for each direction:

$$\varepsilon_n^{\text{init}} = 0.0005, \quad \varepsilon_s^{\text{init}} = \varepsilon_t^{\text{init}} = 0.0025$$

Hence, the damage variable D evolves according to the linear evolution equation:

$$D = \frac{\delta_m^f (\delta_m^{\text{max}} - \delta_m^0)}{\delta_m^{\text{max}} (\delta_m^f - \delta_m^0)}, \quad (3.14)$$

where an effective displacement in cohesive element can be calculated as follows:

$$\delta_m = \sqrt{\delta_n^2 + \delta_s^2 + \delta_t^2} \quad (3.15)$$

In the equation (4.1), the values δ_m^0 and δ_m^f correspond to effective displacements at the damage initiation and failure, respectively. The term δ_m^{max} means a highest attained effective displacement.

The damage failure criteria is defined according to the mixed-mode energy-based approach $\delta_m^f = 2G^C/T_{eff}^0$, where the critical fracture energy is formulated by the Benzeggagh-Kenane (BK) form [12]:

$$\begin{aligned} G^C &= G_n^C + (G_s^C - G_n^C) \left\{ \frac{G_S}{G_T} \right\}^\eta \\ G_S &= G_s + G_t \\ G_T &= G_n + G_S \end{aligned} \quad (3.16)$$

$G_n^C = 0.032 \text{ Nmm}$ and $G_s^C = G_t^C = 0.3 \text{ Nmm}$ are the assumed critical fracture energies in the normal and two shear directions, respectively. The power $\eta = 1$ is considered.

In the case of inelastic separation, nominal stresses in three directions can be determined by using the following equations:

$$\begin{aligned} t_n &= \begin{cases} (1-D)\bar{t}_n, & \bar{t}_n \geq 0 \\ \bar{t}_n, & \text{otherwise} \end{cases}, \\ t_s &= (1-D)\bar{t}_s \\ t_t &= (1-D)\bar{t}_t \end{aligned}$$

where \bar{t}_n , \bar{t}_s , and \bar{t}_t are extrapolated from elasticity equation (3.11), considering zero damage.

For the reason that the stiffness of boundaries is characterized by homogenized elastic properties of the polycrystal, the separation of a cohesive layer depends on the effective stiffness of adjacent grains. As shown in the previous section, the single crystal possesses an anisotropic elastic and inelastic material behavior. Taking into account a random crystal lattice orientation, an effective stiffness of grains in the loading direction can be smaller, equal or larger. Therefore, different relations between deformations of grains and the grain boundary layer can be observed in the polycrystal. For instance, Fig. 3.2 illustrates two opposite cases of deformations in a bicrystal under tension and shear load. In the case where grains are stiffer than the boundary in between (Fig. 3.2a and 3.2b) the boundary deforms the most. Otherwise (Fig. 3.2c and 3.2d), higher deformation occurs inside the grains.

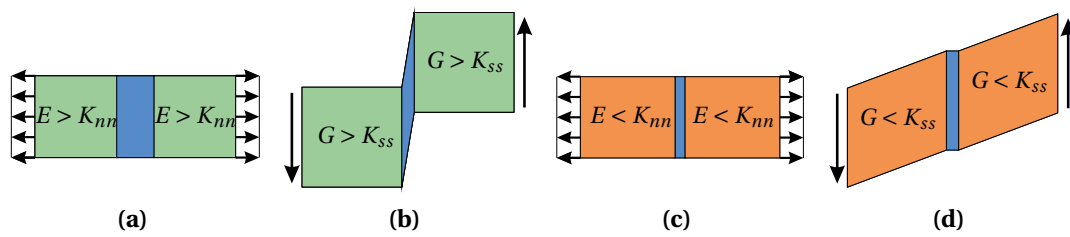


Figure 3.2 Examples of deformation of bicrystal in the tension and shear tests considering different relationship between the stiffness of grains (E and G) and stiffness of boundary (K_{nn} and $K_{ss} = K_{tt}$)

However, taking into account the viscoplastic material behavior inside grains, the significant redistribution of stresses can be observed, due to a local relaxation and damage accumulation, as will be shown in the Section 5.2.

CHAPTER

4

Postprocessing

The postprocessing of the results is the final step in the analysis of structures with the finite element method. Usually, it means the retrieving of stresses and strains at interesting nodes or finite elements. Considering randomized

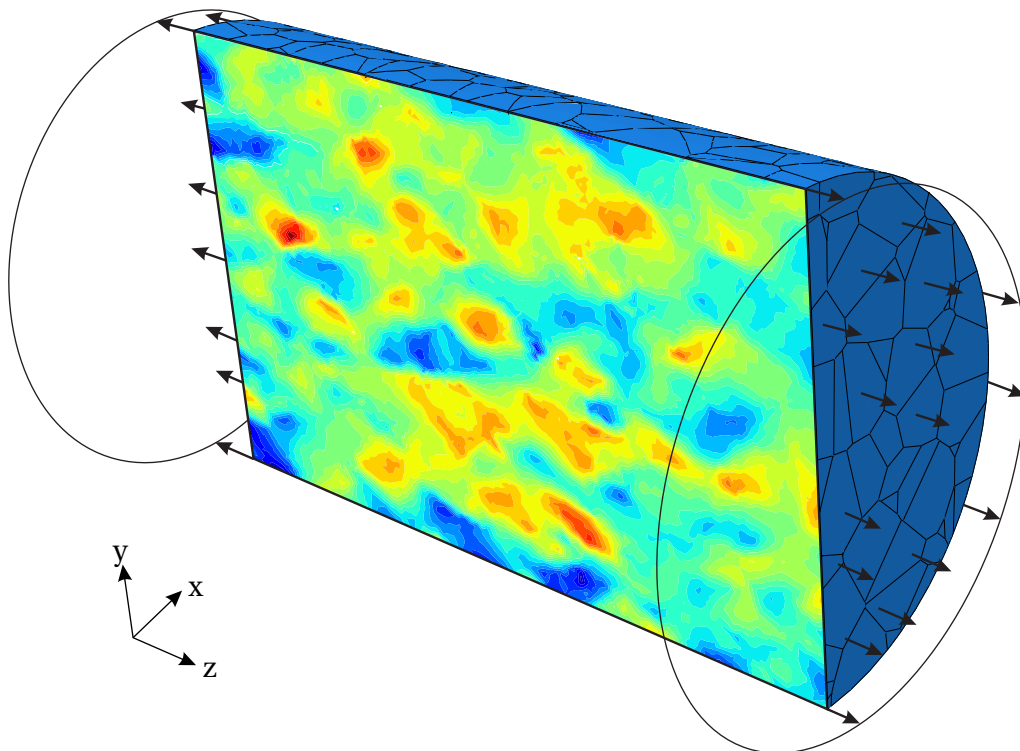


Figure 4.1 Normal stresses σ_{zz} in the cross-section of cylindrical polycrystal under tension

heterogeneous structures like polycrystal, the important information about the stress state is included in the whole domain, as shown on the example of a cylindrical bar under tension in Fig. 4.1, where distribution of the normal stresses σ_{xx} in a cross-section is presented. Due to randomized crystalline lattice orientations and the anisotropic material constitutive model inside grains, one can observe regions with high and low stresses and strains. In average, it characterizes a macroscopic response of the polycrystal.

However, the sophisticated macroscopic behavior, caused by the heterogeneity of polycrystalline microstructure, can be expected in certain regions of a polycrystal such as the free surface, holes, notches, etc. In order to investigate a macroscopic response in such regions and its difference with the bulk area, special numerical techniques of averaging and interpolation are developed and implemented, as discussed in this chapter.

As a common approach, the CAD/CAE program Abaqus possesses a Visualization module to extract field values at specified locations and time frames. However, the full automatization of the postprocessing step is required for statistical analysis. It can be done with the help of the Abaqus scripting interface in the same way as during the construction of geometrical and finite element models. Moreover, the accessing to solution's database can be performed with programming language C++ instead of the less efficient Python language.

A certain part of the postprocessing code uses embedded Abaqus functions, such as the transformation of coordinate system, the reading of field values, etc. Besides, sophisticated numerical techniques were introduced.

4.1 Volumetric averaging

First of all, the averaged values of required fields should be computed to illustrate the relationship between applied loads and the achieved response. The widely-known volumetric averaging procedure allows us to calculate averaged components of the field over the entire polycrystal or in certain regions, like the surface and bulk. However, since a random local coordinate system is involved to introduce a crystal lattice orientation inside grains, the tensorial elemental values such as stresses and strains are stored within that coordinate system. Therefore, the rotation of tensors into the global CS should be performed at first. For this purpose, one may access the Abaqus ASI function "getTransformedField", which provides rotation of a data field into

required CS. Elemental values at the global CS can then be averaged by using following equation:

$$\bar{F}(t) = \frac{\sum f_i(t)v_i}{V} \quad (4.1)$$

where f_i and v_i are the field value and the volume taken from an i -element, V is the total volume, and sum is taken over all elements.

This approach can be extended by specifying the averaging domain. For example, the redistribution of high- and low-stress phases can be averaged separately, assuming mean stress as a threshold between phases. Likewise, the distribution of stresses in the radial direction of a cylindrical polycrystal can be analyzed by volumetric averaging within the radial layers.

However, the application of volumetric averaging is suggested for the analysis of regions with a statistically uniform deformation gradient. Otherwise, important local effects may be lost during averaging. For instance, the influence of discrete polycrystalline microstructure in models with notches or holes can not be clearly analyzed by using the volumetric averaging because of the non-uniform deformation gradient, especially in the concentration area. For this reason, the algorithm of point-wise averaging was developed, as presented in next section.

4.2 Point-wise averaging

Unlike volumetric averaging, the proposed algorithm averages the solutions over several samples point-wisely, as shown on Fig. 4.2. Each sample is generated, considering the identical shape and simulated under the same loading and boundary conditions. Due to a random polycrystalline microstructure, the unique distribution of stresses and strains is observed in each sample, as demonstrated in the cross-section in the figure. By collecting field values from those N fields at the same location, one can calculate the arithmetic mean with equation (4.2). To calculate the averaged distribution \hat{F} within an entire cross-section the procedure should be repeated at each point of the averaging grid. The proposed technique allows us to identify specific tendencies and features which are invisible in the single specimen. Thus, the averaged distributions of stresses in cylindrical polycrystals clearly demonstrate the appearance of the surface layer effect, which is discussed later in Chapter 5.

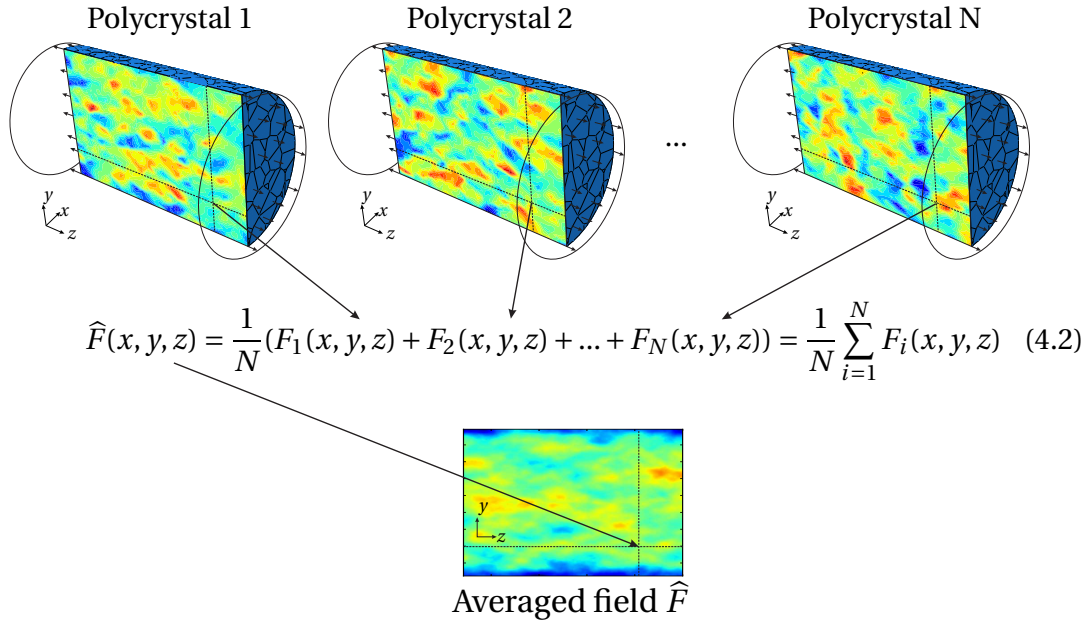


Figure 4.2 Scheme of point-wise averaging over N samples of polycrystal

Nevertheless, the point-wise averaging algorithm requires a single grid of points for gathering and averaging values from different specimens. Due to the randomness of a polycrystalline microstructure, the cross-section of finite element meshes in these models is incompatible. For the reason that the simulation results are stored at nodes and Gauss points, the proposed techniques can not be applied directly on the mesh. Therefore, the field values in each specimens should be projected onto a generated regular grid of points at first. It can be done by using the developed three-dimensional interpolation algorithm presented further.

4.3 Interpolation using shape functions

Since the finite element method is used to decompose a complex geometrical model into a mesh of basic elements, it is convenient to implement interpolation algorithm using the shape functions of FE. Basically, they are involved in FEM to interpolate values at integration points from nodal field data, as explained in textbooks [47, 111], among many others. The interpolation function (4.3) consists of Lagrangian polynomials N_i , where each polynomial refers to i -node of the element. Also known as shape functions, they are described for each type of the finite element considering non-dimensional natural coordinates g, h , and r , which are defined in the

range of $[-1..1]$ or $[0..1]$. The boundary values of local coordinates correspond to the nodes of an element.

$$f(g, h, r) = \sum_{i=1}^n N_i(g, h, r) f_i \quad (4.3)$$

where n is a total number of nodes in element, f_i is a value of interpolating field at i -node.

Using interpolation function (4.3), the global coordinates of an arbitrary point described in the natural coordinates can be calculated as follows:

$$\begin{aligned} x(g, h, r) &= \sum_{i=1}^n N_i(g, h, r) x_i \\ y(g, h, r) &= \sum_{i=1}^n N_i(g, h, r) y_i \\ z(g, h, r) &= \sum_{i=1}^n N_i(g, h, r) z_i \end{aligned} \quad (4.4)$$

where x_i , y_i , and z_i are the global coordinates of the i th node.

In the same way, components of stresses, strains, displacements, etc. can be interpolated as well:

$$\begin{aligned} \sigma(g, h, r) &= \sum_{i=1}^n N_i(g, h, r) \sigma_i, \\ \varepsilon(g, h, r) &= \sum_{i=1}^n N_i(g, h, r) \varepsilon_i, \\ \mathbf{u}(g, h, r) &= \sum_{i=1}^n N_i(g, h, r) \mathbf{u}_i, \end{aligned} \quad (4.5)$$

where σ and ε are stress and strain tensors, respectively, while \mathbf{u} is vector of displacements.

As mentioned above, the general idea of the proposed algorithm is based on the interpolation of a required scalar field at each point of the projecting grid, which is illustrated exemplarily in Fig. 4.3. In this case, the global coordinates of these points should be recalculated within the local coordinate system of the corresponding finite element. The so-called mapping procedure can be performed once for the required cross-section of a specimen. Afterwards, the calculated local coordinates of the grid's points are used to interpolate the field values at an arbitrary time frame.

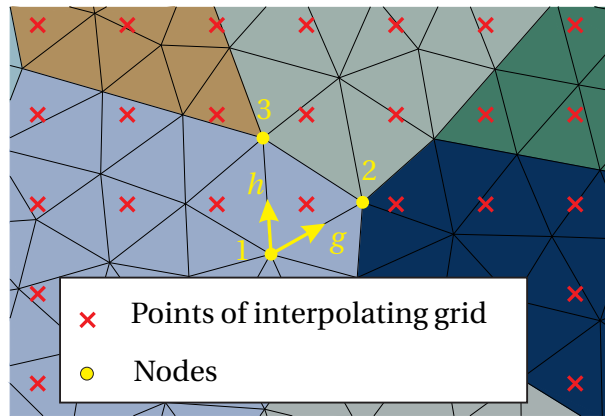


Figure 4.3 Illustration of the mapping procedure as projection of an interpolating grid of points onto arbitrary finite element mesh

Although the identification of the belonging finite element is a trivial task, the calculation of the local coordinates for an arbitrary point requires additional computational effort. Considering volumetric finite elements, the solution was found and implemented only for linear finite elements. Moreover, whereas the generalized solution is given for a tetrahedron, the mapping within a hexahedron and prism was described for a special case.

4.3.1 Linear tetrahedral finite element

The widely-known linear tetrahedral finite element consists of four nodes and four triangular facets, as presented in Fig. 4.4. It is commonly applied in structural analysis with FEM, due to the simplest geometry and the free meshing algorithm. The local coordinates g , h , and r are defined in a range of $[0..1]$ with the origin at node 1.

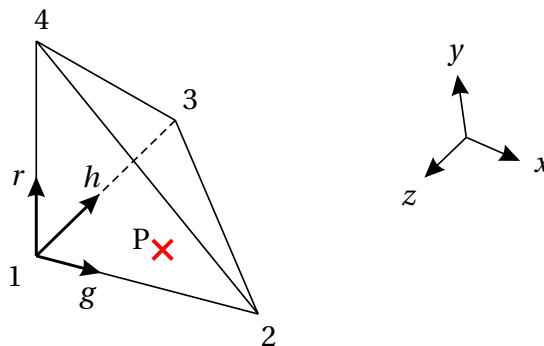


Figure 4.4 Arbitrary point P within linear tetrahedral finite element C3D4

The interpolation function is described in equation (4.6) with introduced shape functions.

$$f(g, h, r) = (1 - g - h - r)f_1 + gf_2 + hf_3 + rf_4 \quad (4.6)$$

The global coordinates of an arbitrary point $P(x_P, y_P, z_P)$ inside tetrahedra can be found by substituting the global nodal coordinates into the equation above in the same way as shown in the general case (4.4). Through the inverse transformation of these equations, the local coordinates (g, h, r) of point $P(x_P, y_P, z_P)$ follow from the system of equations:

$$\begin{bmatrix} x_2 - x_1 & x_3 - x_1 & x_4 - x_1 \\ y_2 - y_1 & y_3 - y_1 & y_4 - y_1 \\ z_2 - z_1 & z_3 - z_1 & z_4 - z_1 \end{bmatrix} \begin{Bmatrix} g \\ h \\ r \end{Bmatrix} = \begin{Bmatrix} x_P - x_1 \\ y_P - y_1 \\ z_P - z_1 \end{Bmatrix} \quad (4.7)$$

where x_i, y_i, z_i for $i = 1..4$ are nodal cartesian coordinates.

The obtained local coordinates can be used to interpolate stress, strain, and displacement components by equation (4.6). For the reason that solids of grains are represented by tetrahedra, the general results after the point-wise averaging are obtained with the given generalized solution of the mapping procedure. However, prism and hexahedral finite elements are considered as well.

4.3.2 Linear hexahedral finite element

A hexahedral finite element demonstrates higher accuracy and stability within FEA in comparison with a tetrahedron, but requires an advanced meshing technique. For example, such elements can be generated by using extrusion, sweep or revolution algorithms, and a source quadrilateral mesh. Neither of these techniques is applicable for meshing the Voronoi cells because of an

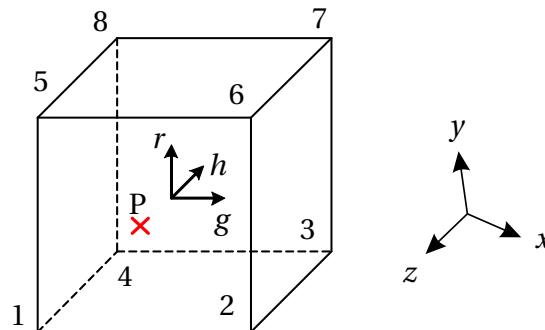


Figure 4.5 Arbitrary point P within linear hexahedral finite element C3D8

undefined elongation direction and the complicated meshing of polygonal faces. However, the boundary layer and the extruded Voronoi diagram are well suitable for the sweep or extrusion algorithm, due to the prism topology. Furthermore, both techniques facilitate the mapping of local coordinates for an arbitrary point within FE. Unlike the generalized case, two parallel facets in the element are assumed. Therefore, one of three local coordinates r can be identified explicitly, since it coincides with the extrusion direction. To calculate the remaining natural coordinates g and h , the inverse transformation of the interpolation function (4.8) is performed by substituting nodal cartesian coordinates, as shown in Appendix B.

$$\begin{aligned}
 u(g, h, r) = & \frac{1}{8}(1-g)(1-h)(1-r)u_1 + \frac{1}{8}(1+g)(1-h)(1-r)u_2 \\
 & + \frac{1}{8}(1+g)(1+h)(1-r)u_3 + \frac{1}{8}(1-g)(1+h)(1-r)u_4 \\
 & + \frac{1}{8}(1-g)(1-h)(1+r)u_5 + \frac{1}{8}(1+g)(1-h)(1+r)u_6 \\
 & + \frac{1}{8}(1+g)(1+h)(1+r)u_7 + \frac{1}{8}(1-g)(1+h)(1+r)u_8
 \end{aligned} \tag{4.8}$$

4.3.3 Linear prism finite element

The prism finite element is generated in the same way as the hexahedron, but taking into account the triangle base facets, as shown in Fig. 4.6. Hence, the planar triangular mesh can be used as a source of the extrusion or sweep algorithm. Since solids of grains are represented by tetrahedra, the grain boundary layer is generated with prism finite elements, as was discussed in Section 2.4.1. Moreover, the same assumption on parallel facets can

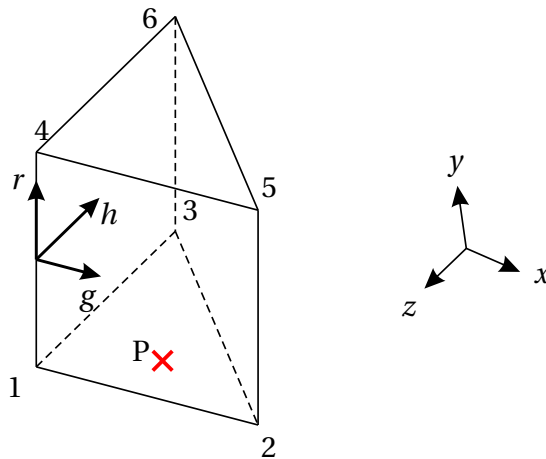


Figure 4.6 Arbitrary point P within linear prism finite element C3D6

be considered in order to simplify the calculation of natural coordinates, which was introduced for the hexahedron. Therefore, the third natural coordinate r coincides with the normals of the top and bottom facets. The remaining coordinates g and h can be obtained from the transformation of the generalized interpolation function (4.9), as explained more detailed in Appendix C.

$$\begin{aligned}
 u(g, h, r) = & \frac{1}{2}(1 - g - h)(1 - r)u_1 + \frac{1}{2}g(1 - r)u_2 + \frac{1}{2}h(1 - r)u_3 \\
 & + \frac{1}{2}(1 - g - h)(1 + r)u_4 + \frac{1}{2}g(1 + r)u_5 + \frac{1}{2}h(1 + r)u_6
 \end{aligned} \tag{4.9}$$

Simulation

Using the developed framework, polycrystalline samples with different shape were generated and analyzed under various loads. For the reason that a representative volume element is not applicable for the simulation of the discussed micro-parts, geometrical and finite element models are generated, considering the large number of grains and free boundary conditions on surfaces. Hence, the analysis of the deformation and stress states in the entire polycrystalline specimens is performed and presented in this chapter.

Since the anisotropic constitutive material model and a random crystal lattice orientation are described in each grain, the distributions of stresses and strains show high heterogeneity. However, the tendency of these fields can be investigated in a large number of samples by using the developed point-wise averaging technique which was explained in previous chapter. In the case where the obtained averaged distribution demonstrates a correlation with the solution of the RVE, one can consider the applicability of the scale-separation method. Besides, these effects can be assumed to be negligible if their contribution is small enough. The most important observation made in this work was the detection of the so-called surface layer effect in polycrystalline samples with free surfaces under tensile/compression loading conditions. This effect is thoroughly analyzed assuming zero-thickness grain boundaries and perfectly bonded grains, which allows to consider plenty of samples with a large number of grains. After the identification of the general properties, the simulation of the intergranular fracture in a single cylindrical specimen was performed as well, in order to investigate the behavior of the surface layer effect under damage propagation.

5.1 Surface layer effect

The averaged distributions of normal and equivalent stresses clearly show lower stresses in the surface layer in comparison with the bulk region. This effect can be explained by the fact that there are less constrained grains on the surface of the specimen. At least one side of those grains is free of constraints. It is widely-known that a clear understanding of the material behavior in the surface and bulk regions is a key point in the precise prediction of the life time and critical working conditions. An experimental confirmation of the layer's existence can be found in several papers and reports [8, 54]. The general observations there show that the thickness of the layer is approximately equal to the size of 1-3 grains. Therefore, an experimental investigation requires complex precise equipment, including a testing machine and micrography devices. Besides, the general properties of the layer can be analyzed numerically, assuming the simplest material model and the shape of the sample.

In the present work, three different shapes of samples are considered: a thin rectangular plate, a cylindrical bar and a notched cylindrical bar. The first two models are investigated with the viscoplastic grain material model, while the notched cylinder is analyzed under purely elastic tension. Unlike the smooth cylinder and rectangular plate, the notched cylinder demonstrates non-uniform deformation gradient under tension. In this case, the comparison with an inelastic homogeneous model is not accurate because of unknown macroscopic inelastic material model. Even though such a model can be described through the homogenization of an RVE, one may mistakenly recognize the parameter's identification error as a useful feature of the polycrystalline microstructure. Instead, the comparison of the elastic solution between the polycrystal and the homogeneous model allows us to perform a clear qualitative analysis. Considering a smooth homogeneous cylinder, stresses and strains are uniformly distributed. Therefore, the area of the RVE's applicability can be identified in the averaged distribution of stresses and strains taken from polycrystalline model with a large number of grains and the realistic boundary conditions.

5.1.1 Rectangular plate under cyclic load

Polycrystalline samples of a rectangular plate with 1000 grains are generated by the extrusion of a planar Voronoi diagram for a single layer of finite elements. Although such a polycrystal can not be investigated in real

experiments, the numerical simulation is more efficient. Thus, the larger number of grains is generated within the cross-section of a rectangular plate rather than in a cylindrical bar, considering the similar number of elements.

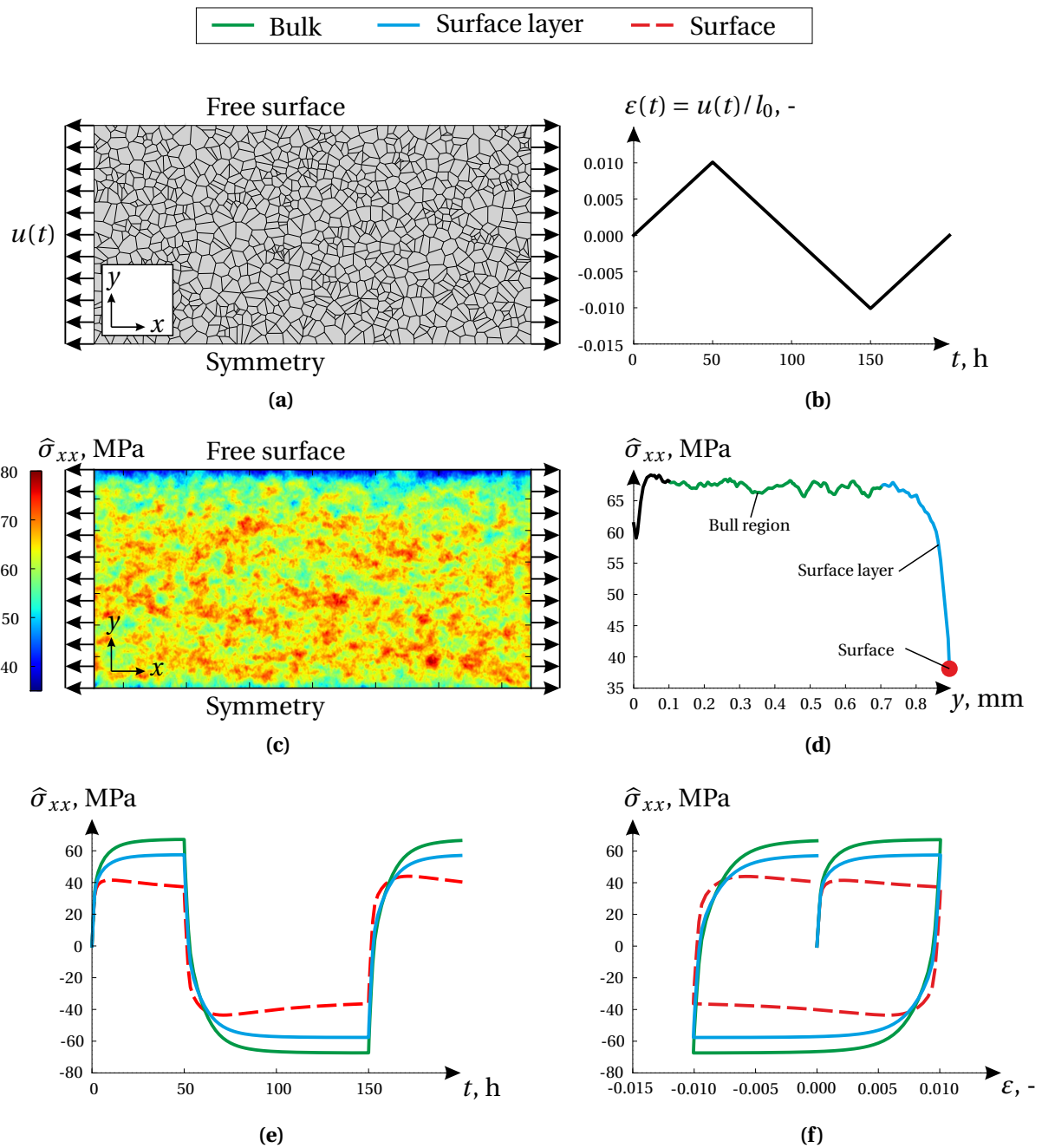


Figure 5.1 Rectangular plate under cyclic load: (a) example of polycrystal; (b) loading amplitude; (c) averaged distribution of stresses at 50 h; (d) stresses vs. vertical coordinate at 50 h; (e) averaged stresses in bulk and surface regions; (f) hysteresis loops

The geometrical model of one sample from a total of 400 grains is shown in Fig. 5.1a, where symmetric and free boundary conditions were applied on the bottom/back and top/front sides, respectively. Each sample is deformed by cyclic displacement-controlled load $u(t)$ (amplitude in Fig. 5.1b), applied to the left- and right-hand sides of the model.

After a successful simulation of the samples with anisotropic viscoplastic material model, the averaged distribution of stresses in the loading direction was computed using the point-wise averaging technique at each time increment. Fig. 5.1c illustrates such a distribution at the time point of 50 h, when maximum strains are applied. In the figure almost uniform stresses are observed in the bulk region, whereas they are decreased in the surface layer. Therefore, the applicability of the RVE method can be confirmed only in the bulk region, while the modeling of the surface layer requires its description in the macroscopic material model. More evidently, the effect can be represented in Fig. 5.1d, where stresses along the vertical coordinate y of the model are shown. Taking into account an average grain size of $40\ \mu\text{m}$, the thickness of the surface layer effect is approximately equals 2-3 grains, which correlates with the experimental observation [54]. Moreover, the difference between stresses in the surface layer and the bulk region is significant and may change during the loading cycle. For this reason, three domains of volumetric averaging are introduced: the bulk, the surface layer, and the surface, as shown in Fig. 5.1e by green, blue, and red color, respectively. The macroscopic behavior in these regions is illustrated as the relation between stresses and time in Fig 5.1e, and stresses and strains in Fig. 5.1f.

Beside the amplitude of stresses, the thickness of the layer is changed as well. It can be shown by 3D plot 5.2a, where the horizontal axis represents time, the vertical axis represents the vertical coordinate of the model, and color connotes the amplitude of the averaged stresses at corresponding position and time point. Therefore, a slice of the 3D plot at time point of 50 h is the same as the one given in the Fig. 5.1d, considering another projection. By normalizing the stress values by following equation, the comparison with bulk region can be displayed more clearly.

$$\Delta\hat{\sigma}_{xx}^{\text{norm}}(y) = \frac{|\hat{\sigma}_{xx}(y) - \bar{\sigma}_{xx}^{\text{bulk}}|}{\max_y(|\hat{\sigma}_{xx}(y) - \bar{\sigma}_{xx}^{\text{bulk}}|)} \quad (5.1)$$

where

$$\bar{\sigma}_{xx}^{\text{bulk}} = \frac{1}{0.6} \int_{0.1}^{0.7} \hat{\sigma}_{xx}(y) dy \quad (5.2)$$

Thus, Fig. 5.2b demonstrates that the thickness of the surface layer may change on the reversing of load, but remains steady-state in the case of a constant loading rate.

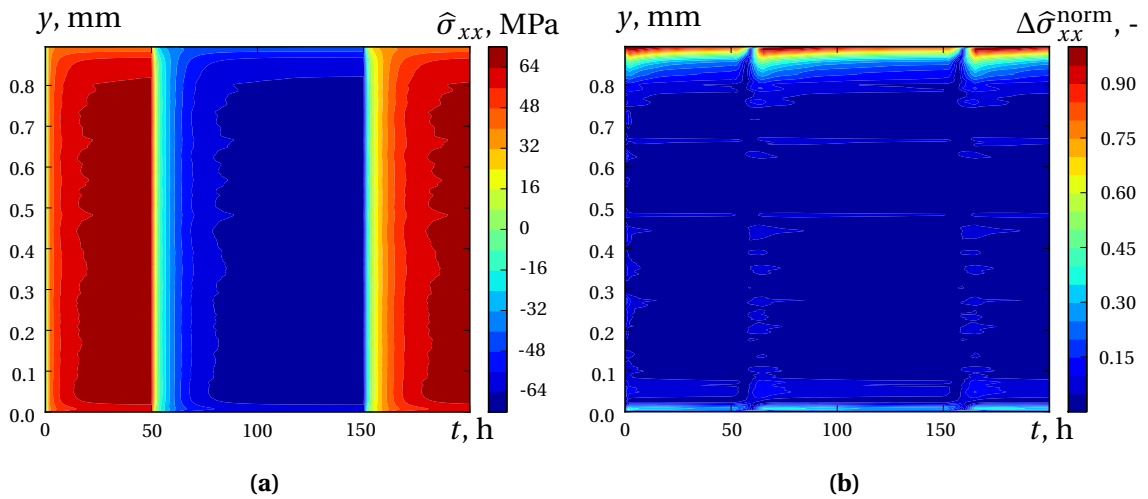


Figure 5.2 Average stresses $\hat{\sigma}_{xx}$ with respect to vertical coordinate y and time: (a) non-normalized, (b) normalized

The proposed model of the rectangular plate was used as a simple simulation framework. However, general results are given for the more realistic model of a cylindrical bar.

5.1.2 Cylindrical bar in cyclic viscoplasticity

A polycrystalline cylindrical bar is a more representative model than a thin rectangular plate, due to its similarity with real micro-parts such as pins, wires, etc. Moreover, artificial boundary conditions, such as symmetry, are not involved in the simulation, since the entire specimen is considered. Hence, free boundary conditions are described on the surface of the cylinder. The construction of finite element models for polycrystals with a complex shape and large number of grains is discussed in Chapter 2. Fig. 5.3a shows a single example out of 400 realizations of a smooth cylindrical bar with approximately 1000 grains. All samples have identical dimensions with a diameter and length of 0.4 mm, but a randomized microstructure. Considering a similar displacement-controlled loading amplitude on the sides of the cylindrical bar (Fig. 5.3b), as it was done in the previous model, 400 polycrystals were investigated in cyclic loading conditions.

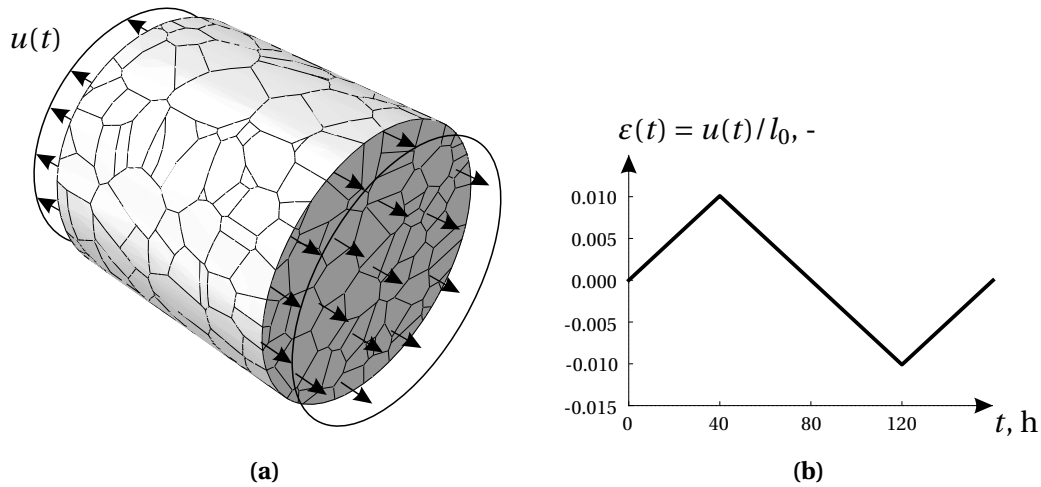


Figure 5.3 Cylindrical bar: (a) example of polycrystal; (b) loading amplitude

Taking into account the random material orientations and anisotropic viscoplastic behavior inside the grains, heterogeneous stress and deformation states are obtained by using the finite element method. Due to the implemented implicit time integration scheme of the user defined material subroutine UMAT, the stable time increment was achieved. It allows us to simplify the calculation of averaged distributions of a required field with the developed point-wise averaging algorithm because of an identical discrete time scale in all solutions. The averaged normal stresses $\hat{\sigma}_{zz}$ at time point of 40 h are shown in figures 5.4 within three different cross-sections of the cylindrical bar. The obtained averaged distributions clearly demonstrate the presence of the surface layer effect in the cylindrical model, too. Besides, the thickness of the layer is approximately equal to the size of 1.5 grain, or $60\mu\text{m}$, which is less than in the previous example of a thin rectangular plate. It can be explained by the more realistic boundary conditions and shape of grains in the cylindrical bar, whereas in the rectangular plate symmetry was considered on the back side of the extruded grains and a free surface on the front. Anyway, the well-known solution of a homogeneous cylinder within the classical continuum theory states uniform normal stresses and strains under tension. Hence, the applicability of the scale-separation method with a RVE should be reconsidered.

Since the thickness of the layer is identified, one can compare the macroscopic response in bulk and surface regions over a cycle by introducing two corresponding volumetric averaging domains. Fig. 5.4d displays averaged bulk stresses by a green line, whereas the blue line represents normal stresses in the surface layer.

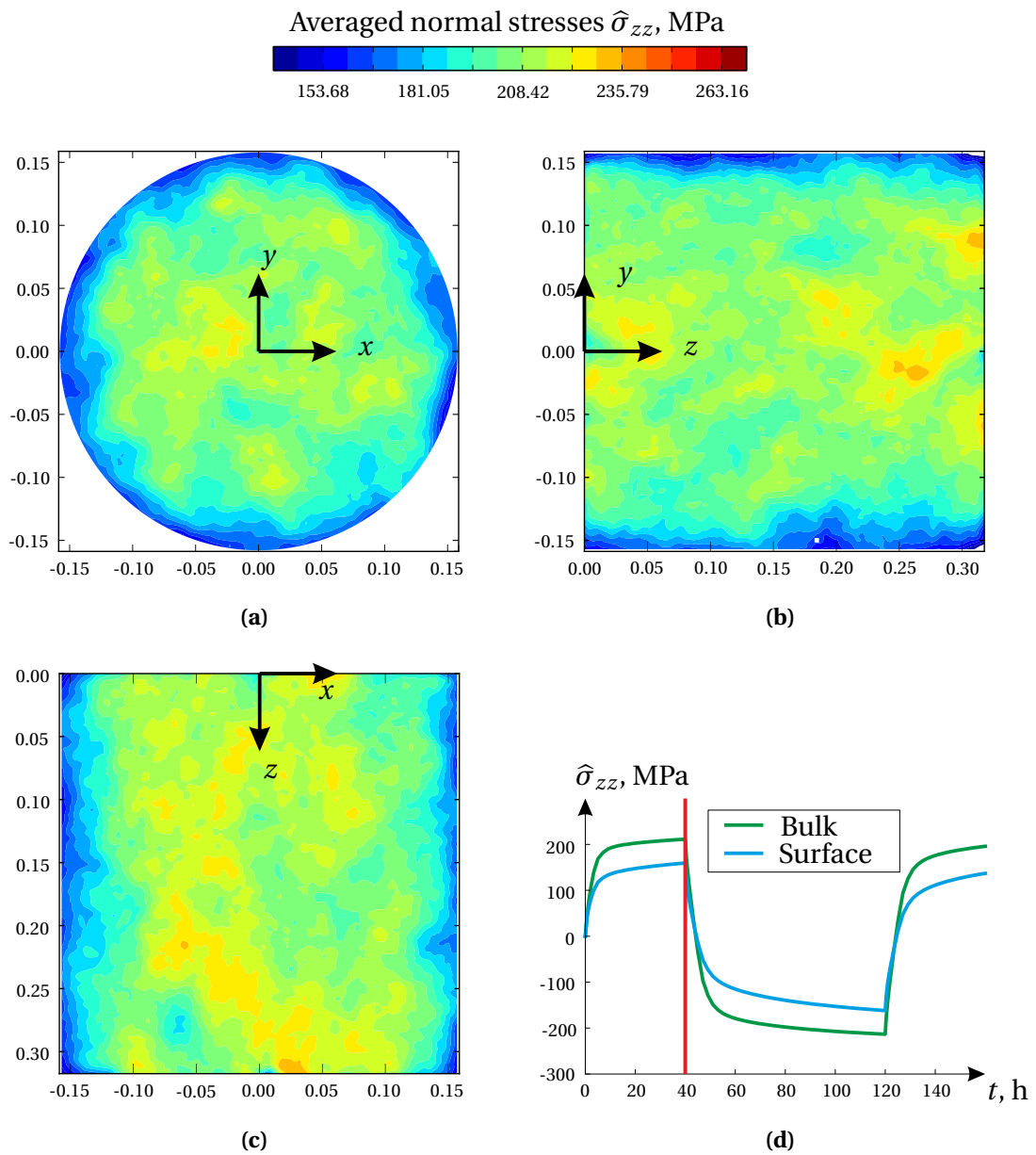


Figure 5.4 Averaged distributions of stresses in cylindrical model:
 (a) cross-section XY; (b) Cross-section YZ; (c) cross-section XZ; (d)
 averaged stresses in bulk and surface layer with respect to time

Despite the simplest anisotropic viscoplastic material behavior and perfectly bonded grains, the a nonlinear macroscopic response is achieved. For example, the Bauschinger effect and hardening are clearly observable on both curves. The smaller amplitude of stresses in the surface layer can

be noticed on loading steps as well as on unloading. Moreover, the plots demonstrate the slight decrease of the difference between stresses in the bulk region and in the surface layer at steady-state regimes. Therefore, a sophisticated behavior of the effect can be expected under various loading conditions. For this reason, displacement-controlled tensile tests are performed with the same set of cylindrical polycrystals, but a different loading rate, as discussed further.

5.1.3 Cylindrical bar under tension. Loading rate dependence

In this test, the dependence of the surface layer effect on the loading rate was investigated in 400 polycrystalline cylindrical bars with approximately 1000 grains. An example of the geometrical model is illustrated on the surface of the model in Fig. 5.5, where free boundary conditions are considered on the surface of the polycrystals, and displacement-controlled load is applied on the sides. The polycrystals were deformed by two different ramp amplitudes with loading rates of 0.1 %/h and 0.05 %/h, which is illustrated in Fig. 5.6a.

Taking into account the viscoplastic material behavior and random

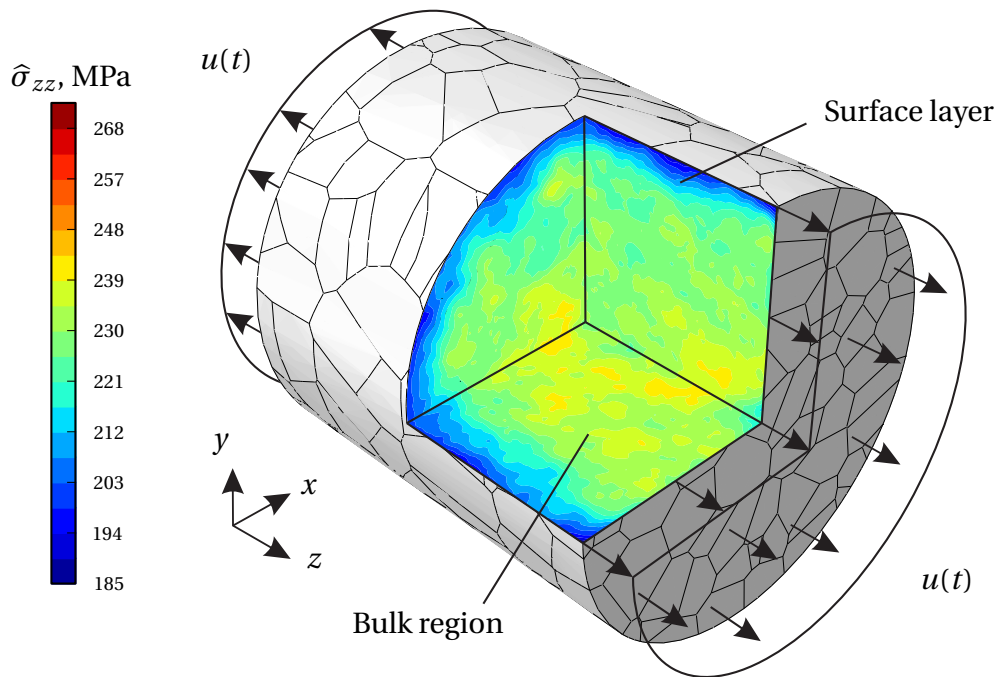


Figure 5.5 Averaged distribution of normal stresses $\hat{\sigma}_{zz}$ in three cross-sections for loading rate 0.1 %/h at the end of simulation. Example of microstructure on the surface

material orientations inside the grains, the simulation shows heterogeneous distributions of stresses, elastic and inelastic strains. Moreover, the loading rate dependent accumulation of inelastic strains causes the redistributions of stresses and total strains. Averaged stresses in normal directions are calculated using the mentioned point-wise averaging algorithm for two loading rates separately. For example, Fig. 5.5 demonstrates the averaged distribution of stresses within cross-sections of the cylinder for the analysis with a loading rate of 0.1 %/h at time point of 20 hours. The surface layer can be clearly observed in the figure.

The development of stresses in bulk and surface regions can be illustrated by introducing two corresponding domains for volumetric averaging. Thus, Fig. 5.6b demonstrates the relationship between normal stresses $\hat{\sigma}_{zz}$ and applied strains ε_{zz} , whereby bulk stresses are represented by solid lines and stresses in surface layer by dashed lines. Blue and red colors are used to distinguish the results of the analysis with a 0.1 %/h and a 0.05 %/h loading rate, respectively. Plots demonstrate that stresses in the surface layer are almost 20 % smaller than in the bulk region.

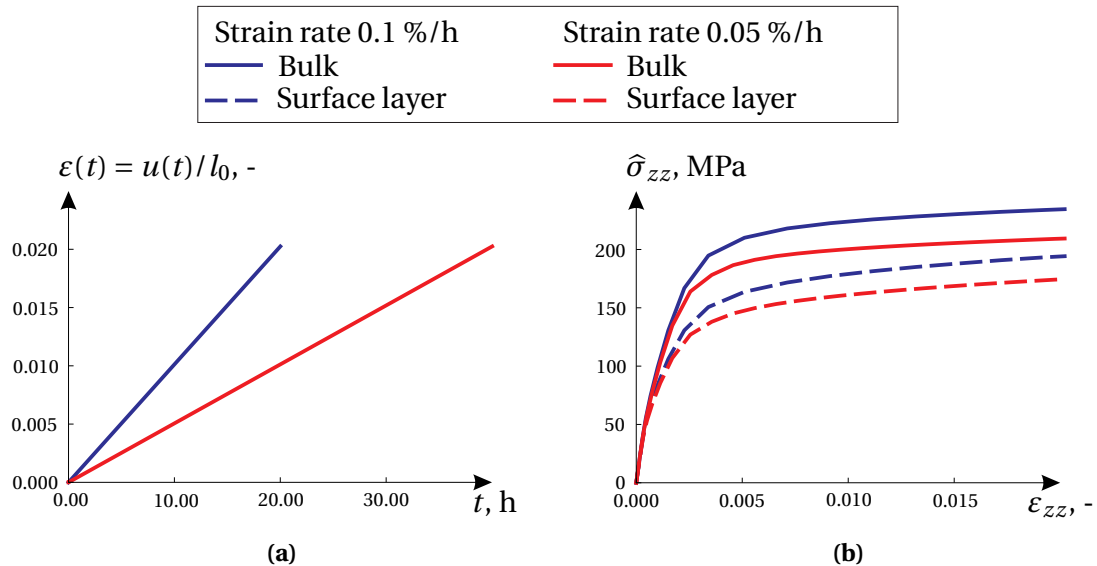


Figure 5.6 Averaged stresses in cylindrical polycrystals under different strain rates: (a) total strains; (b) averaged stresses

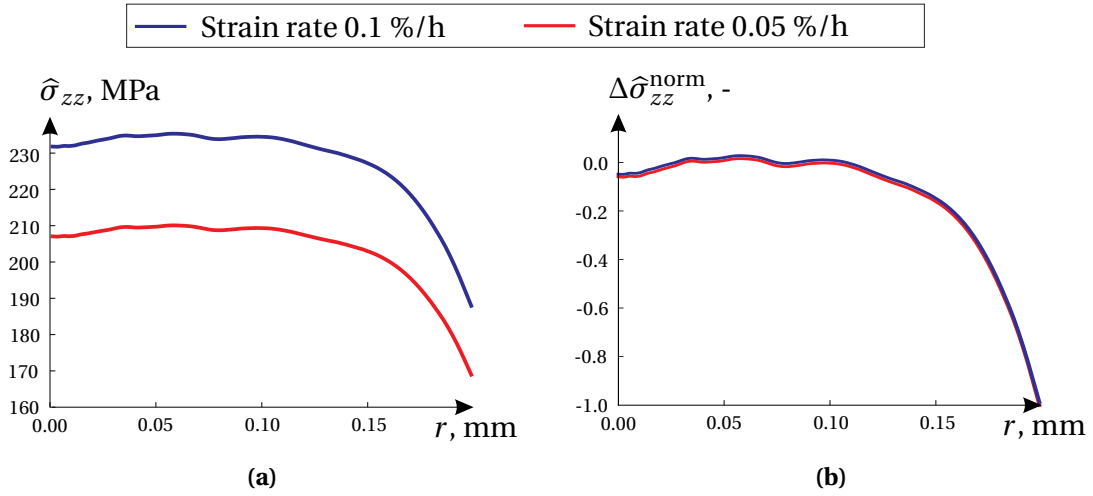


Figure 5.7 Average normal stresses $\hat{\sigma}_{zz}$ along the axis y : (a) non-normalized; (b) normalized

Besides, the general properties of the surface layer effect can be analyzed through the representation of normal stresses $\hat{\sigma}_{zz}$ with respect to the radial coordinate of the cylindrical bar. These plots are illustrated in Fig. 5.7a at the end time point of the simulations which corresponds to maximum applied strains of 2%. The bulk stresses in the given results are approximately equal 232 MPa and 209 MPa for 0.1 %/h and 0.05 %/h loading rates, respectively. An amplitude of the surface layer effect can be estimated as the difference between stresses in the bulk region and on the surface. Thus, for a higher strain rate it equals 45 MPa, while for a lower one it equals 40 MPa. However, the relative amplitude is approximately 19% in both cases. It can be more evidently demonstrated in Fig. 5.7b, where the difference of stresses normalized by bulk values is calculated with the similar equation (5.1). Furthermore, the equal thickness of the layer of $\sim 60 \mu\text{m}$ can be concluded for different loading rates.

Summarizing the obtained results, the independence of the surface layer effect's thickness and the normalized amplitude is stated for the described viscoplastic material model of grains. This conclusion can be used to facilitate further analysis of cylindrical bar under various loading conditions. For example, the single sample, rather than 400 samples, of cylindrical polycrystal is considered in the following sections. Taking into account the observed thickness of the layer, the sub-domain-based volumetric averaging algorithm can be used rather than point-wise averaging technique.

5.1.4 Cylindrical bar under tension. Relaxation test

It is widely-known that the microscopic redistribution of stresses and strains in polycrystals characterizes a non-linear material response. The mentioned results of tensile tests on 400 polycrystalline cylindrical samples clearly demonstrate the presence of the surface layer effect with a thickness of about 1-2 grains. Under ramp and cyclic loading conditions, the thickness of the layer is not changed significantly. Nevertheless, the behavior of the discovered effect should be investigated under relaxation loading conditions too.

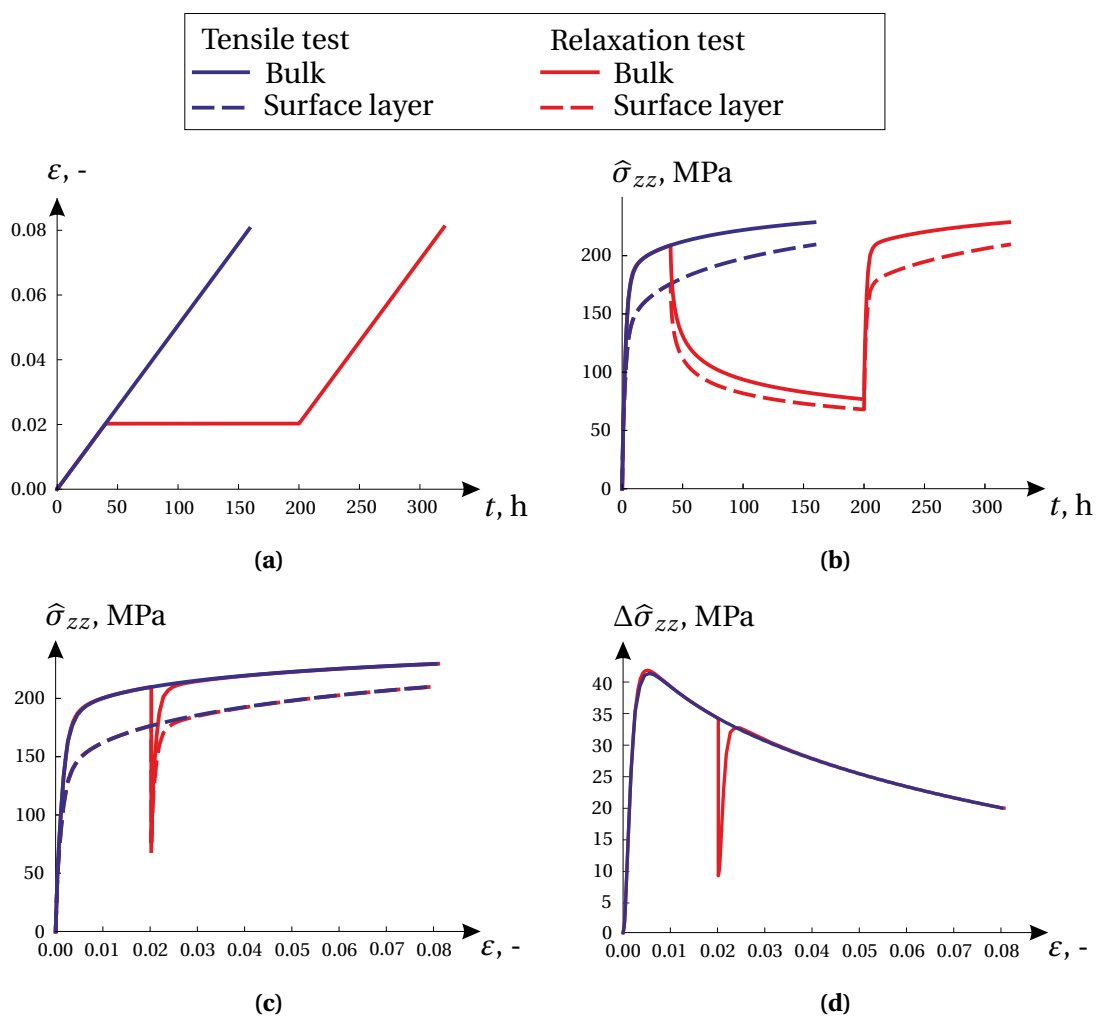


Figure 5.8 Stress response of a cylindrical polycrystalline specimen under tension and relaxation: (a) total strains; (b) averaged stresses; (c) stress-strain diagram; (c) difference between stresses in surface and bulk regions

Since the independence of the layer's thickness in a smooth cylinder is assumed, one can simulate a single sample of a polycrystal introducing bulk and surface regions of volumetric averaging. Therefore, computational and postprocessing times are reduced even though larger number of grains or a longer simulation time can be considered.

In the presented analysis, the cylindrical polycrystal (Fig. 5.3a) with 1000 grains was deformed in axial displacement-controlled tests with two different loading amplitudes, which are shown in the Fig. 5.8a. In the relaxation test, the sample is deformed by up to 2% in 40 hours with a constant strain rate. Afterwards, within 160 hours, the applied displacements on the sides of the cylinder are maintained, which implies the relaxation procedure. Eventually, the tension of the sample is continued to up to 8% of strains with same the initial strain rate in order to investigate the influence of the stress relaxation on the mechanical properties of a microstructure. Moreover, the identical sample was deformed with the same loading rate from 0 to 8% of strains. The corresponding plots of the loading amplitudes and the averaged macroscopic response are demonstrated by red and blue lines in the figures.

Fig. 5.8b illustrates averaged normal stresses $\hat{\sigma}_{zz}$ over time in the bulk region by solid lines and in the surface layer by dashed lines. Noticeably, the evolution of stresses in these regions is similar in both tests. It is clearly noticeable in Fig. 5.8c, where stresses are shown in respect to applied strains.

5.1.5 Cylindrical bar under multicyclic deformation

The final results of the investigation of the surface layer effect in a smooth cylinder are obtained in a multicyclic test of a single polycrystalline specimen, similar to Fig. 5.3a. Besides free boundary conditions on the surface of the sample, the displacement-controlled load was applied on the sides, regarding the amplitude in Fig. 5.9a.

Thus, four cycles with a period of 160 hours and a mean zero value were simulated considering maximum applied strains of 2%. Fig. 5.9b and 5.9c represent averaged stresses in the bulk region by a green line and in the surface layer by a blue line with respect to time and total strains, respectively. On hysteresis loops, an almost exact match between cycles can be observed in these regions. Furthermore, the difference between stresses in the bulk region and surface layer does not change significantly between the cycles, as it is shown in Fig. 5.9d. The similar amplitude over all cycles allows us to conclude the independence of the surface layer effect under multicyclic loading conditions, despite a complex non-linear material behavior.

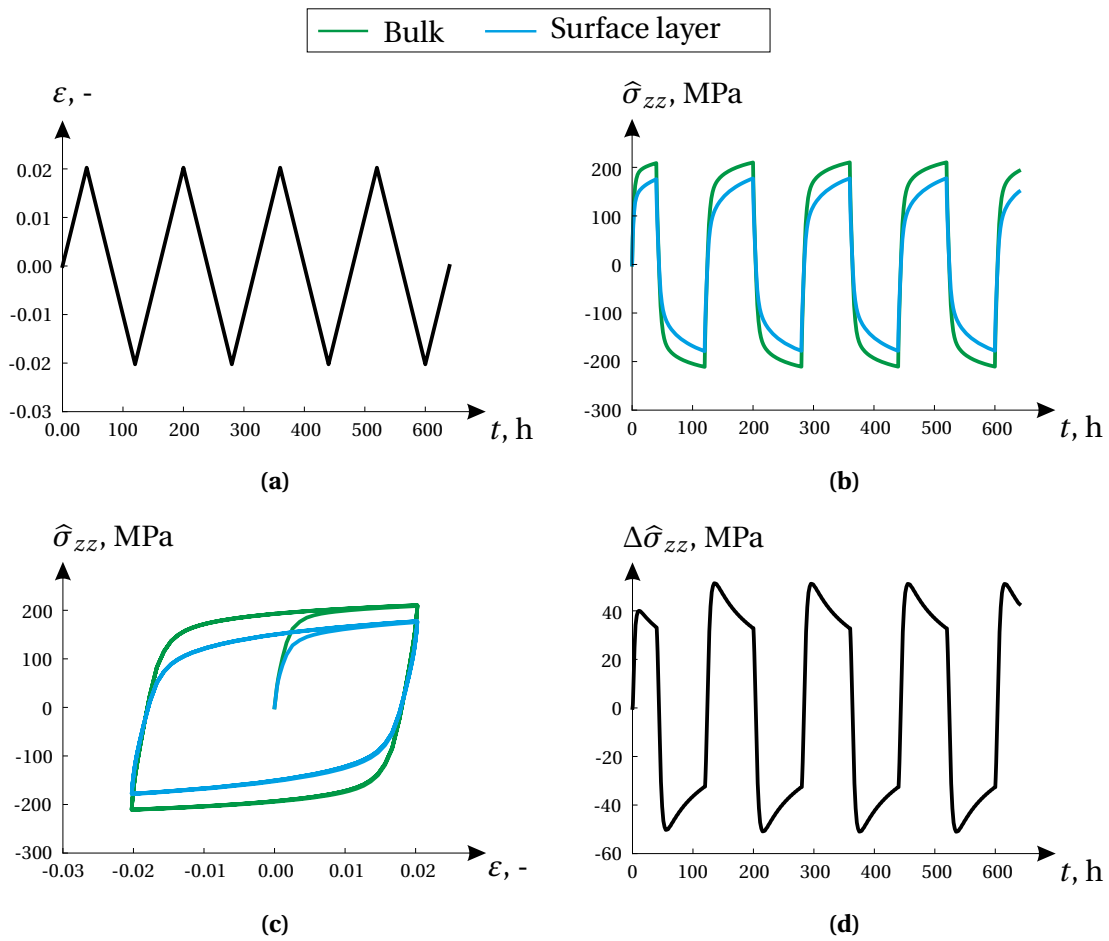


Figure 5.9 Averaged stresses in cylindrical polycrystal during four cycles of deformation: (a) total strains; (b) averaged stresses; (c) stress-strain diagram; (d) difference between stresses in surface and bulk regions

5.1.6 Influence of grain material's anisotropy

Besides the shape of polycrystal, loading and boundary conditions, the influence of the grain material properties on the surface layer effect is investigated as well. As mentioned earlier, the appearance of the surface layer effect can be explained by the fact that the grains on a surface are less constrained. Therefore, a rate of the grain material's anisotropy may affect the basic properties of the layer such as thickness and amplitude. The grain material model is formulated by the anisotropic elasticity and anisotropic viscoplasticity, considering the randomized crystal lattice orientation, as explained in Section 3.1. For this reason, the two different tensile tests were

performed in this analysis: the viscoplastic test and purely elastic test. In both cases the set of 400 randomized realizations of the cylindrical polycrystal with approximately 1000 grains are generated and simulated under tension. The example of a polycrystal is shown above in Fig. 5.3a.

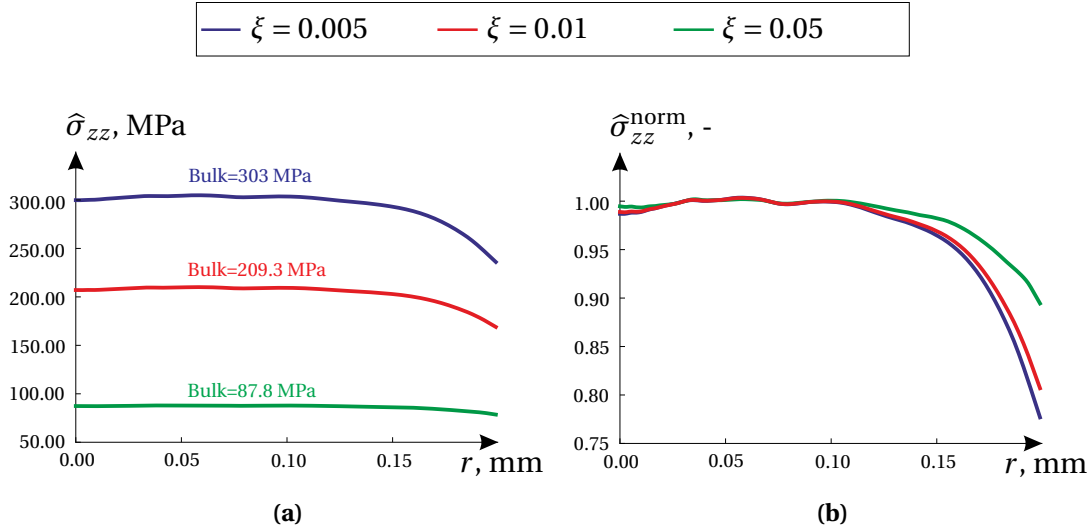


Figure 5.10 Averaged stresses vs. radial coordinate in a cylindrical specimen with the viscoplastic grain material model: (a) non-normalized; (b) normalized

The influence of the grain anisotropy on the surface layer effect can be investigated through a comparison of the average stresses in models with different material properties. Thus, in the viscoplastic test, three values of the coefficient of inelastic anisotropy $\xi = \{0.005, 0.01, 0.05\}$ are used. Other elastic and inelastic parameters are remained the same. Despite the identical displacement-controlled loading and the boundary conditions, the different response can be observed in 400 polycrystals. The results of simulations were averaged using a developed point-wise averaging algorithm within cross-sections of the finite element models. Since, the configuration of the layer in a cylindrical specimen was already investigated in previous tests, the average distributions of stresses can be furthermore averaged along the radial direction. By this way, the relationship between the average normal stresses $\hat{\sigma}_{zz}$ and the radial coordinate r is obtained and illustrated in Fig. 5.10a for three different values of the coefficient of anisotropy ξ . In the figure, a red color corresponds to the default value of $\xi = 0.01$, while blue and green colors refer to larger and smaller anisotropy, respectively. In order to compare these curves qualitatively, Fig. 5.10b shows normalized stresses

by corresponding bulk values. The thickness of the layer seems similar in all three cases, while the dependence of the surface layer's amplitude on the coefficient of anisotropy can be stated. In the second test, the polycrystals were investigated under elastic tension with deactivated inelastic material parameters. The elastic behavior of crystallites is characterized by three constants $\lambda_1 = 410$ GPa, $\lambda_2 = 47$ GPa, and $\lambda_3 = 150$ GPa, as described in Section 3.1. In the similar way, two constants λ_1 and λ_3 were fixed, while the three values for the third constant $\lambda_2 = \{20, 47, 100\}$ GPa are used in this analysis in order to introduce different level of anisotropy. The larger the difference between shear parameters λ_2 and λ_3 is, the stronger the anisotropy is. The obtained averaged distribution of normal stresses $\hat{\sigma}_{zz}$ with respect to the radial coordinate of the cylinder clearly shows a dependence of the bulk stresses and surface layer's properties on the rate of anisotropy, as demonstrated in Fig. 5.11a. Thus, Fig. 5.11b represents similarly normalized curves using bulk values, where the different thickness and amplitude of the surface layer effect are observable.

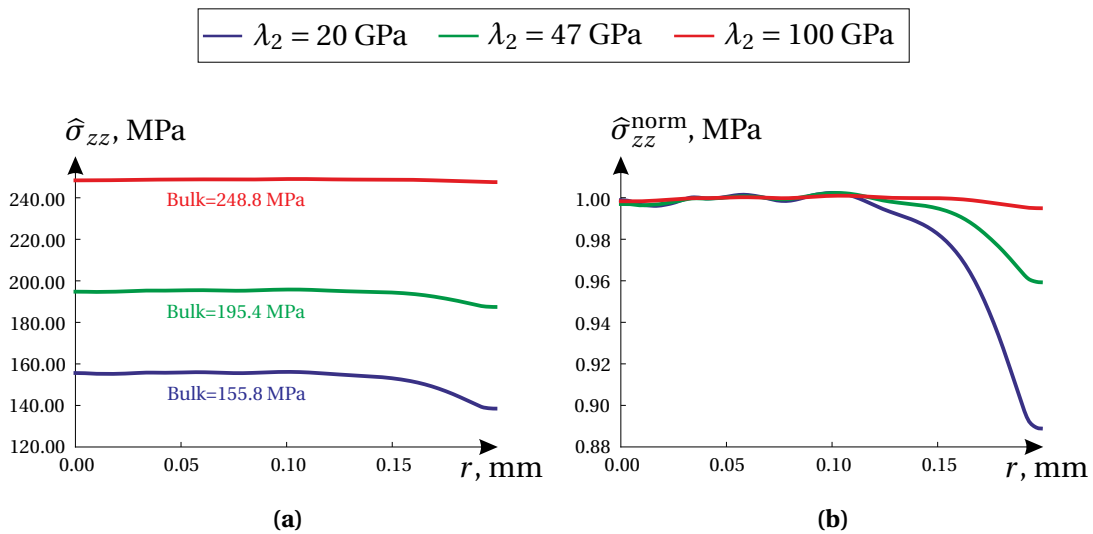


Figure 5.11 Average stresses vs. radial coordinate in a cylindrical specimen with the elastic grain material model: (a) non-normalized; (b) normalized

5.1.7 Elastic tension of notched cylindrical bar

The surface layer effect was initially discovered in smooth models of a cylindrical bar and a rectangular plate. It is clearly observed in the averaged distribution of stresses and investigated by the comparison of

values in the surface layer and bulk region. However, microparts with a complex shape are widely used in devices and mechanisms and should be thoroughly investigated too. The analysis of a heterogeneous polycrystalline microstructure in models with notches, cuts, and holes is more complicated, due to the macroscopic stress and strain gradients. In the present work, the cylindrical bar with a circumferential notch is simulated considering both a homogeneous and a polycrystalline microstructure, as represented in Fig. 5.12. Since stresses and strains in the polycrystalline model are highly heterogeneous, the statistical analysis with the point-wise averaging technique is performed in this test. Thus, 500 randomized polycrystals with 2000 grains are generated and simulated under tension.

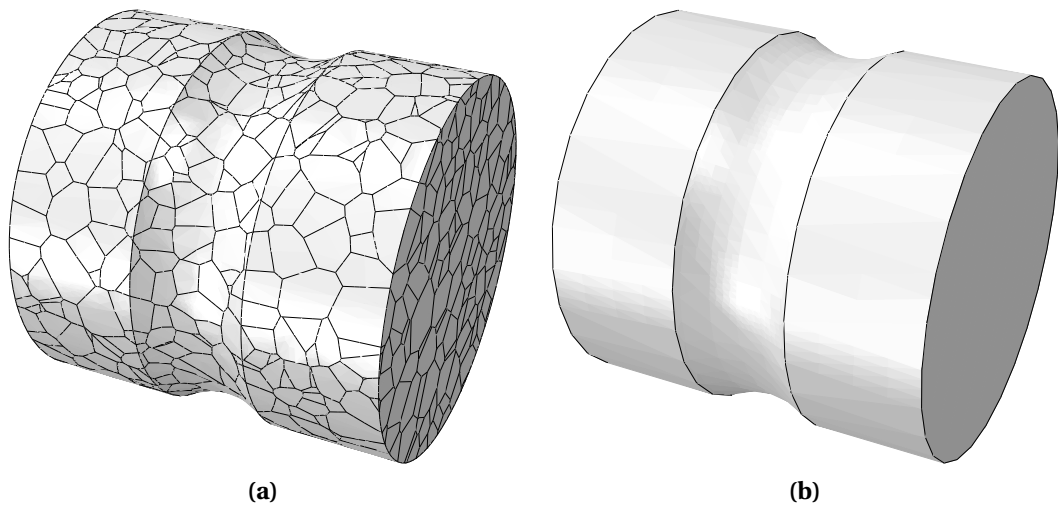


Figure 5.12 Cylindrical bar with circumferential notch: (a) example of polycrystal; (b) analogue homogeneous model

Considering a homogeneous structure, the isotropic constitutive material model can be formulated through a homogenization procedure of polycrystals in a series of tensile and shear tests. The procedure implies a fitting of the material model's parameters according to the homogenized response. The comparison of the simulation results between homogeneous and polycrystalline models allows us to recognize the surface layer effect or other unclear features. Nevertheless, the observed difference between the solutions can mistakenly be stated as an important effect, while it may actually be caused by an imperfect description of the homogeneous material model. The purely elastic behavior in both a polycrystalline and an analogue isotropic homogeneous structure is considered to reduce the homogenization error.

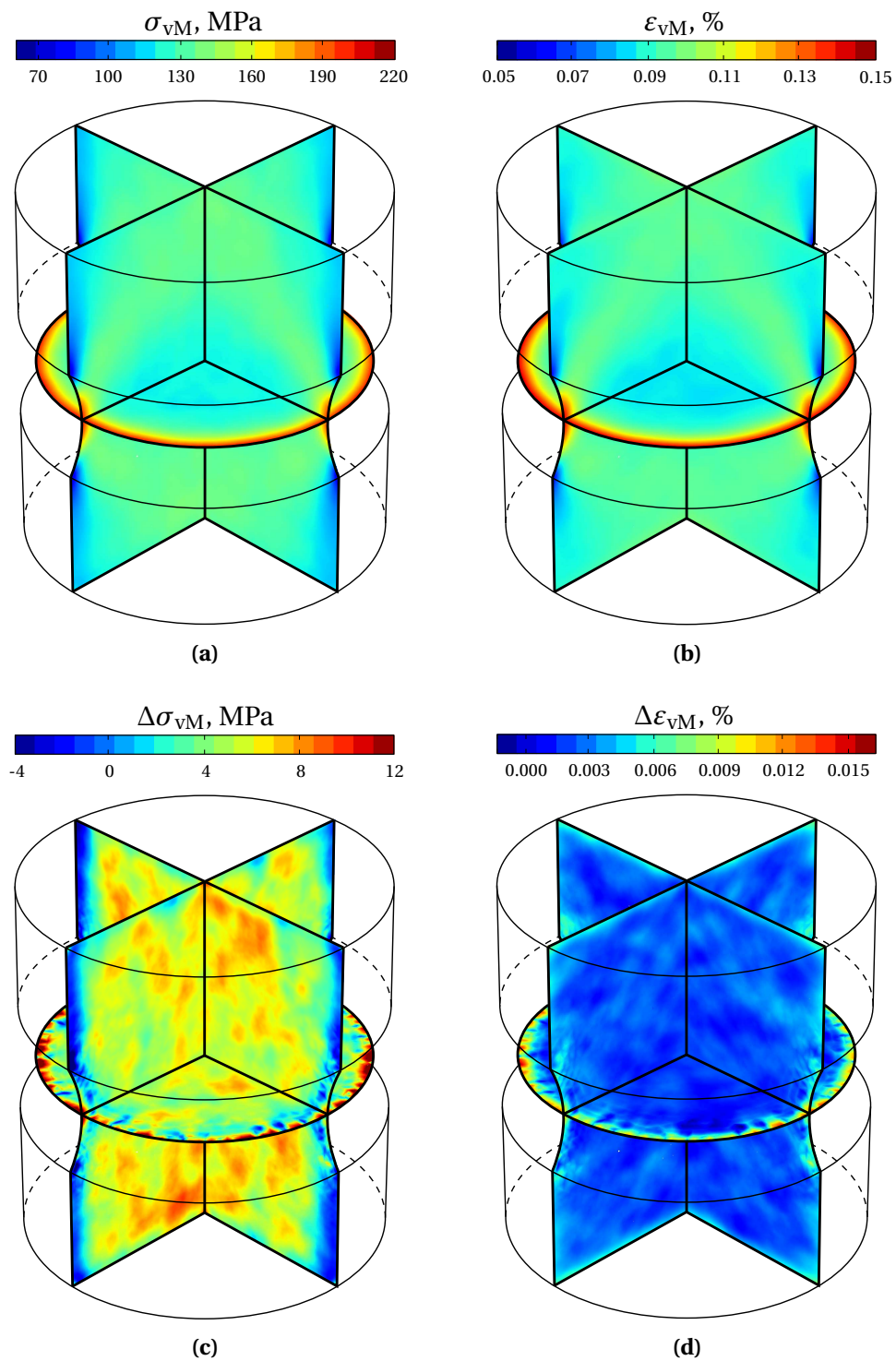


Figure 5.13 Averaged distributions of equivalent von Mises stresses (a) and strains (b) in elastic tensile test of notched cylindrical polycrystalline model. Difference of stresses (c) and strains (d) between polycrystalline and analogue homogeneous model

Furthermore, the elastic solution can be calculated in a single time increment of FEA, while plenty iterations are needed for inelastic simulation. For this reason, the number of realizations and the number of grains were increased to achieve smother averaged distributions of stresses and strains.

The homogenized Young's modulus $\bar{E} = 129.6$ GPa and the poisson ratio $\nu = 0.341$ were calculated in elastic tensile tests of unit cell polycrystalline models. Thus, the isotopic elastic classical continuum model is formulated in a notched cylinder with a homogeneous structure, taking into account the estimated macroscopic elastic constants.

The finite element analysis of 500 polycrystals and single homogeneous sample is performed, applying identical tensile displacement-controlled load on the sides and free boundary conditions on the surfaces. Fig. 5.13a shows an averaged distribution of equivalent von Mises stresses in three orthogonal cross-sections of 500 polycrystals. These distributions are calculated by point-wise averaging and interpolation algorithms, which were explained in Chapter 4. For the comparison with the polycrystalline model, the distribution of equivalent von Mises stresses is obtained from the homogeneous sample considering the same cross-sections. The difference between averaged polycrystalline and homogeneous stress distributions is demonstrated in Fig. 5.13c. In the similar way the distributions of equivalent von Mises strains are calculated according to following equation taken from [4] and illustrated in Fig. 5.13b:

$$\varepsilon_{vM} = \frac{2}{3} \sqrt{\frac{3(e_{xx}^2 + e_{yy}^2 + e_{zz}^2)}{2} + 3(\varepsilon_{xy}^2 + \varepsilon_{yz}^2 + \varepsilon_{zx}^2)} \quad (5.3)$$

where deviatoric strains:

$$\begin{aligned} e_{xx} &= +\frac{2}{3}\varepsilon_{xx} - \frac{1}{3}\varepsilon_{yy} - \frac{1}{3}\varepsilon_{zz} \\ e_{yy} &= -\frac{1}{3}\varepsilon_{xx} + \frac{2}{3}\varepsilon_{yy} - \frac{1}{3}\varepsilon_{zz} \\ e_{zz} &= -\frac{1}{3}\varepsilon_{xx} - \frac{1}{3}\varepsilon_{yy} + \frac{2}{3}\varepsilon_{zz} \end{aligned} \quad (5.4)$$

The Figure 5.13d represents the difference of equivalent von Mises strains between polycrystalline and analogue homogeneous models.

The difference of equivalent stresses between the polycrystalline and the homogeneous model clearly shows the presence of the surface layer effect. Moreover, despite the identical dimensions of the specimens and loading conditions, one can observe higher bulk stresses in the polycrystalline model in comparison with homogeneous one. At the same time, the equivalent strain distributions are nearly uniform except for the concentration area. It

can probably be explained by an inaccurate identification of the macroscopic elastic constants or the artifacts in deformation gradient at the loading sides of the model. Hence, the difference between the models consists of two components: the surface layer effect and the static error. In addition, the different behavior of the surface layer effect can be noticed in the concentration area and around it. Hence, a thorough simulation of the polycrystalline microstructure in models with a macroscopic deformation gradient is necessary to analyze the observed features. Anyway, the presence of the surface layer effect is confirmed considering both a purely elastic and a viscoplastic material behavior.

5.2 Intergranular fracture

In order to investigate the damage evolution in a polycrystalline microstructure and the propagation of the surface layer effect, the simulation of intergranular fracture is performed in this work. Unlike transgranular fracture based on damage of the crystalline lattice inside grains, the intergranular one takes place along the grain boundaries. This behavior is inherent for copper polycrystals under creep conditions at elevated temperatures.

The general goal of this simulation is a qualitative analysis of stress and strain redistribution in a single cylindrical polycrystalline sample with approximately 1000 grains, which is demonstrated in Fig. 5.14. For this purpose, a cohesive zone model was introduced in the finite-thickness grain boundaries, as explained in the sections 2.4.1 and 3.2. Elastic and damage behavior of the boundary layer can be formulated by three traction-separation laws (TSL): one in normal and two in shear directions. The damage initiation and failure criteria are defined in such a way as to make the boundaries weaker in normal directions in respect to shear direction.

The finite element model of the polycrystal is composed of grain tetrahedra and special-purpose prism finite elements in the grain boundary layer. Due to a compatible finite element mesh, the convergence of the simulation can be achieved by using the cohesive zone approach, even though a large number of grains is generated. Furthermore, the artificial parameter viscosity allows us to significantly improve the convergence of the simulation. On the other hand, it influences the material behavior, which should be investigated at first.

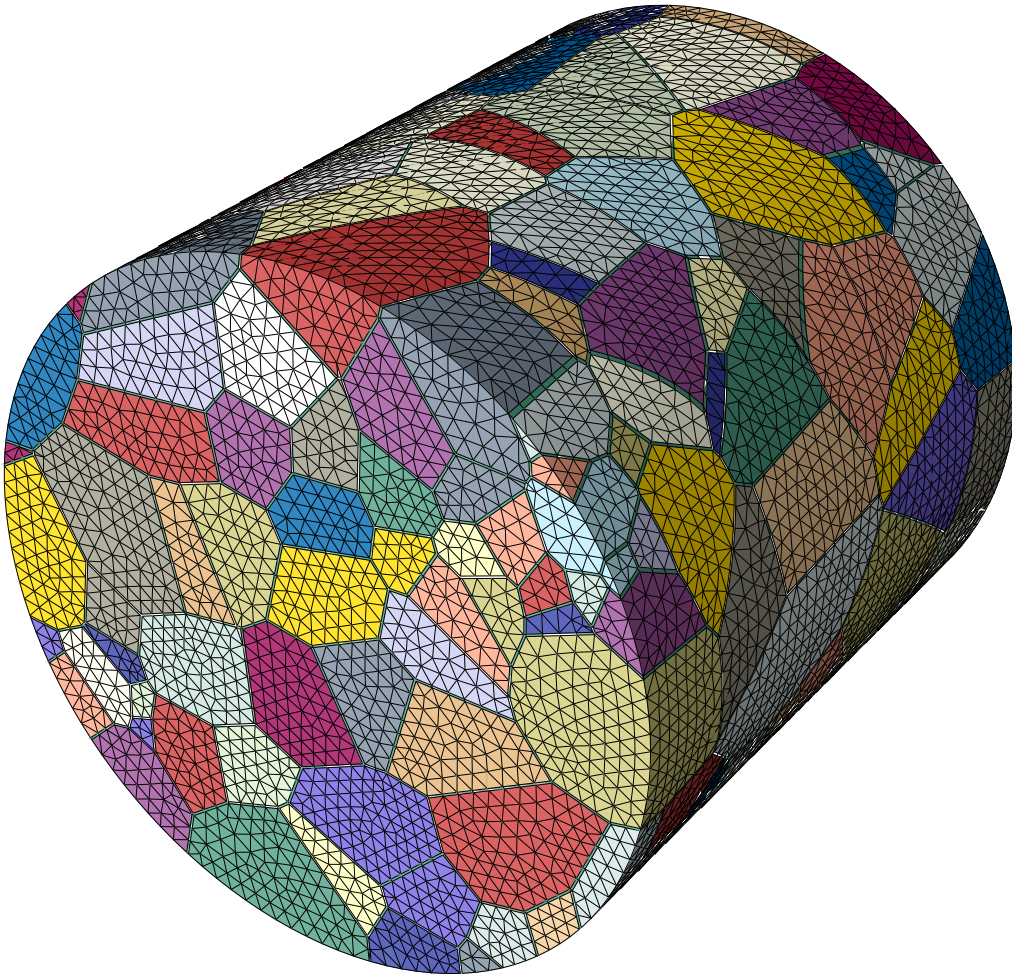


Figure 5.14 Cylindrical polycrystal with finite-thickness grain boundaries

5.2.1 Sensitivity analysis of viscosity parameter

According to Abaqus Analysis User's Manual [2], the viscosity regularization can improve the convergence of the cohesive zone approach by "permitting stresses to be outside the limits set by the traction-separation law". The viscosity parameter in constitutive equations represents a relaxation time of a viscous system at the softening regimes. If it is relatively small in respect to the integration time, the convergence of the solution can be improved without compromising results. For this reason, the sensitivity analysis of a polycrystal with 1000 grains is performed with three different values of the viscosity parameter. In the first test, the displacement-controlled tension is applied on the sides of the cylinder, considering the same loading strain rate of 0.025%/h. Fig. 5.15a represents averaged normal stresses σ_{zz} within grains

in models with the viscosity parameter $\mu = [0.1, 0.5, 0.9]$. Thus, the higher the viscosity is defined, the higher stress response is achieved. On the other hand, the accumulation of averaged damage at grain boundaries proceeds slower for a higher viscosity, as illustrated in Fig. 5.15b.

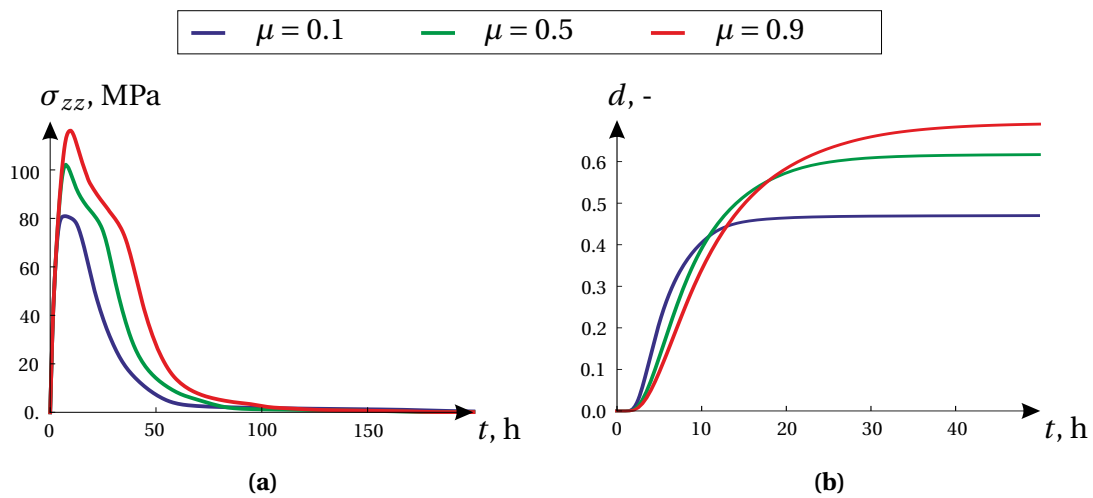


Figure 5.15 Influence of the viscosity parameter in displacement-controlled tension test: (a) average stresses in grains; (b) average damage in grain boundaries

The dependence of the macroscopic polycrystalline response on the viscosity parameter was investigated under creep conditions as well. The same free boundary conditions are used on the surface of the cylinder, while constant tension with an amplitude of 80 MPa is applied on the sides. In addition, the specimen is constrained to equal nodal axial displacements on the ends of the cylinder. Figures 5.16a and 5.16b display average value of the damage parameter in grain boundaries and average normal total strains ε_{zz} in grains, respectively, in models with a viscosity $\mu = [0.025, 0.05, 0.1]$. Despite the same loading conditions, the different evolution behavior of damage and total strains can be observed. According to the mentioned theoretical formulations, the smallest viscosity value 0.025 corresponds to a more precise solution. However, the rate of convergence in that case is not appropriate for the simulation of polycrystals with a large number of grains. For this reason, a viscosity value of 0.1 is considered in the following analysis. Although the solution of a finite element model is certainly compromised, the investigation of intergranular fracture of polycrystals can be performed qualitatively.

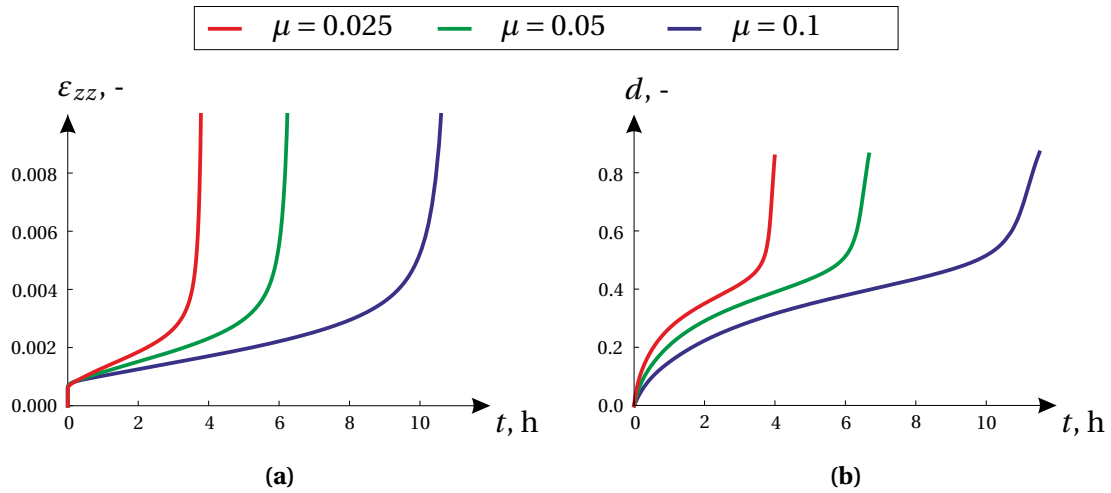


Figure 5.16 Influence of the viscosity parameter in creep test: (a) total strains; (b) average damage in grain boundaries

5.2.2 Displacement-controlled test

The comparison of the macroscopic behavior in the surface and bulk regions is the main goal in the analysis of intergranular fracture. In the presented test, the displacement-controlled uniaxial tension is applied on the one end of the cylindrical polycrystal, while symmetric boundary conditions are applied on the other one. The surface of the cylinder is free of constraints. Thus, a single specimen with approximately 1000 grains was tensed up to 2.5% of deformations in 100 h with a constant total strain rate.

Using the sub-domain volumetric averaging technique, one can calculate macroscopic stresses, strains, and damage in surface layer and bulk region. The radius of the specimen is $200 \mu\text{m}$ with an approximate grain size of $40 \mu\text{m}$. However, to distinguish macroscopic response in these regions, the averaging domain of the surface layer has a thickness of $10 \mu\text{m}$, while the radius of the bulk domain is $120 \mu\text{m}$. Thus, in the diagrams below, the green and blue lines represent the averaged values over the surface and bulk domains, respectively.

Fig. 5.17b illustrates the applied deformation amplitude by a black line along with the averaged total strains over grains in the two mentioned regions. The results of averaging show that grains in the surface layer are deformed to a higher extent in comparison with the bulk grains. It is also noticeable in Fig. 5.17a, where the distribution of axial total strains at the moment of failure is presented. Nevertheless, higher averaged axial stresses can be observed in the bulk grains, as demonstrated in Fig. 5.17a. A similar behavior of the surface

layer effect was discovered during the analysis of polycrystals with perfectly bonded grains and can be explained by the fact that grains on the surface are less constrained. In addition, Fig. 5.17c shows the different rate of the average damage evolution in the cohesive zone. Thus, the damage evolves faster in the bulk boundaries than in the surface layer.

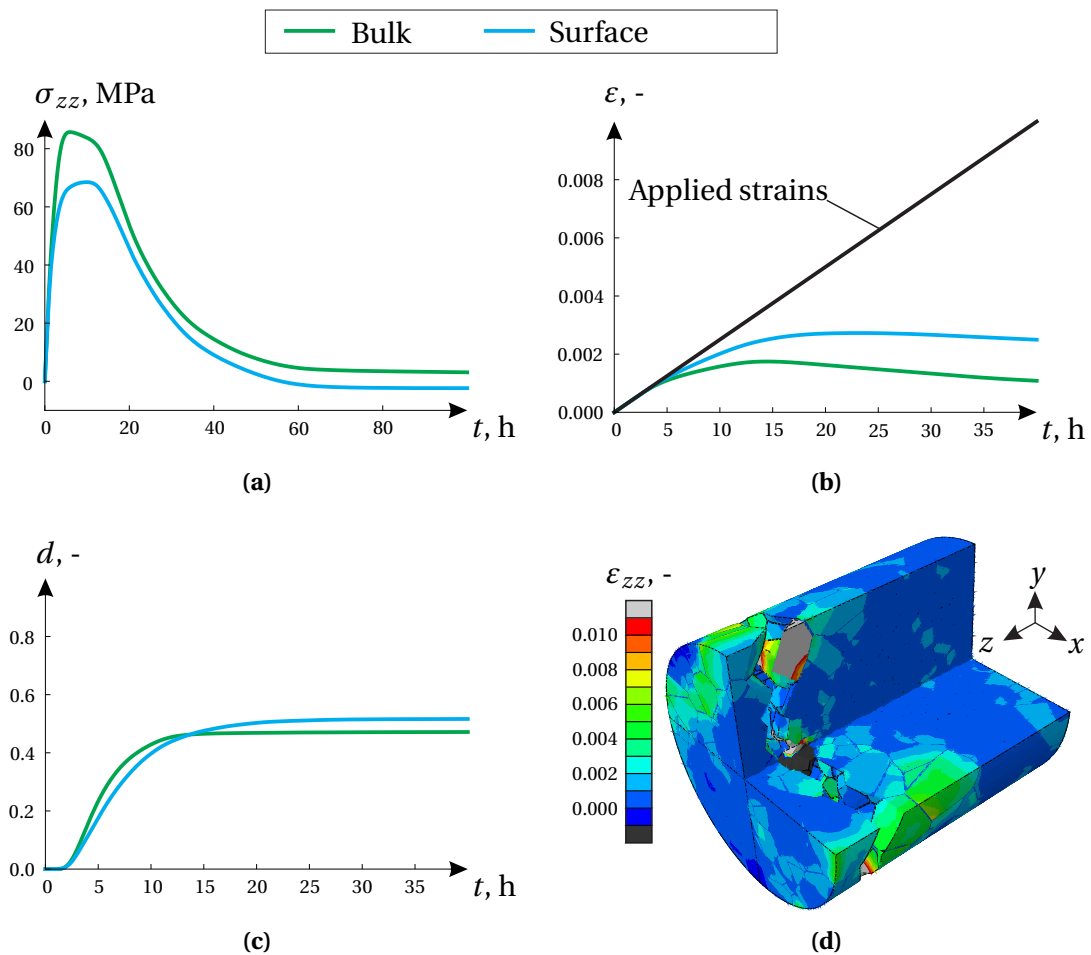


Figure 5.17 Cylindrical polycrystal under displacement-controlled tensile load: (a) average stresses in grains; (b) average total strains in grains; (c) average damage in grain boundaries; (d) total strains ϵ_{zz} at time of fracture

5.2.3 Uniaxial creep test of cylindrical polycrystal

Unlike displacement-controlled tests, the uniaxial creep loading conditions imply constant tensile force. It is inherent to static working devices and parts such as fuel cells under internal pressure, tensed wires, etc. The growth of

cavities and further intergranular fracture are usual damage mechanisms in polycrystals under creep loading conditions and an elevated temperature. In order to investigate the redistribution of stresses, strains, and the damage parameter in the polycrystalline microstructure, a similar cylindrical bar with approximately 1000 grains was generated. The free boundary conditions are assigned on the surface of the sample, while symmetry is assumed on the one side. In addition, the nodes on the other side are constrained to the same displacements, which improves the distribution of the load during the deformation and crack propagation. In this test, the analysis of the stress and the deformation state in the models under three tensile loads of 75, 80, and 90 MPa is performed and visualized in the figures below by green, red, and blue colors, respectively.

Thus, Fig. 5.18a demonstrates averaged total strains, calculated through the elongation of the polycrystal. Three stages of primary, secondary and tertiary creep are observable on these curves. Furthermore, the dependence of the total strain rate on the applied load is displayed in Fig. 5.18b with respect to total strains. Thus, the secondary creep stage for higher tensile force can be barely identified.

Taking into account the same grain size and dimensions of the sample, the averaging domains for the bulk and surface regions can be defined in the same way as it was done in the displacement-controlled test. In the figures below, the solid line represents averaged bulk values, while the dashed line means averaging within the surface layer.

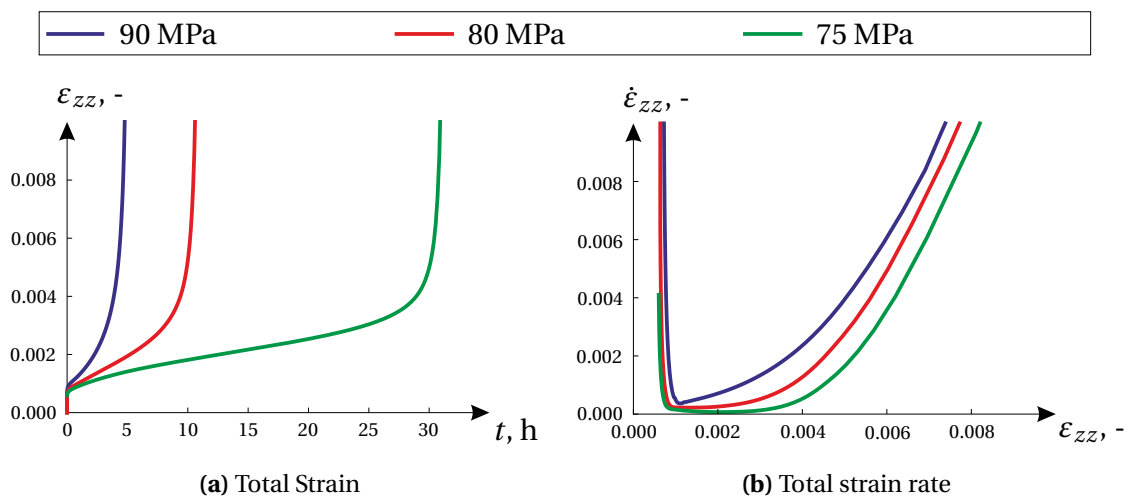


Figure 5.18 Cylindrical polycrystal in creep test under different loads: (a) averaged total strain; (b) averaged total strain rate

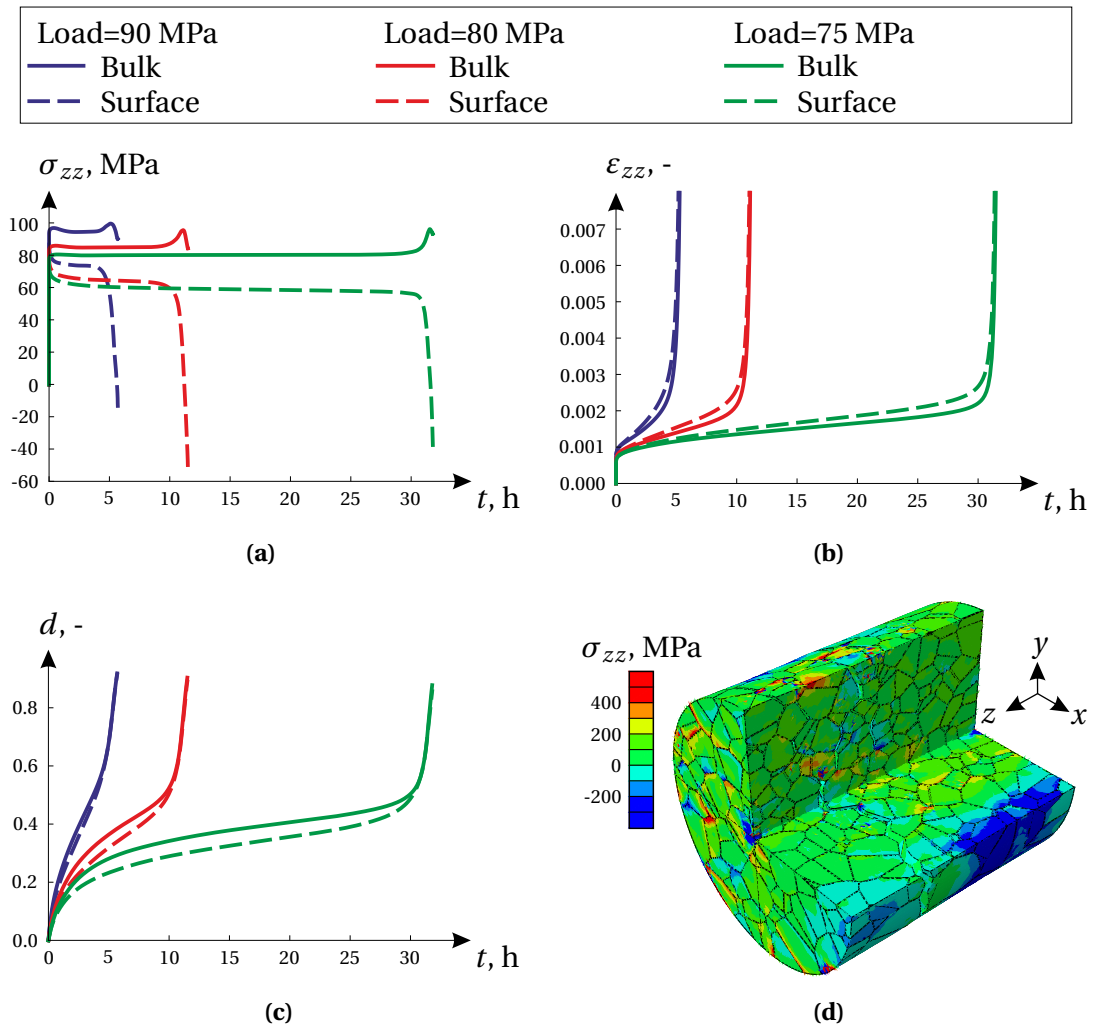


Figure 5.19 Cylindrical polycrystal in creep test: (a) averaged stresses in grains; (a) averaged stresses in grains; (b) averaged total strains in grains; (c) average damage in grain boundaries; (d) normal stresses σ_{zz}

The distribution of normal stresses σ_{zz} over the model is demonstrated in Fig. 5.19d, where the opened crack is observable. Similarly to the displacement-controlled test, the averaged grain stresses are lower in the surface layer than in the bulk region, as illustrated in Fig. 5.19a for different loading values. Apparently, the crack propagation starts on the surface of the cylinder. It can be supposed to be caused by an intensive relaxation of the surface layer along with the increase of bulk stresses. The comparison of the damage evolution within grain boundaries in Fig. 5.19c shows a certain difference between these domains, especially considering the secondary

creep stage. On the other hand, the slightly higher total strains can be observed in grains of the surface layer, as demonstrated in Fig. 5.19b. However, a larger number of samples should be investigated in order to verify the observed behavior. Anyway, the presence of the surface layer effect considering intergranular fracture of polycrystalline specimen can be confirmed.

Conclusions

In order to investigate the influence of a heterogeneous polycrystalline microstructure in microparts, the software framework was developed. The implemented scripts and libraries allow us to perform a full cycle of the numerical simulation within the CAD/CAE program Abaqus, including the generation of a geometrical and finite element model, the conducting of the finite element analysis, and the postprocessing of results.

The microstructure of copper is represented by a 3D randomized Voronoi diagram. The basic algorithms of the construction and applications of the diagram are explained in the first Chapter 2. The developed construction algorithm is based on the randomized incremental generation of a Voronoi diagram using the so-called "trial-and-error" method. The algorithm implies a particular reconstruction of the diagram during the insertion of every cell. According to the "trial-and-error" method, the insertion of a new cell is repeated if geometric criteria are not satisfied during the updating of Voronoi cells. The open-source library Voropp was chosen as sufficient groundwork for the implementation of the randomized incremental Voronoi diagram, due to its convenient cell-based code structure. Introducing several criteria such as the minimum edge length, the angle between edges or faces, etc., the appropriate Voronoi diagram without geometrical singularities can be generated.

The absence of short edges in the Voronoi diagram is especially important considering a finite-thickness grain boundary layer in order to simulate intergranular fracture. The developed algorithm computes prism grain boundaries through offsetting of the faces for a specified distance. Besides

the description of the technique, Section 2.2.3 shows a special case where the construction of a boundary may fail because of the short edge. Nevertheless, the stability and convergence can be significantly improved by ensuring the minimum edge length and other properties. The generation of the corresponding finite element model is described in Section 2.4.1. Nevertheless, most of the simulation results were obtained considering a zero-thickness boundary layer and perfectly bonded grains. This approach allows us to reduce the computational costs required for the simulation of polycrystals with large number of grains. Both approaches of the grain boundary modeling are discussed in Sections 2.3 and 2.4. These sections describe the generation of a geometrical model and a finite element mesh, respectively, along with the construction of arbitrarily shaped polycrystals such as a rectangular plate, a smooth cylindrical bar, and a circumferentially notched cylindrical bar.

Taking into account the anisotropic elasto-viscoplastic material behavior and random crystal lattice orientations inside grains, the heterogeneous distributions of stresses and strains can be observed under loading conditions. In order to investigate these distributions, two different averaging techniques are involved. The first one is based on volumetric averaging of field values over the entire domain of the specimen or over sub-domains such as the bulk region and the surface layer. However, the analysis of heterogeneous distributions considering a macroscopic gradients of stresses and strains is questionable as discussed in Chapter 4. For this reason, the point-wise averaging algorithm was developed and implemented in this work. It allows to compute an averaged distribution of the required field over plenty of randomized realizations of the polycrystalline specimen. Since the finite element meshes of polycrystals are incompatible due to their randomized structure, the sophisticated interpolation algorithm is proposed. This algorithm can calculate a value of the field at an arbitrary point within the finite element model using shape functions of the finite element. Section 4.3 describes the general idea and implementations of this algorithm for tetrahedral, prism, and hexahedral finite elements.

Using described pre- and postprocessing techniques, the polycrystalline microstructure, represented by a Voronoi diagram, was investigated under various loading conditions as shown in Chapter 5. Thus, the models of the rectangular plate, smooth, and notched cylindrical specimens with approximately 1000 grains are generated with zero-thickness grain boundaries. Applying free boundary conditions on the surface and displacement-controlled tension on the sides, a realistic numerical testing of the specimens

can be performed. The statistical analysis of stresses in these models clearly shows the presence of the surface layer effect with a thickness of 1-2 grains. For example, the averaged normal stresses in the surface layer of cylindrical specimens are approximately 20% smaller than stresses in the bulk region. Lower stresses in that region can probably be explained by the fact that grains in the surface layer are less constrained in comparison with the bulk region. However, the classical continuum theory implies the uniform distribution of stresses and strains in similar models with a homogeneous structure. Therefore, the scale separation method using a Representative Volume Element may produce a certain error in the simulation of polycrystals with a similar relationship between the grain size and the dimensions of specimens. Furthermore, the appearance of the surface layer effect in the model with a macroscopic deformation gradient is confirmed on the example of a cylindrical bar with a circumferential notch, which was investigated within elastic tension. On the other hand, the analysis of stress redistribution in the cylindrical model under various loading conditions showed the independence of the surface layer effect's properties on relaxation, loading rate, and the multicyclic load. Hence, the effect can be neglected in certain cases. Nevertheless, in order to analyze a damage propagation and the influence of the surface layer effect in polycrystals with a large number of grains, the model of intergranular fracture is considered in this work. For this reason, a single cylindrical polycrystal with approximately 1000 grains is generated considering finite-thickness grain boundaries. The grain material behavior is formulated by the same anisotropic elasto-viscoplastic material model with random orientation, while the cohesive zone model is introduced for the boundary layer. The displacement-controlled and creep tests show different distributions of stresses, total strains, and damage in the bulk region and the surface layer.

However, the further investigation of the polycrystalline microstructure is required considering a more representative geometrical model and the more precise description of material behavior in grains and boundaries. The statistical analysis can certainly be facilitated, since general properties of the surface layer effect, such as thickness, are determined. For example, the number of randomized realizations within a point-wise averaging algorithm can be reduced. Anyway, the extension of the scale-separation method with a RVE should be reconsidered in order to introduce the discovered features.

Following algorithms and methods were developed and implemented in the programming code, which was thoroughly optimized for the generation of a large number of grains:

- The randomized incremental algorithm for generation of the Voronoi diagram
- Construction of the meshable finite-thickness grain boundaries
- The 3D interpolation technique based on a finite element mesh
- The point-wise averaging algorithm for the statistical analysis of several polycrystalline samples
- Advanced meshing procedure for the sweeping of finite element mesh in grain boundaries

The essential results of this work can be summarized as follows:

- The Voronoi diagrams without short edges are generated accordingly to introduced geometrical criteria
- Due to possibility to construct a model with arbitrary shape and a large number of grains, the polycrystals with macroscopic dimensions were analyzed under various loading and boundary conditions
- The averaged distributions of stresses and strains over the solutions of a large number of samples are obtained
- These distributions show appearance of the surface layer effect as decreasing of stresses on the surface of specimens
- The observed effect can be explained by the fact that grains on the surface are less constrained than in the bulk region
- Regarding performed simulations the thickness of the surface layer is about one-two grains

Taking into account obtained results of the geometrical modeling and simulation the following recommendations for future studies can be proposed:

- The performance of the implemented programming code can be increased by using the multithreaded execution on multicore CPU or GPU

- Simulation of polycrystals with complex shape can be used for the further analysis of the surface layer effect
- A macroscopic material model must include the surface layer effect to improve accuracy of the scale-separation method
- More representable model of microstructure can be achieved by construction of the non-planar faces between grains
- The crystal plasticity theory and available user material subroutines can be used for modeling of material behavior inside grains
- More accurate interface model should be developed for the grain boundaries
- Experimental investigation of the surface layer effect

APPENDIX

A

Implicit time integration scheme

The increment of stress tensor $\Delta\boldsymbol{\sigma}$ is calculated by the following equation considering an implicit time integration scheme:

$$\Delta\boldsymbol{\sigma} = {}^{(4)}\mathbf{T} \cdot \cdot (\Delta\boldsymbol{\varepsilon}_t - \Delta\boldsymbol{\varepsilon}_t^{in}), \quad (\text{A.1})$$

where $\Delta\boldsymbol{\varepsilon}_t$ and $\Delta\boldsymbol{\varepsilon}_t^{in}$ are the total strain increment tensor and the inelastic strain increment tensor at time t , respectively. The fourth rank tensor ${}^{(4)}\mathbf{T}$ is formulated as:

$${}^{(4)}\mathbf{T} = \lambda_1 \mathbf{I} \otimes \mathbf{I} + {}^{(4)}\mathbf{K} - \frac{g\Delta t}{1 + g\Delta\boldsymbol{\sigma} \cdot \cdot {}^{(4)}\mathbf{M} \cdot \cdot \boldsymbol{\sigma}} \boldsymbol{\sigma} \cdot \cdot {}^{(4)}\mathbf{L} \otimes {}^{(4)}\mathbf{L} \cdot \cdot \boldsymbol{\sigma} \quad (\text{A.2})$$

To simplify the description of the tensor ${}^{(4)}\mathbf{T}$ in Eq. (A.1), three fourth rank tensors \mathbf{K} , \mathbf{L} , and \mathbf{M} are introduced and displayed below.

$$\begin{aligned} {}^{(4)}\mathbf{K} &= \alpha_2 {}^{(4)}\mathbf{P}_2 + \alpha_3 {}^{(4)}\mathbf{P}_3, \\ {}^{(4)}\mathbf{L} &= \alpha_2 {}^{(4)}\mathbf{P}_2 + \xi \alpha_3 {}^{(4)}\mathbf{P}_3, \\ {}^{(4)}\mathbf{M} &= \alpha_2 {}^{(4)}\mathbf{P}_2 + \xi^2 \alpha_3 {}^{(4)}\mathbf{P}_3, \end{aligned} \quad (\text{A.3})$$

where variables α_2 and α_3 should be calculated at every iteration taking into account the time increment Δt , the inelastic anisotropic parameter ξ , and elastic properties λ_i .

$$\alpha_2 = \frac{\lambda_2}{1 + \Delta t \lambda_2 h}, \quad \alpha_3 = \frac{\lambda_3}{1 + \Delta t \lambda_3 \xi h} \quad (\text{A.4})$$

The projectors ${}^{(4)}\mathbf{P}_i$ can be useful in order to decompose a fourth rank tensor according to cubic symmetry [13].

$$\begin{aligned} {}^{(4)}\mathbf{P}_1 &= \frac{1}{3}\mathbf{I} \otimes \mathbf{I}, \\ {}^{(4)}\mathbf{P}_2 &= \sum_{i=1}^3 (\mathbf{g}_i \otimes \mathbf{g}_i \otimes \mathbf{g}_i \otimes \mathbf{g}_i) - {}^{(4)}\mathbf{P}_1, \\ {}^{(4)}\mathbf{P}_3 &= {}^{(4)}\mathbf{I} - {}^{(4)}\mathbf{P}_1 - {}^{(4)}\mathbf{P}_2, \end{aligned} \quad (\text{A.5})$$

where the second rank and fourth rank unity tensors are:

$$\begin{aligned} \mathbf{I} &= \mathbf{g}_k \otimes \mathbf{g}^k, \\ {}^{(4)}\mathbf{I} &= \frac{1}{2} (\mathbf{g}_k \otimes \mathbf{I} \otimes \mathbf{g}_k + \mathbf{g}_i \otimes \mathbf{g}_j \otimes \mathbf{g}_i \otimes \mathbf{g}_j), \end{aligned} \quad (\text{A.6})$$

where \mathbf{g}_i , $i = 1, 2, 3$ is the orthonormal basis of the cubic crystal.

The generalized descriptions of the involved functions g and h are shown in the following equations:

$$g = \frac{9}{4} \frac{1}{\sigma_{\text{eq}}^2} \left(\frac{df(\sigma_{\text{eq}})}{d\sigma_{\text{eq}}} - \frac{f(\sigma_{\text{eq}})}{\sigma_{\text{eq}}} \right), \quad h = \frac{3}{2} \frac{f(\sigma_{\text{eq}})}{\sigma_{\text{eq}}}, \quad (\text{A.7})$$

where $f(\sigma_{\text{eq}})$ is a response function in constitutive equation for inelastic strains. In the case of the power law type equation $f(\sigma_{\text{eq}}) = a\sigma_{\text{eq}}^n$, these functions are:

$$g = \frac{9}{4} \frac{a\sigma_{\text{eq}}^{n-1}}{\sigma_{\text{eq}}^2} (n-1), \quad h = \frac{3}{2} a\sigma_{\text{eq}}^{n-1} \quad (\text{A.8})$$

APPENDIX

B

Mapping of arbitrary point in extruded hexahedral finite element

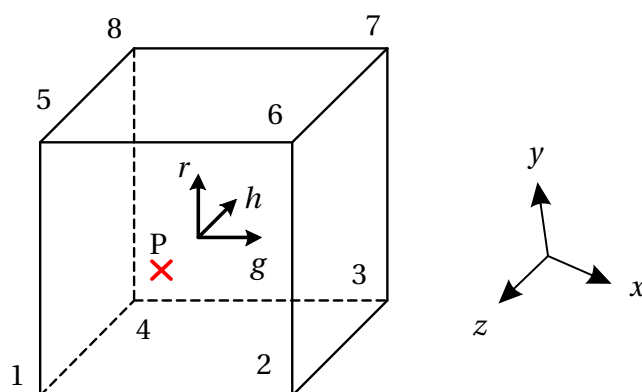


Figure B.1 Arbitrary point P within linear hexahedral finite element C3D8

In this section, the mapping procedure as the calculation of the local natural coordinates of an arbitrary point P in extruded hexahedral finite element is explained. The interpolation function of the 8-node linear hexahedral finite element is:

$$\begin{aligned}
 u(g, h, r) = & \frac{1}{8}(1-g)(1-h)(1-r)u_1 + \frac{1}{8}(1+g)(1-h)(1-r)u_2 \\
 & + \frac{1}{8}(1+g)(1+h)(1-r)u_3 + \frac{1}{8}(1-g)(1+h)(1-r)u_4 \\
 & + \frac{1}{8}(1-g)(1-h)(1+r)u_5 + \frac{1}{8}(1+g)(1-h)(1+r)u_6 \\
 & + \frac{1}{8}(1+g)(1+h)(1+r)u_7 + \frac{1}{8}(1-g)(1+h)(1+r)u_8,
 \end{aligned} \tag{B.1}$$

where g , h , and r are the local coordinates of the finite element, which is illustrated in Fig. B.1. Nodal values of interpolating field are defined as u_i , $i = 1..8$. Assuming $(1 - r)$ and $(1 + r)$ are known items, due to coincidence with an extrusion axis, it can be rewritten as:

$$u(g, h, r) = (1 - g)(1 - h)u_r^I + (1 + g)(1 - h)u_r^{II} + (1 + g)(1 + h)u_r^{III} + (1 - g)(1 + h)u_r^{IV}, \quad (\text{B.2})$$

where:

$$\begin{aligned} u_r^I &= \frac{1}{8} [(1 - r)u_1 + (1 + r)u_5], \\ u_r^{II} &= \frac{1}{8} [(1 - r)u_2 + (1 + r)u_6], \\ u_r^{III} &= \frac{1}{8} [(1 - r)u_3 + (1 + r)u_7], \\ u_r^{IV} &= \frac{1}{8} [(1 - r)u_4 + (1 + r)u_8] \end{aligned} \quad (\text{B.3})$$

The interpolation function can also be represented as:

$$u(g, h, r) = u_r^{C1} + gu_r^{C2} + hu_r^{C3} + ghu_r^{C4}, \quad (\text{B.4})$$

where:

$$\begin{aligned} u_r^{C1} &= u_r^I + u_r^{II} + u_r^{III} + u_r^{IV}, \\ u_r^{C2} &= u_r^{III} + u_r^{IV} + u_r^I + u_r^{II}, \\ u_r^{C3} &= u_r^{II} + u_r^{III} - u_r^I + u_r^{IV}, \\ u_r^{C4} &= u_r^{III} - u_r^I + u_r^{II} + u_r^{IV} \end{aligned} \quad (\text{B.5})$$

Substituting the global coordinates x_P , y_P , and z_P of the arbitrary point P into interpolation function (B.4), the local coordinates g and h can be found as well:

$$\begin{cases} x_r^{C1} + gx_r^{C2} + hx_r^{C3} + ghx_r^{C4} = x_P \\ y_r^{C1} + gy_r^{C2} + hy_r^{C3} + ghy_r^{C4} = y_P \\ z_r^{C1} + gz_r^{C2} + hz_r^{C3} + ghz_r^{C4} = z_P \end{cases}, \quad (\text{B.6})$$

where x_r^{C1} , x_r^{C2} , x_r^{C3} , and x_r^{C4} are constants calculated by equations (B.3) and (B.5) with nodal x-coordinates $u_i = x_i$, $i = 1..8$ and the pre-computed third local coordinate r . In the same way corresponding constants related to y- and z-axes are computed.

APPENDIX

C

Mapping of arbitrary point in extruded prism finite element

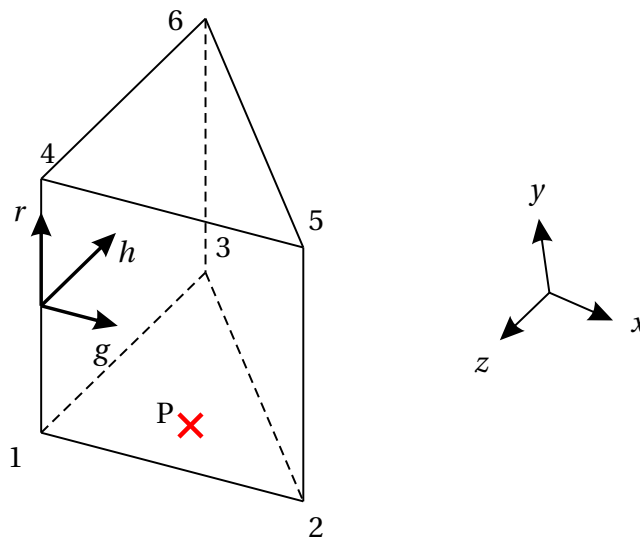


Figure C.1 Arbitrary point P within linear prism finite element C3D6

The local natural coordinates of an arbitrary point P in extruded prism finite element can be found using following mapping procedure, which is explained in this section. The interpolation function of the 6-node linear prism finite element is:

$$\begin{aligned}
 u(g, h, r) = & \frac{1}{2}(1 - g - h)(1 - r)u_1 + \frac{1}{2}g(1 - r)u_2 + \frac{1}{2}h(1 - r)u_3 \\
 & + \frac{1}{2}(1 - g - h)(1 + r)u_4 + \frac{1}{2}g(1 + r)u_5 + \frac{1}{2}h(1 + r)u_6,
 \end{aligned} \tag{C.1}$$

where g , h , and r are local coordinates of the finite element, which is illustrated in Fig. C.1. Nodal values of interpolating field are defined as u_i , $i = 1..6$. Assuming $(1 - r)$ and $(1 + r)$ are known items, due to coincidence with an extrusion axis, it can be rewritten as:

$$u(g, h, r) = (1 - g - h)(1 - r)u_r^I + gu_r^{II} + hu_r^{III}, \quad (C.2)$$

where

$$\begin{aligned} u_r^I &= \frac{1}{2} [(1 - r)u_1 + (1 + r)u_4], \\ u_r^{II} &= \frac{1}{2} [(1 - r)u_2 + (1 + r)u_5], \\ u_r^{III} &= \frac{1}{2} [(1 - r)u_3 + (1 + r)u_6] \end{aligned} \quad (C.3)$$

The interpolation function can also be represented as:

$$u(g, h, r) = u_r^I + g(u_r^{II} - u_r^I) + h(u_r^{III} - u_r^I) \quad (C.4)$$

Substituting the global coordinates x_P , y_P , and z_P of the arbitrary point P into interpolation function (C.4), the local coordinates g and h can be calculated using following system of equations:

$$\begin{cases} x_r^I + g(x_r^{II} - x_r^I) + h(x_r^{III} - x_r^I) = x_P \\ y_r^I + g(y_r^{II} - y_r^I) + h(y_r^{III} - y_r^I) = y_P \\ z_r^I + g(z_r^{II} - z_r^I) + h(z_r^{III} - z_r^I) = z_P \end{cases}, \quad (C.5)$$

where x_r^I , x_r^{II} , and x_r^{III} are constants described by Eq. (C.3) with nodal x -coordinates $u_i = x_i$, $i = 1..6$ and the pre-computed third local coordinate r . In the same way constants y_r^I , y_r^{II} , y_r^{III} , z_r^I , z_r^{II} , and z_r^{III} are calculated taking into account corresponding nodal y - and z -coordinates are computed.



Bibliography

- [1] *Atlas of Stress-strain Curves*. ASM International, 2002.
- [2] SIMULIA ABAQUS 6.12. *Abaqus Analysis User's Manual*. Dassault Systèmes Simulia Corp., USA, 2012.
- [3] SIMULIA ABAQUS 6.12. *Abaqus Scripting Reference Manual*. Dassault Systèmes Simulia Corp., USA, 2012.
- [4] TNO DIANA BV 9.4.4. *DIANA User's Manual - Analysis Procedures*, 2012.
- [5] B. Abbott. Soap bubbles. MHC Art Museum.
- [6] E. Aurenhammer. Voronoi diagrams – a survey of a fundamental geometric data structure. *ACM Comput. Surv.*, 23(3):345–405, September 1991.
- [7] E. Barbe, S. Forest, and G. Cailletaud. Intergranular and intragranular behavior of polycrystalline aggregates. part 1: F.E. model. *International Journal of Plasticity*, 17(4):513 – 536, 2001.
- [8] E. Barbe, S. Forest, and G. Cailletaud. Intergranular and intragranular behavior of polycrystalline aggregates. part 2: Results. *International Journal of Plasticity*, 17(4):537 – 563, 2001.
- [9] C.B. Barber, D.P. Dobkin, and H. Huhdanpaa. The quickhull algorithm for convex hulls. *ACM Trans. Math. Softw.*, 22(4):469–483, December 1996.

- [10] B. Bazaz, A. Zarei-Hanzaki, and S.M. Fatemi-Varzaneh. Hardness and microstructure homogeneity of pure copper processed by accumulative back extrusion. *Materials Science and Engineering: A*, 559(0):595 – 600, 2013.
- [11] R.L. Bell and T.G. Langdon. An investigation of grain-boundary sliding during creep. *Journal of Materials Science*, 2(4):313–323, 1967.
- [12] M.L. Benzeggagh and M. Kenane. Measurement of mixed-mode delamination fracture toughness of unidirectional glass/epoxy composites with mixed-mode bending apparatus. *Composites Science and Technology*, 56(4):439 – 449, 1996.
- [13] A. Bertram and J. Olschewski. Formulation of anisotropic linear viscoelastic constitutive laws by a projection method. *High temperature constitutive modeling: Theory and application ASME*, MD-Vol. 26, AMD-Vol. 121:129 – 137, 1991.
- [14] Y. Bhandari, S. Sarkar, M. Groeber, M.D. Uchic, D.M. Dimiduk, and S. Ghosh. 3D polycrystalline microstructure reconstruction from FIB generated serial sections for FE analysis. *Computational Materials Science*, 41(2):222 – 235, 2007.
- [15] A. Brahme, M.H. Alvi, D. Saylor, J. Fridy, and A.D. Rollett. 3D reconstruction of microstructure in a commercial purity aluminum. *Scripta Materialia*, 55(1):75 – 80, 2006.
- [16] B.L. Bramfitt. *Metallographer's Guide: Practice and Procedures for Irons and Steels*. EngineeringPro collection. ASM International, 2001.
- [17] D.G. Brandon, B. Ralph, S. Ranganathan, and M.S. Wald. A field ion microscope study of atomic configuration at grain boundaries. *Acta Metallurgica*, 12(7):813 – 821, 1964.
- [18] J. Budai, W. Gauddig, and S. L. Sass. The measurement of grain boundary thickness using x-ray diffraction techniques. *Philosophical Magazine A*, 40(6):757–767, 1979.
- [19] W.L. Chan and M.W. Fu. Experimental studies of plastic deformation behaviors in microheading process. *Journal of Materials Processing Technology*, 212(7):1501 – 1512, 2012.

- [20] D.-Y. Chiang. The generalized masing models for deteriorating hysteresis and cyclic plasticity. *Applied Mathematical Modelling*, 23(11): 847 – 863, 1999.
- [21] A.C.F Cocks and M.F Ashby. On creep fracture by void growth. *Progress in Materials Science*, 27(3-4):189 – 244, 1982.
- [22] R.D. Cook, D.S. Malkus, M.E. Plesha, and R.J. Witt. *Concepts and Applications of Finite Element Analysis, 4th Edition*. Wiley, 4 edition, October 2001.
- [23] R. Courant. Variational methods for the solution of problems of equilibrium and vibrations. *Bulletin of the American Mathematical Society*, 49:1–23, 1943.
- [24] A. Curnier. *Computational Methods in Solid Mechanics*. Developments in Hydrobiology. Springer Netherlands, 1994.
- [25] B. Delaunay. Sur la sphère vide. A la mémoire de Georges Voronoï. *Bulletin de l'Académie des Sciences de l'URSS*, 6:793–800, 1934.
- [26] G. Dhatt and G. Touzot. *The finite element method displayed*. (A Wiley-Interscience publication). Wiley, 1984.
- [27] G.L. Dirichlet. Über die Reduktion der positiven quadratischen Formen mit drei unbestimmten ganzen Zahlen. *Journal für die Reine und Angewandte Mathematik*, 40:209–227, 1850.
- [28] C. Efstathiou, H. Sehitoglu, and J. Lambros. Multiscale strain measurements of plastically deforming polycrystalline titanium: Role of deformation heterogeneities. *International Journal of Plasticity*, 26 (1):93 – 106, 2010.
- [29] M. S. Floater. Mean value coordinates. *Comput. Aided Geom. Des.*, 20 (1):19–27, March 2003.
- [30] S. Fortune. A sweepline algorithm for voronoi diagrams. In *Proceedings of the Second Annual Symposium on Computational Geometry*, SCG '86, pages 313–322, New York, NY, USA, 1986. ACM.
- [31] S. Fortune. Voronoi diagrams and delaunay triangulations. *Computing in Euclidean geometry*, 1:193–233, 1992.

- [32] F. Fritzen, T. Böhlke, and E. Schnack. Periodic three-dimensional mesh generation for crystalline aggregates based on voronoi tessellations. *Computational Mechanics*, 43(5):701–713, 2009.
- [33] Christophe G. and Jean-François R. Gmsh: A 3-d finite element mesh generator with built-in pre-and post-processing facilities. *International Journal for Numerical Methods in Engineering*, 79(11):1309–1331, 2009.
- [34] V. Gergely and B. Clyne. The formgrip process: foaming of reinforced metals by gas release in precursors. *Advanced Engineering Materials*, 2(4):175–178, 2000.
- [35] T. Gnäupel-Herold, P.C. Brand, and H.J. Prask. Accessing the elastic properties of cubic materials with diffraction methods. In *Advances in X-ray Analysis*, volume 42, pages 464–470. IDDC, 1998.
- [36] D. Gochfeld and O. Sadakov. *Plasticity and creep of construction elements under repeatable loadings, on russian: Plastichnost' i polzuchest' elementov konstruksiy pri povtornykh nagruzheniyakh*. Moskva "Mashinostroenie", 1984.
- [37] C. Gratin. *De la représentation des images au traitement morphologique d'images tridimensionnelles*. PhD thesis, Ecole des Mines de Paris, 1993.
- [38] P. J. Green and R. Sibson. Computing dirichlet tessellations in the plane. *The Computer Journal*, 21(2):168–173, 1978.
- [39] M. Groeber, S. Ghosh, M.D. Uchic, and D.M. Dimiduk. A framework for automated analysis and simulation of 3D polycrystalline microstructures. part 2: Synthetic structure generation. *Acta Materialia*, 56(6):1274 – 1287, 2008.
- [40] M.A. Groeber, B.K. Haley, M.D. Uchic, D.M. Dimiduk, and S. Ghosh. 3D reconstruction and characterization of polycrystalline microstructures using a FIB—SEM system. *Materials Characterization*, 57(4—5):259 – 273, 2006.
- [41] E.O. Hall. The deformation and ageing of mild steel: Iii discussion of results. *Proceedings of the Physical Society. Section B*, 64(9):747, 1951.
- [42] M. Herbig, A. King, P. Reischig, H. Proudhon, E.M. Lauridsen, J. Marrow, J.Y. Buffière, and Wo. Ludwig. 3-d growth of a short fatigue crack within a polycrystalline microstructure studied using combined diffraction and

- phase-contrast x-ray tomography. *Acta Materialia*, 59(2):590 – 601, 2011.
- [43] R. Hill. Elastic properties of reinforced solids: Some theoretical principles. *Journal of the Mechanics and Physics of Solids*, 11(5):357 – 372, 1963.
- [44] K. Hormann. Barycentric coordinates for arbitrary polygons in the plane. Technical Report IfI-05-05, Department of Informatics, Clausthal University of Technology, February 2005.
- [45] A. Hrennikoff. Solution of problems of elasticity by the framework method. *Journal of applied mechanics*, 8.4:169–175, 1941.
- [46] M. Huang and Y. Li. X-ray tomography image-based reconstruction of microstructural finite element mesh models for heterogeneous materials. *Computational Materials Science*, 67(0):63 – 72, 2013.
- [47] K.H. Huebner. *The Finite Element Method for Engineers*. A Wiley-Interscience publication. Wiley, 2001.
- [48] M. Kova and L. Cizelj. Modeling elasto-plastic behavior of polycrystalline grain structure of steels at mesoscopic level. *Nuclear Engineering and Design*, 235:1939–1950, 2005. 17th International Conference on Structural Mechanics in Nuclear Engineering SMiRT-17 17th International Conference on Structural Mechanics in Nuclear Engineering.
- [49] P. Kratochvil. Libellenflügeln. Public Domain Pictures Site.
- [50] S. Kumar and S.K. Kurtz. Simulation of material microstructure using a 3d voronoi tessellation: Calculation of effective thermal expansion coefficient of polycrystalline materials. *Acta Metallurgica et Materialia*, 42(12):3917 – 3927, 1994.
- [51] S. Kumar and S.K. Kurtz. Monte-carlo study of angular and edge length distributions in a three-dimensional poisson-voronoi tessellation. *Materials Characterization*, 34(1):15–27, 1995.
- [52] T.G. Langdon. Grain boundary sliding as a deformation mechanism during creep. *Philosophical Magazine*, 22(178):689–700, 1970.

- [53] S.A. Langer, E.R. Fuller, and W.C. Carter. Oof: Image-based finite-element analysis of material microstructures. *Computing in Science & Engineering*, 3(3):15–23, 2001.
- [54] M.P. Laurent. Residual stress changes in garigue. volume ii - a continuum surface layer effect in polycrystalline aggregates. Technical Report NAWCADWAR-95033-4.3 (Vol. II), Engineering Science and Mechanics Department, Virginia Polytechnic Institute and State University, January 1994.
- [55] H. M. Ledbetter and E. R. Naimon. Elastic properties of metals and alloys. II. copper. *Journal of Physical and Chemical Reference Data*, 3(4):897–935, 1974.
- [56] D.M. Lee and L.A. Pinol. Effects of tin and copper nanotexturization on tin whisker formation. In *IPC APEX EXPO 2012*, pages 337–359. Curran, 2012.
- [57] X. Li, W. Hu, S. Xiao, and W.Q. Huang. Molecular dynamics simulation of polycrystalline molybdenum nanowires under uniaxial tensile strain: Size effects. *Physica E: Low-dimensional Systems and Nanostructures*, 40(10):3030 – 3036, 2008.
- [58] H. H. Liu, S. Schmidt, H. F. Poulsen, A. Godfrey, Z. Q. Liu, J. A. Sharon, and X. Huang. Three-dimensional orientation mapping in the transmission electron microscope. *Science*, 332(6031):833–834, 2011.
- [59] W. Ludwig, A. King, P. Reischig, M. Herbig, E.M. Lauridsen, S. Schmidt, H. Proudhon, S. Forest, P. Cloetens, S. Rolland du Roscoat, J.Y. Buffière, T.J. Marrow, and H.F. Poulsen. New opportunities for 3d materials science of polycrystalline materials at the micrometre lengthscale by combined use of x-ray diffraction and x-ray imaging. *Materials Science and Engineering: A*, 524(1–2):69 – 76, 2009. Special Topic Section: Probing strains and Dislocation Gradients with diffraction.
- [60] G. Masing. Zur heynschen theorie der verfestigung der metalle durch verborgen elastische spannungen. In *Wissenschaftliche Veröffentlichungen aus dem Siemens-Konzern*, pages 231–239. Springer Berlin Heidelberg, 1923.
- [61] T. Mayer, E. Mazza, and S.R. Holdsworth. A masing-type modelling concept for cyclic plasticity at elevated temperature. In H. Altenbach

and S. Kruch, editors, *Advanced Materials Modelling for Structures*, volume 19 of *Advanced Structured Materials*, pages 263–273. Springer Berlin Heidelberg, 2013.

- [62] W.H. Miller. *A Treatise on Crystallography*. Deighton, 1839.
- [63] A.F. Möbius. *Der barycentrische Calcul*. 1827.
- [64] S. Murakami and Y. Sanomura. Creep and creep damage of copper under multiaxial states of stress. In A. Sawczuk and B. Bianchi, editors, *Plasticity Today – Modelling, Methods and Applications*, pages 535 – 551. Elsevier, London, New York, 1985.
- [65] K. Naumenko and H. Altenbach. *Modeling of Creep for Structural Analysis*. Springer, Berlin ;Heidelberg, 2007. Includes bibliographical references (p. [199]-214) and index.
- [66] P. Niggli. *Die topologische Strukturanalyse I*, volume 65. *Zeitschrift für Kristallographie*, 1927.
- [67] Mikael Nygårds. Number of grains necessary to homogenize elastic materials with cubic symmetry. *Mechanics of Materials*, 35(11):1049 – 1057, 2003.
- [68] H. Ogawa, F. Wakai, and Y. Waseda. Molecular dynamics simulation of the model grain boundary structure of polycrystalline materials. *Molecular Simulation*, 18(3):179–192, 1996.
- [69] O. Ozhoga-Maslovskaia. *Micro scale modeling grain boundary damage under creep conditions*. PhD thesis, Otto-von-Guericke-UniversitätMagdeburg, 2014.
- [70] V.A. Pal'mov. *Vibrations of Elasto-Plastic Bodies*. Foundations of Engineering Mechanics. Springer, 1998.
- [71] P. Paufler, E. Gustav, and R. Schulze. *Physikalische Grundlagen mechanischer Festkörpereigenschaften*. Vieweg, Braunschweig, 1978.
- [72] N. J. Petch. The cleavage strength of polycrystals. *J. Iron Steel Inst. Lond.*, 173:25–28, 1953.
- [73] W.D. Pilkey and D.F. Pilkey. *Peterson's Stress Concentration Factors*. Wiley, 2008.

- [74] R. Quey, P.R. Dawson, and F. Barbe. Large-scale 3d random polycrystals for the finite element method: Generation, meshing and remeshing. *Computer Methods in Applied Mechanics and Engineering*, 200(17-20): 1729 – 1745, 2011.
- [75] D. Raabe and M. Sachtleber. Measurement of plastic strains by 3D image correlation photogrammetry at the grain scale, 2003.
- [76] D. Raabe, M. Sachtleber, Z. Zhao, F. Roters, and S. Zaefferer. Micro-mechanical and macro-mechanical effects in grain scale polycrystal plasticity experimentation and simulation. *Acta Materialia*, 49(17):3433 – 3441, 2001.
- [77] R. Raj and M.F. Ashby. On grain boundary sliding and diffusional creep. *Metallurgical Transactions*, 2(4):1113–1127, 1971.
- [78] A.C.E. Reid, S.A. Langer, R.C. Lua, V.R. Coffman, S.I. Haan, and R.E. García. Image-based finite element mesh construction for material microstructures. *Computational Materials Science*, 43(4):989 – 999, 2008.
- [79] A. Reuss. Berechnung der fließgrenze von mischkristallen auf grund der plastizitätsbedingung für einkristalle . *ZAMM - Journal of Applied Mathematics and Mechanics / Zeitschrift für Angewandte Mathematik und Mechanik*, 9(1):49–58, 1929.
- [80] C.H. Rycroft. Voro++: a three-dimensional voronoi cell library in c++. *Chaos*, 19(4):041111, 2009.
- [81] D.M. Saylor, J. Fridy, B.S. El-Dasher, K.-Y. Jung, and A.D. Rollett. Statistically representative three-dimensional microstructures based on orthogonal observation sections. *Metallurgical and Materials Transactions A*, 35(7):1969–1979, 2004.
- [82] D. Schrichte. Green sea turtle. Conserve Turtles Org, 2014.
- [83] B.M. Schroeter and D.L. McDowell. Measurement of deformation fields in polycrystalline OFHC copper. *International Journal of Plasticity*, 19(9):1355 – 1376, 2003.
- [84] M.I. Shamos and D. Hoey. Closest-point problems. In *Foundations of Computer Science, 1975., 16th Annual Symposium*, pages 151–162, Oct 1975.

- [85] G. Simmons. Single crystal elastic constants and calculated aggregate properties. Technical report, DTIC Document, 1965.
- [86] I. Simonovski and L. Cizelj. Automatic parallel generation of finite element meshes for complex spatial structures. *Computational Materials Science*, 50(5):1606 – 1618, 2011.
- [87] I. Simonovski and L. Cizelj. Towards modeling intergranular stress corrosion cracks on grain size scales. *Nuclear Engineering and Design*, 246(0):107 – 114, 2012. Selected and expanded papers from International Conference Nuclear Energy for New Europe 2010, Portorož, Slovenia, September 6-9, 2010.
- [88] I. Simonovski and L. Cizelj. Cohesive element approach to grain level modelling of intergranular cracking. *Engineering Fracture Mechanics*, 110(0):364 – 377, 2013.
- [89] R. P. Skelton. The growth of grain boundary cavities during high temperature fatigue. *Philosophical Magazine*, 14(129):563–572, 1966.
- [90] R.P. Skelton, H.J. Maier, and H.-J. Christ. The baushinger effect, masing model and the ramberg-“osgood relation for cyclic deformation in metals. *Materials Science and Engineering: A*, 238(2):377 – 390, 1997.
- [91] E. Slowik. Descartes’ physics. In *The Stanford Encyclopedia of Philosophy*. Stanford University, summer 2014 edition, 2014.
- [92] J. Snow. *On the Mode of Communication of Cholera*. John Churchill, 1855.
- [93] R. N. Stevens. Grain-boundary sliding and diffusion creep in polycrystalline solids. *Philosophical Magazine*, 23(182):265–283, 1971.
- [94] H.Q. Sun, Y.-N. Shi, M.-X. Zhang, and K. Lu. Plastic strain-induced grain refinement in the nanometer scale in a mg alloy. *Acta Materialia*, 55(3): 975 – 982, 2007.
- [95] H. Van Swygenhoven, A. Caro, and D. Farkas. A molecular dynamics study of polycrystalline fcc metals at the nanoscale: grain boundary structure and its influence on plastic deformation. *Materials Science and Engineering: A*, 309-310(0):440 – 444, 2001. Dislocations 2000: An International Conference on the Fundamentals of Plastic Deformation.

- [96] A. Tatschl and O. Kolednik. On the experimental characterization of crystal plasticity in polycrystals. *Materials Science and Engineering: A*, 356(1—2):447 – 463, 2003.
- [97] C. Turan, Ö.N. Cora, and M. Koç. Effect of manufacturing processes on contact resistance characteristics of metallic bipolar plates in PEM fuel cells. *International Journal of Hydrogen Energy*, 36(19):12370 – 12380, 2011.
- [98] V. Tvergaard. On the creep constrained diffusive cavitation of grain boundary facets. *Journal of Mechanics Physics of Solids*, 32:373–393, 1984.
- [99] V. Tvergaard. Effect of grain boundary sliding on creep constrained diffusive cavitation. *Journal of the Mechanics and Physics of Solids*, 33 (5):447 – 469, 1985.
- [100] T. Van der Putte and H. Ledoux. Modelling three-dimensional geoscientific datasets with the discrete Voronoi diagram. In *Advances in 3D Geo-Information Sciences*, Lecture Notes in Geoinformation and Cartography, pages 227–242. Springer-Verlag, Berlin Heidelberg, 2011.
- [101] W. Voigt. Ueber die Beziehung zwischen den beiden Elasticitätsconstanten isotroper Körper. *Annalen der Physik*, 274:573–587, 1889.
- [102] G. Voronoi. Nouvelles applications des paramètres continus à la théorie des formes quadratiques. *Journal für die Reine und Angewandte Mathematik* 133, pages 97–178, 1907.
- [103] E.L. Wachspress. *A Rational Finite Element Basis*. Academic Press rapid manuscript reproductions. Academic Press, 1975.
- [104] K. Wang, N.R. Tao, G. Liu, J. Lu, and K. Lu. Plastic strain-induced grain refinement at the nanometer scale in copper. *Acta Materialia*, 54(19): 5281 – 5291, 2006.
- [105] S. Weyer, A. Fröhlich, H. Riesch-Oppermann, L. Cizelj, and M. Kovac. Automatic finite element meshing of planar voronoi tessellations. *Engineering Fracture Mechanics*, 69(8):945 – 958, 2002.
- [106] E. Wigner and F. Seitz. On the constitution of metallic sodium, I. *j-PHYS-REV-2*, 43(10):804–810, May 1933.
- [107] Wikipedia. Voronoi diagram — wikipedia, 2014.

- [108] B. Wilshire and A.J. Battenbough. Creep and creep fracture of polycrystalline copper. *Materials Science and Engineering: A*, 443(1-2): 156 – 166, 2007.
- [109] O.C. Zienkiewicz and R.L. Taylor. *The Finite Element Method*, volume 1. McGraw-Hill, London, 1989.
- [110] O.C. Zienkiewicz and R.L. Taylor. *The Finite Element Method: Solid mechanics*. Number v. 2 in Referex collection. Mecánica y materiales. Butterworth-Heinemann, 2000.
- [111] O.C. Zienkiewicz and R.L Taylor. *Finite Element Method: Volume 1 - The Basis*. Butterworth-Heinemann, Oxford, 5th edition, 2000.
- [112] G. Zlateva and Z. Martinova. *Microstructure of Metals and Alloys: An Atlas of Transmission Electron Microscopy Images*. Taylor & Francis, 2008.

Lebenslauf

Persönliche Daten

Name, Vorname: Prygorniev, Oleksandr
 Geburtsdatum: 22 November 1987
 Geburtsort: Kharkiv (Ukraine)
 Familienstand: ledig
 Nationalität: ukrainisch

Schulbildung

1995–2005 Gesamtschule, Kharkiv (Ukraine)

Studium

2005–2009 Bachelor of Computer Science
 Nationale Technische Universität
 "Kharkiver Polytechnisches Institut",
 Kharkiv (Ukraine)

2009–2011 Master of System Analysis
 Nationale Technische Universität
 "Kharkiver Polytechnisches Institut",
 Kharkiv (Ukraine)

2011– PhD
 Otto-von-Guericke-Universität,
 Magdeburg (Deutschland)

Berufserfahrung

2006–2009 Softwareentwickler
 "ElectroPromAvtomatika" GmbH, Kharkiv (Ukraine)

2010–2011 Softwareentwickler
 "Tehnokon" GmbH, Kharkiv (Ukraine)

2011–2013 Stipendiat
 Otto-von-Guericke-Universität,
 Magdeburg (Deutschland)

2013–2014 Wissenschaftlicher Mitarbeiter
 Otto-von-Guericke-Universität,
 Magdeburg (Deutschland)

Magdeburg, 20.03.2015

Oleksandr Prygorniev